



ISSN 1028-8546

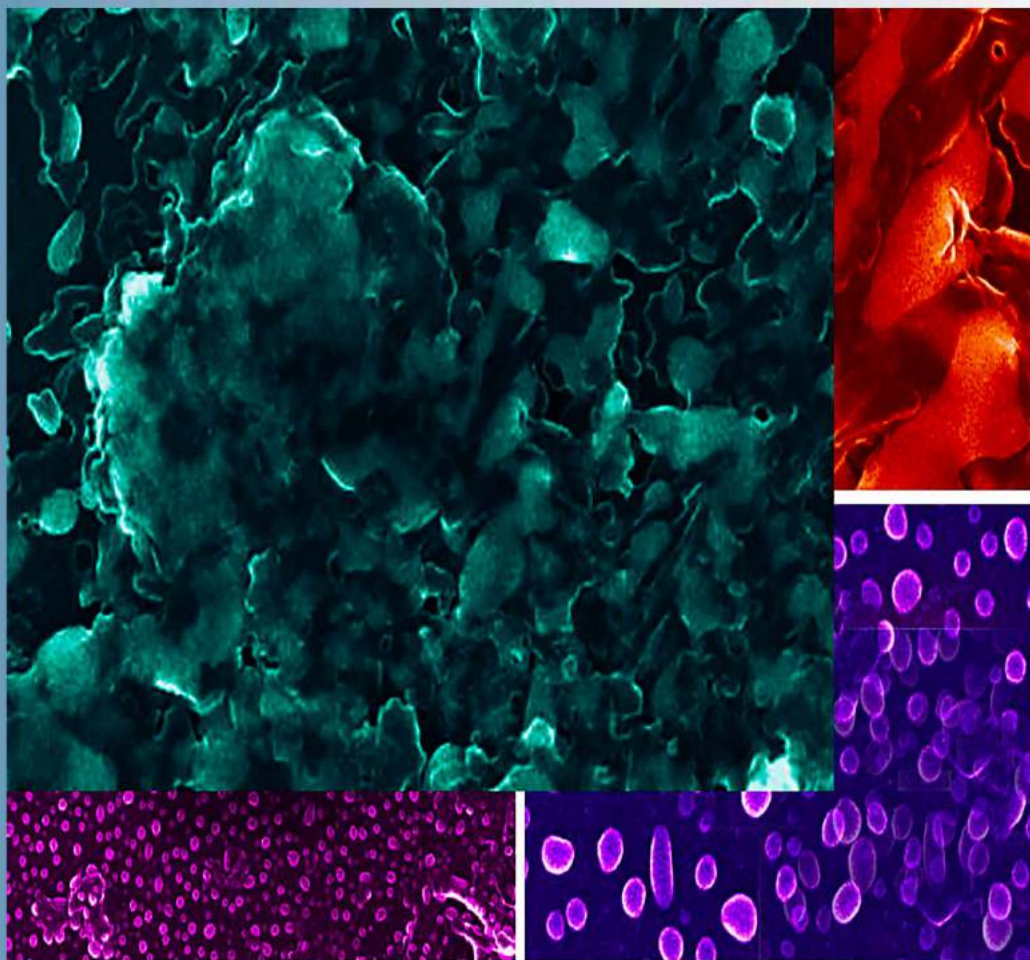
Volume XXVI Number 4

Section: En December, 2020

Azerbaijan Journal of Physics

Fizika

www.physics.gov.az
jophphysics.wixsite.com/ajpphysics



Institute of Physics
Azerbaijan National Academy of Sciences
Department of Physical, Mathematical and Technical Sciences

Published from 1995
Ministry of Press and Information
of Azerbaijan Republic,
Registration number 514, 20.02.1995

ISSN 1028-8546
vol. XXVI, Number 04, 2020
Series: En

Azerbaijan Journal of Physics

FIZIKA

*Institute of Physics
Azerbaijan National Academy of Sciences
Department of Physical, Mathematical and Technical Sciences*

HONORARY EDITORS

Arif PASHAYEV

EDITORS-IN-CHIEF

Nazim MAMEDOV

Chingiz QAJAR

SENIOR EDITOR

Talat MEHDIYEV

INTERNATIONAL REVIEW BOARD

Ivan Scherbakov, Russia
Kerim Allahverdiyev, Azerbaijan
Mehmet Öndr Yetiş, Turkey
Gennadii Jablonskii, Belarus
Rafael Imamov, Russia
Vladimir Man'ko, Russia
Eldar Salayev, Azerbaijan
Dieter Hochheimer, USA
Victor L'vov, Israel

Vyacheslav Tuzlukov, South Korea
Majid Ebrahim-Zadeh, Spain
Anatoly Boreysho, Russia
Mikhail Khalin, Russia
Hasan Bidadi, Tebriz, Iran
Natiq Atakishiyev, Mexico
Tayar Djafarov, Azerbaijan
Arif Hashimov, Azerbaijan

Javad Abdinov, Azerbaijan
Salima Mehdiyeva, Azerbaijan
Talat Mehdiyev, Azerbaijan
Ayaz Bayramov, Azerbaijan
Tofiq Mammadov, Azerbaijan
Shakir Nagiyev, Azerbaijan
Rauf Guseynov, Azerbaijan
Yusif Asadov, Azerbaijan

TECHNICAL EDITORIAL BOARD

Senior secretary: Elmira Akhundova; Nazli Huseynova, Gulnura Jafarova
Nigar Akhundova, Elshana Aleskerova, Rena Nayimbayeva

PUBLISHING OFFICE

131, H. Javid ave., AZ-1143, Baku
ANAS, Institute of Physics

Tel.: (99412) 539-51-63, 539-32-23
Fax: (99412) 537-22-92
E-mail: jophphysics@gmail.com
Internet: www.physics.gov.az
<https://jophphysics.wixsite.com/ajpphysics>

Published at "Omega-5"
41, Aga Nematulla str., Baku

Sent for printing on: __.__. 201__
Printing approved on: __.__. 201__
Physical binding: _____
Number of copies: _____ 200
Order: _____

It is authorized for printing:

ON BIOLOGICAL ACTIVITY OF SELENIUM COMPOUNDS

(Ideas of G.M. Abdullayev in modern perceptions about biological role of Se).

T.M. GUSEYNOV², T.R. MEHDIYEV¹, R.T. GULIYEVA², B.SH. BARKHALOV¹

¹Institute of Physics of ANAS, H.Javid ave., 131, AZ-1143, Baku, Azerbaijan

²Institute of Biophysics of ANAS, Zahid Khalilov., 117, Baku, AZ 1141

The inorganic compounds (sodium selenide) and organic compounds (Ebselen) can significantly influence on the development of virus infection including COVID-19. The oxidative stress is the one of COVID-19 key damaging elements. One of the main reasons of its activity is that M-RNA COVID-19 has the gens of important seleno-containing proteins (GP, TRx, SelenP) for synthesis and expression of which use the internal resources of selenium, forming its deficit that leads to limit of selenoprotein synthesis of organism. That's why selenium status can have the significant value for both processes of infection beginning and severity of disease carrying out and following complications connected with damage of immune response and development of oxidative stress.

keywords: sodium selenide, Ebselen, selen, COVID-19, selenium in human health

PACS: 64.70.Fx 36.40

INTRODUCTION

In the history of selenium research, since its discovery by I.Berzelius in 1817, one can distinguish some separate stages associated with investigation of its activity and distribution in nature, in particular, in cells of living organism [1,2]. First of all, these are works of American scientist K.Shwartz who established the anti-necrotic role of Se in organisms of several animals in 1957 [3] and thus, he proved the illegality of attitude to this element only as purely toxic [4, 5].

The information that known antiperoxide enzyme glutathione peroxidase [6] protective towards hemoglobin, is the seleno-dependent protein having the wide antioxidant properties was given in 1973 in works of L.A. Floe and I.H. Rotruk [7,8]. The works of Azerbaijan scientist G.M.Abdullayev, whose activity stimulated the complex study of selenium biological properties in Azerbaijan scientific centers on physics and biology, play important role in development of this stage of investigation. The facts of light sensitivity amplification of organ of sight by selenium (sodium selenite), stability of tissues and cells to oxidative stress and also stability of whole organism to such disturbing factor of environment as radioactive radiation and mutagenesis caused by it and others, were established. The big cycle of works is devoted to the influence of selenium on growth and multiplication of vegetable objects and micro-organisms, selenium metabolism in organs and tissues of oncological sick, deceleration mechanism by selenium of tumor cell growth on inhibition model of activities of DNA and RNA polymerases. The cycles of works are made on the example of the flu virus and the effectiveness of sodium selenite on inhibition of replicative and transcription processes associated with genetic material of flu virus A (H₃N₂). Note that Azerbaijan chemists synthesized the series of effective selenium organic compounds in 70-80th which showed the high biological properties against series of pathologies. Comparing the structural formulae of these compounds with those which nowadays are used

in clinic medicine and agriculture (veterinary) (Ebselen, selenpiran and others) we accept that choice of synthesis of effective selenium organic compounds is right.

In 70-80th it was shown that Se localizes in all cells of organism [9,10] and mortality from cancer depends on regional soil supply by Se [5,11,12]. Selenium deficit increased the virulence of low-activity virus Koksaki-B3 damaging the heart muscle so-called Keshan disease by Chinese province suffering from selenium deep deficit [13,14]. The three selenium-containing enzymes on different levels taking part in regulation of iodine exchange were identified in 90th [15]. These discoveries stimulated big interest to its intracellular regulation functions. Nowadays, more than 25 of selenium-containing proteins in the cells of most different organs and tissues have been identified. It is established that the part of the selenoproteins has the concrete physiological functions, moreover, that many of them have anti-oxidative functions [15,16]. The unique mechanism of selenoprotein synthesis so-called SESIS-mechanism had been also discovered. It includes 21 required amino-acid selenocysteine which is coded by stop-codon UGA in structure m-RNA. Selenium is included in selenoproteins through selenocysteine t-RNA which is synthesized by the means of transition of Se group in serine t-RNA from selenium-phosphate. This mechanism is unique because it has co-translation character at which the protein synthesis on ribosomes takes place simultaneously with synthesis of 21st amino-acid (i.e. transformation of serine in selenocysteine) [16,17].

In the end of 90th and early 2000th there was the supposition that Se has the anticancer activity along with antivirus one [13,18]. Earlier known fact of Koksaki-B3 inhibition virus activity is the reason of it [18]. Recently, it had been revealed that such virus diseases as Khant fever [19], Zika [20], hepatitis C[21], HIV [22-24], Ebola [25-27], different flus [28-30] take places difficultly at selenium deficit which along with Zn and vitamin D plays the important role in supply of normal immunity [31,32]. The mortality

from HIV in selenium-deficit regions was in 3-5 times higher than in normal ones. For HIV infection the mortality in several regions of Africa achieved 20-multiple exceed [22,23]. Taking under consideration that genome COVID-19 contains the elements of HIV, Ebola, SARS-CoV-1 and etc. [24-26, 33, 34, 35] on the base of analysis of the present publications, collaborators of Institute of Biophysics of ANAS made an assumption that increasing selenium deficit in many countries is caused by significant decrease of ecological situation [35]. In particular, the increasing atmosphere gas contamination leading to soil oxidation, heavy metals and chemicalization of agriculture lead to strong decrease of selenium slip forms, i.e. to depletion of plants by selenium and correspondingly, to weakening of supply of animals and plants by selenium [35]. Note that last 40-50 years the thinning-down of atmosphere ozone layer and consequently, increase of hard component of sun UV radiation stimulating the photo-oxidative processes required the compensation and increased discharge of anti-oxidants including Se has been taken place. We can add that general climate warming including so-called greenhouse effect can lead to increase of selenium deficit and correspondingly, to appearing of earlier "sleeping" virus types or increase of virulence of already present ones [35a].

Nowadays, considering the Se participation in many biological processes including the development of virus infections, it is necessary to accept that predictions of G.M.Abdullayev on role of this element in life processes and activity of biological objects in many aspects were prophetic ones.

The widely spread dangerous virus diseases, that have appeared recently, are caused, as a rule, by RNA-viruses containing selenoproteins in their genome (glutathione peroxidase, tioredoxinreductase, SeP and others). The attempt to generalize previously available facts and information on Se participation in development processes of these virus infections is the aim of the present investigation. This is important for both understanding of Se role and generation of optimal method use of seleno-containing compounds for medical treatment of virus diseases.

COVID-19 (SARS-COV-2)

Not considering details of SARS-CoV-2 appear, one can make some static analysis of factors influencing on its distribution, virulence, pathogenicity of ecological factors taking under consideration the clear irregularity of its consequences on people health in different countries, having the different both social-economical and geographical conditions. Here we note the analogy with earlier known virus diseases connected with disturbance of immune response, in particular, we note HIV infection [25,26] the genome of which is the part of present COVID-19 genome [33, 34].

Note, that we earlier noted that HIV infection distribution is geographically connected with regions of Se low content in soils. In Africa HIV infection has become the pandemic character and quarter of

population suffers from this disease. In particular, in Zambia, Botswana and Zimbabwe the quantity of infected people is 20-25% [35]. Besides, Senegal in West Africa has the lowest indexes of distribution of AIDS and cancer along with highest soil levels enriched by Se [36].

The connection between increased mortality from AIDA and selenium ecological deficit is shown for US [35]. It was shown that the increased mortality from AIDS is observed at selenium lowered level. The investigations carried out by Etan U.Taylor and his collaborators also proved that AIDS, Kaposi's sarcoma and cancer diseases are more spread in regions with seleno-deficit soils and this is true for not only for Africa, but for whole World [34]. In China seleno-deficit regions are known as "Chinese disease belt". Here, the everyday average selenium consumption is less than 10 µg (norm is 100 µg) that leads to activation of Koksaki B3 virus mutation leading to heart pathological state in regions of "Chinese disease belt". The increase of selenium content in food ration can also significantly decrease the sphere of cancer activity and decrease of mortality from cardiac infarction [13,14].

In Europe, Russia and Ukraine the monitoring investigations which have revealed the seleno-deficit of population, are carried out. The legislative measures on enrichment of food ration by selenium have been accepted in several states. It is mentioned that last 20-30 years the supply of selenium with food has decreased in 50% even in such conservative and healthy country as Great Britain. We don't mention the countries of "third world" where very bad situation with food. The wide use of import products of "intensive agriculture production" (this is actual for Azerbaijan population) is included in number of factors defining the selenium content in organisms [35, 37, 38]. Note that genome of many RNA viruses contains the code for seleno-dependent glutathione-peroxidase (GP). Some changes in environment that have appeared in the end of 20th to beginning 21th hundred have significantly improved AIDS competitive ability that became the reason of AIDS wide spread. These changes were analyzed in the works of Taylor and his colleagues [25, 25, 34]. These authors also showed that in the middle of 90th there was virus group having the gen coding the seleno-dependent glutathione peroxidase. This virus group included HIV-1 and HIV-2, also virus Koksaki B3 defining the development of cardiomyopathy (cardiac infarction) and viruses of B and C hepatitis's and others. The authors supposed that this fact is connected either with Se role as oxidant minimizing the consequences of oxidation stress or with its influence on gen activity in the response on HIV infection [35].

In 2014 – 2016 Taylor and his collaborators, carried out detail comparative investigations of Ebola and HIV-1 genomes showed that in their genomes towards with glutathione peroxidase the specific weight of another seleno-containing enzyme thioredoxinreductase (TRx) the gens of which overlap each other. Thioredoxinreductase has big oxidation-

recombination influence on replicative processes that causes extremely depletion of organism by Se at development of this diseases [34].

According to COVID-19 we can mention that secondary respiratory symptoms are considered more dangerous ones than the primary ones, i.e. COVID-19 is rather vascular disease than respirator one [33, 34, 40, 41]. The injury of heart and vascular system is the main reason of mortality. It is seemed that more than 50% mortality causes by myocardium disturbance (main activation symptom of Koksaki B3) and system global blood coagulability leading to hypoxia or asphyxia [41]. On the base of analysis of present publications one can conclude that patients with normal selenium level in blood and glutathione peroxidase, revealed in period of previous pandemia of H1N1 flu, significantly easier treat this disease [33, 34]. On model tests (on mice) the analogous results had been obtained, i.e. mice which were given selenium died in 3 times [33,34]. The analogous results were obtained for flu virus A (H₃N₂) [34]. In last epidemiological investigations connected with COVID-19 carried out in China by international group of scientists were shown the presence correlative connection between selenium content in hair and recovering: survival rate in 5 times (Hubai province, center Uhan) in comparison with lowered selenium status (Heylunczan province). Moreover, the weakening of development form of disease itself is the important index. This is seen even on the example of one Chinese province (Uhan) but in different cities with different selenium status where mortality ratio is 1:3 [42].

In order to answer to question how Se can influence of virus infection, in particular, on COVID-19 and other similar RNA virus infections, it is necessary to pay attention on following circumstances. The virus particle consists of hydrophobic membrane with protein matrix on external part of which the spikes containing glycoproteins and also esterase proteins locate; in internal part of hydrophobic membrane the carrier of its genome, mRNA (it codes 29 proteins) in the form of looped form covered nucleocapsid protein locate [43, 43a]. These strikes interact with membrane apparatus of host cells (i.e. cells of healthy organism) and form the contact with their receptor proteins with following destroy of membrane integrity promoting the penetrating of virus genetic material inside host cells. Taking under consideration that SARS-CoV-1, SARS-CoV-2 destroy mainly on vascular system (lungs, heart, kidneys, eyes and etc.) then we mention that cell membrane of vascular epithelium includes the series of integral proteins (ACE2 is angiotensin-convertingenzyme2, trans-membrane protease, metal-peptidase and others), having the ability to interact with virus protein SARS-CoV-1 и SARS-CoV-2 (sociability COVID-19 is in more than 10 times higher than for SARS-CoV-1, that is explained by peculiarities of strike protein composition) [43, 44]. Thus, the interruption of virus contact with cell membrane because of structure change of any protein being on strike is the preventive measure for development of infection process [40].

And what is about Se? The fact is that sulphur the content of which in nature from 300 up to 1000 times and in 500 times higher that selenium itself, is the nearest analogue of selenium. The main fact is that Se plays the leading role in formation of protein structure because of SH-groups formation and disulfide bridges (S-S) joining the different groups of protein molecule [2]. Note, that protein disulfide isomerase (PDI) actively take participation in realization of glycoprotein strike contact SARS-CoV-2 with membrane receptors of host cells and their inhibition makes difficult the virus penetration inside healthy cells [40,44].

NATRIUM SELENITE

Sodium selenite presents itself the white crystal powder or crystals dissolved in water. Selenium preparations in small doses act similar to E vitamin, i.e. they take part in processes of tissue breath and oxidation phosphorylation. Sodium selenite has anti-coagulation and anti-toxic properties. As strong anti-oxidant it decreases and breaks the peroxide formation, prevents the overoxidation of fatty acids and accumulation of toxic peroxides in organism and thus normalizes the metabolism. Selenium preparations in big doses are toxic and by their activity are similar to arsenic compounds.

However, in case of Na selenite having the intensive intracellular oxidation metabolism [45-47], it actively reacting with SH-groups of important strike protein SARS-CoV-2-PDI-(SH)₂ catalyzes their oxidation by following scheme:



Thus, in case if the oxidation modification PDI by sodium selenite then this protein loses the ability to interact with integral protein ACE2 of host (organism) membrane cells and the difficulty of contact between virus and healthy cells of organism takes place. There are series of useful properties of sodium selenite in opposition with RNA infection which can be expressed in the form:

1. As it is mentioned above in genome of such viruses as HIV, Ebola, Khant, series of flus, C hepatitis, SARS-CoV-1, SARS-CoV-2 and others are coded such selenoproteins as glutathione peroxidase, thioredoxinreductase, Se-P protein and others. The selective capture of mRNA part responsible for Se-Cys of amino acid for expression of selenoproteins [25, 26], firstly, enzyme thioredoxinreductase which is supplier of protons for necessities of DNA synthesis of healthy cells takes place at penetration in cell of RNA virus host as a result of anti-meaning interactions of mRNA virus and mRNA host cells [23,34]. Thus, as a result the double selenium resource consumption of organism cells necessary for synthesis of both virus selenoproteins and eigen necessities takes place. Thus, selenium deficit state leading to formation of active forms of oxygen [25, 26, 33, 34] and weakening of

immunity on phone of oxidation stress and decrease of organism antioxidation defense appears. In this connection sodium selenite is the successful selenium form which promotes to rapid selenium penetration into cellular structures including the overcoming of hematoencephalic barrier [34, 45-48], that allows us to use sodium selenite for support of essential level of selenoproteins defending organism cells from oxidation stress [12, 48, 49].

2. On model tests with application of tumor cells it is established that sodium selenite suppresses the polymerase reactions of RNA and DNA and thus it can inhibit the tumor growth that shows on the possibility of braking and virus reproduction in host cells [50]. The confirmation of this is the fact that sodium selenite inhibits the reproduction of A group virus already in 80th [50a].
3. Using the known fact that SARS-CoV-1 and SARS-CoV-2 have the series of general genome properties one can make the conclusion about selenium (sodium selenite) influence on development of SARS-CoV-2 infection by SARS-CoV-1 analogy. For SARS-CoV-1 it is established that nucleocapsid protein (similarly to SARS-CoV-2) forming RNA fiber, activates the nucleocapsid factor (NF- κ B) taking participation in transcription that is accompanied by hard inflammatory process [51,52]. It is seemed that selenium actively inhibits NF- κ B protein synthesis, i.e. nucleocapsid factor [53,54], thus it inhibits the virus development in organism cells. On importance of nucleocapsid protein inhibition confirms the fact that it is the key value in transcription processes at HIV infection [55] the genome of which as it is mentioned above has many similar properties with COVID-19 genome.
4. The massive attack of interleukins IL-6 (cytokine storm) on infected organism [56,57] and the destroy of immune response [58] is the one of more dangerous consequences of COVID-19 development. In this context selenium is known as regulator of immune response on all levels: nonspecific, humoral and cellular, simultaneously it limits the activity of T-helpers [59, 60, 61, 61a].
5. As it is mentioned COVID-19 is not only respiratory disease but the vascular one connected with generation of blood supercoagulability [62] and thrombocytopenia formation [63]. Thromboxane formation A₂ (TxA₂) carrying out the platelet aggregation being the reason of blood coagulation in vessels beginning from smallest alveolar arteries up to big pulmonary ones (effect of "focusing screen") not only in lungs but in other organs enriched by vessels (heart, kidneys, retina, atrabiliary capsules and others) is in the base of these processes. [63, 64]. Sodium selenite has anti-aggregation effect based on decrease of thromboxane formation [48, 65, 66]. Note that last 30-40 years in whole World the series of

commercial semisynthetic and synthetic, organic seleno-containing compounds including Se-Met, Se-Cys in the form of biological additions (BAD) regulating or supplying the necessary selenium status has been prepared [67].

Thus, the totality of mentioned positive properties of sodium selenite gives the possibility for its wide use in the capacity of medioprophyllactic means in adjuvant therapy against virus diseases including COVID-19. In spite of advantages of sodium selenite, it has obvious disadvantages: narrow concentration range of therapy action requiring medical attention, fast action effect especially at intravenous introduction (1-2 min) [46], the withdrawal of its significant part from organism not providing the cumulative effect [45, 46, 47, 67].

"EBSELEN" PREPARATION

From above mentioned it is followed that the necessity of study of selenium organic compounds which are seemed more perspective ones in struggle with virus infections because of their low toxicity and action duration [48, 67]. However, not all seleno-organic compounds can successfully apply for prevention and medical treatment of virus diseases including COVID-19 taking under consideration the small time of virus infection development [43]. The fact is that selenium coming to organism from organic compounds passes the complex metabolic way of selenoprotein synthesis taking part in regulation of oxidative, immune, thrombogenic and other processes [61, 67]. As a rule, it stays unavailable until not releases from "organics" transferring into ion form (from Se⁺⁴ up to Se⁻²), i.e. up to selenite which is applicable for synthesis of intrinsic organism selenoproteins [45, 61, 67]. It is character that L-selenomethionine which is one of the often met in BAD or vitamin additions less that sodium selenite is applicable for adjuvant medical treatment of virus infections especially COVID-19 because of multi-stage release of selenium from selenomethionine for its resynthesizing into new selenoproteins of organism [67]. In this connection L-selenomethionine or L-selenocysteine yield to sodium selenite which comes to organism by the way of passive transport in short time, it can be used intravenously, intramuscularly, per os being the cheapest and available compendial preparation of Se produced in Russia, Ukraine, Germany and etc. known as commercial name as "Selenase".

Note that selenoorganic compound with commercial name "Ebselen" synthesized by scientists A.Vendel, P.Graph, M.Parnkhaym and others, has significant effectiveness in group of emphasized compounds. The preparation is seemed the most effective and low-toxic with wide circle of important therapeutic properties: cardiovascular, anticancer, anti-diabetic, anti-bacterial, anti-inflammatory, anti-thrombotic and others. [68, 69]. It is explained by the circumstance that Ebselen has the intrinsic glutathione peroxidase and thioredoxinreductase activity

(peroxiredoxin) carrying out their functions in the absence of these enzymes [70, 71] and also ability to interact with thiol groups in proteins with selenosulfide formation that confirms its action spectrum range on different proteins [72]. Recently the news on anti-virus activity of selenoorganic compound Ebselen on example of HIV and Ebola virus [73], C hepatitis have appeared. Ebselen principal ability and counteraction mechanism to COVID-19 [74,75] has been established in model system. The one of main protein of COVID-19 is the chymotrypsin-like protease [M^{pro}] which has the active cysteine site. This protease splits the long polypeptide on separate polypeptide fragments taking part in replication and transcription processes having in genome. Selenium of Ebselen covalently connects with cysteine of M^{pro} protein and deprives its functional activity on virus genome replication. By other words selenium not splitting from Ebselen molecule blocks its active center M^{pro} [67, 74].

These unique Ebselen properties are the reason for its study and evaluation of its anti-virus effectiveness in comparison with other known preparations which inhibit M^{pro}. Besides, it has strong anti-oxidation properties connected with glutathione peroxidase and thioredoxinreductase activities [68 – 71] under conditions when selenium from Ebselen doesn't consume for natural (intracellular) synthesis GP and TRx because of formed deficit of selenium (that takes place at the use of many other selenium compounds). It protects from oxidative stress being the main reason of virus infection mortality [33, 34, 48, 79-81]. The carried out screening investigations with high transmission capacity showed the some low-molecular ligases probably having inhibition properties among 1000 tested compounds in the capacity of more effective inhibitors M^{pro} acting on catalytic site of this enzyme. Here Ebselen is very interesting [74]. In new investigations it is shown that sensitivity of Ebselen with cavity of catalytic center M^{pro} takes place. The last investigations show that there is unknown site connecting with Ebselen in

dimerization region and it is localized between 2nd and 3rd domains of this protein. This means that Ebselen connecting between 2nd and 3rd domains has an allosteric effect which regulates access to catalytic center by the means of interaction by the loop of this protein and this causes the change of its configuration [82]. All these investigations show that Ebselen as the best antiviral preparation can found the wide clinic application.

CONCLUSION

The inorganic compounds (sodium selenide) and organic compounds (Ebselen) can significantly influence on the development of virus infection including COVID-19. The oxidative stress is the one of COVID-19 key damaging elements. One of the main reasons of its activity is that M-RNA COVID-19 has the gens of important seleno-containing proteins (GP, TRx, SelenP) for synthesis and expression of which use the internal resources of selenium, forming its deficit that leads to limit of selenoprotein synthesis of organism. That's why selenium status can have the significant value for both processes of infection beginning and severity of disease carrying out and following complications connected with damage of immune response and development of oxidative stress.

The application of selenium compounds in particular, sodium selenite having the active metabolism in organism sells on all stages of development of virus infection, is the perspective direction in the search of adjuvant means for anti-virus therapy.

Selenoorganic therapeutic compound Ebselen known its unique biological properties is the one of the most perspective anti-virus prepatations the activity of which is based on the inhibition of replication processes especially of transcription of virus genome for clinic use in medical treatment of COVID-19 and its accompanying complications by data of high-velocity screening analysis.

-
- [1] *J.J. Berzelius*. 1817, Schweigger J. 21.
 [2] *V.V. Ermakov, V.V. Kovalsky*. Biological significance of selenium, 1974, M., Nauka., P. 295.
 [3] *K. Schwarz, G.M. Foltz*. Selenium as an integral part of factor 3 against dietary necrotic liver degeneration., *J. Am. Chem. Soc.*, 1957, v.79, p. 3292-3293.
 [4] *J.W. Hamilton, A.L. Tappel*. Lipid Antioxidant Activity in Tissues and Proteins of Selenium fed Animals, *The Journal of Nutrition*, 1963, v.79, №4, p.493–502,
<https://doi.org/10.1093/jn/79.4.493>
 [5] *Fairweather-Tait S.J. Bao, M.R.Y. Broadley et.all.*, Selenium in human health and disease, 2011, v.14, №7, p.1337-1383, doi: 10.1089/ars.2010.3275.
 [6] *G.C. Mills*. Hemoglobin catabolism. I Glutathione peroxidase, an erythrocyte enzyme which protects hemoglobin from oxidative breakdown *J. Biological Chem.*, 1957, v. 229, p.189–197.
 [7] *L. Flohe, W.A. Gunzler, H.H. Schock*. Glutathione peroxidase a selenoenzyme., *FEBS Lett.*, 1973, v.32, p.132-134.
 [8] *J.H. Rotruck, A.L. Pope, H.E. Ganther, W.G. Hoekstra*. Selenium: Biochemical role as compound of glutathione peroxidase, *Science*, 1973, v.179, p. 588-590.
 [9] *D. Behne, W. Wolters*. Distribution of selenium and glutathione peroxidase in the rat *J.Nutr.* 1983, VII3, p 456-461.
 [10] *R.F. Burk, P.E. Gregory*. Some characteristics of ⁷⁵Se-P, as selenoprotein found, in rat liver and plasma and comparison of it with selenogluthathione peroxidase., *Arch. of Biochemistry and biophysics*, 1982, v. 213, p.73

- [11] *M.J. Tripp, P.D. Whanger.* Association of selenium with tissue membranes of and rat tissues, *Biol.Trace Elem.Res.*, 1984, v.6, p.445
- [12] *R.J. Shamberger, C.E. Willis.* Selenium distribution and human cancer mortality, *Grit. Rew. Clin.lab. Sci.*, 1971, v.2, p. 211-221.
- [13] *G.F. Combs.* J. Biomarkers of selenium status. *Nutrients* 2015, v. 7, p. 2209-2236.
- [14] *O.A. Levander, M.A. Beck.* Interacting nutritional and infectious etiologies of Keshan disease: Insights from coxsackie virus B-induced myocarditis in mice deficient in selenium or vitamin E. *Biol Trace Elem Res.*, 1997, v.56, №1 p. 5-21. doi: 10.1007/BF02778980.
- [15] *Q. Li, M. Liu, J. Hou, C. Jiang, S. Li, T. Wang.* The prevalence of Keshan disease in China. *Int J. Cardiol.*, 2013, v.168, №2, p.1121-1126. doi: 10.1016/j.ijcard.2012.11.046.
- [16] *K.H. Winther, M.P. Rayman, S.J. Bonnema, L. Hegedüs.* Selenium in thyroid disorders - essential knowledge for clinicians. *Nat Rev Endocrinol* 2020, v.16, №3, p.165-176. doi: 10.1038/s41574-019-0311-6.
- [17] *V.M. Labunskyy, D.L. Hatfield and V.N. Gladyshev.* Selenoproteins: molecular pathways and physiological roles. *Physiol. Rev.* 2014, v. 94, p. 739-777.
- [18] *M.A. Berry, L. Banu, J.W. Harney, and P.R. Larsen.* Functional characterization of the eukaryotic SPECIES elements which direct selenocysteine insertion at UGA codons. *EMBO J.* 1993, v.12, p.3315-3322.
- [19] *L-Q. Fang, M. Goeijenbier, S-Q. Zuo, L-P. Wang, S. Liang, S. Klein et al.* The Association between Hantavirus Infection and Selenium Deficiency in Mainland China. *Viruses.* 2015, v.7, №1, p.333 -351 doi: 10.3390/v7010333.
- [20] *E.W. Taylor, J.A. Ruzicka.* Antisense inhibition of selenoprotein synthesis by Zika virus may contribute to neurological disorders and microcephaly by mimicking SePP1 knockout and the genetic disease progressive cerebello-cerebral atrophy. *Bull World Health Organ* 2016 doi: 10.2471/BLT.16.182071.
- [21] *S.Y. Yu, W.G. Li, I.J. Zhu et. al.* Chemoprevention trial of human hepatitis with selenium supplementation in China. *Biol.Trace Elem. Res.*, 1989, v.20, p.15-22.
- [22] *M.K. Baum, G. Shor-Posner, S. Lai, G. Zhang, H. Lai, M.A. Fletcher et al.* High Risk of HIV-Related Mortality Is Associated With Selenium Deficiency: J Acquir Immune Defic Syndr Hum Retrovirol. 1997, v.15, №5, p.370-4. doi: 10.1097/00042560-199708150-00007.
- [23] *M.K. Baum, A. Campa, S. Lai, S. Sales Martinez, L. Tsalaila, P. Burns et al.* Effect of Micronutrient Supplementation on Disease Progression in Asymptomatic, Antiretrovirus-Naive, HIV-Infected Adults in Botswana: A Randomized Clinical Trial. *JAMA* 2013, v.310, №20, p. 2154-2163 doi: 10.1001/jama.2013.280923.
- [24] *J. Kamwesiga, V. Mutabazi, J. Kayumba, J.K. Tayari, J.C. Uwimbabazi, G. Batanage et al.* Effect of selenium supplementation on CD4+ T-cell recovery, virus suppression and morbidity of HIV-infected patients in Rwanda: a randomized controlled trial. *AIDS* 2015, v.29, №9, p. 1045-1052. doi: 10.1097/QAD.0000000000000673.
- [25] *E.W. Taylor, J.A. Ruzicka, L. Premadasa.* Theoretical and experimental evidence for RNA:RNA 398 antisense tethering of thioredoxinreductase mRNAs by Ebola and HIV-1 for virus selenoprotein 399 synthesis. *ResearchGate* 2015http://rgdoi.net/10.13140/RG.2.2.10237.51683.
- [26] *E.W. Taylor, J.A. Ruzicka, L. Premadasa, L. Zhao.* Cellular Selenoprotein mRNA Tethering via Antisense Interactions with Ebola and HIV-1 mRNAs May Impact Host Selenium Biochemistry. *Curr Top Med Chem* 2016, v.16, № 13, p. 1530-1535. doi: 10.2174/1568026615666150915121633.
- [27] *B. Lipinski.* Can Selenite be an Ultimate Inhibitor of Ebola and Other Virus Infections? *Br J.Med. and Med. Res.*, 2015, v. 6, p. 319-324.
- [28] *L. Yu, L. Sun, Y. Nan, L-Y. Zhu.* Protection from H1N1 Influenza Virus Infections in Mice by Supplementation with Selenium: A Comparison with Selenium-Deficient Mice. *Biol Trace Elem Res.* 2011, v.141, №1-3, p.254-61. doi: 10.1007/s12011-010-8726-x.
- [29] *M.A. Beck, H.K. Nelson, Q. Shi, P. Van Dael, E.J. Schiffrin, S. Blum.* Selenium deficiency increases the pathology of an influenza virus infection, *FASEB J.* 2001; v. 15, №.8, p. 1481-1483.
- [30] *G. Gong, Y. Li, K. He, Q. Yang, M. Guo, T. Xu et al.* The inhibition of H1N1 influenza induced apoptosis by sodium selenite through ROS-mediated signaling pathways. *RSC Adv.*, 2020, v.10, №13, p.8002-8007. doi: 10.1039/C9RA09524A.
- [31] *X. Li, M. Geng, Y. Peng, L. Meng, S. Lu.* Molecular immune pathogenesis and diagnosis of COVID-19. *J Pharm Anal* 2020, v.10, №2, p.102-108. doi: 10.1016/j.jpha.2020.03.001.
- [32] *P.R. Hoffmann, M.J. Berry.* The influence of selenium on immune responses. *Molecular Nutrition & Food Research*, 2008, v.52, №11, p.1273–1280,DOI 10.1002/mnfr.200700330.
- [33] *L. Hiffler, B. Rakotoambinina.* Selenium and RNA virus interactions: Potential implications for SARS-CoV-2 infection (COVID-19), *ResearchGate*, April 2020, 16p.DOI: 10.31219/osf.io/vaqz6.
- [34] *E.W. Taylor.* Can selenium significantly increase the cure Rate in Covid-19, An interview with prof. E.W.Taylor, *Natural Health*, 2020 News, June 18.
- [35] *T.M. Guseinov, N.S. Safarov.* Selenium and some virus diseases, *f. Biomedicine* №.2, 2007, pp.3-7.
- 35a. *G.D. Jones, B. Droz, P. Greve, P. Gottschalk, D. Poffet, S.P. McGrath et al.* Selenium deficiency risk predicted to increase under future

- climate change. *ProcNatlAcadSci*, 2017, v.114, № 11, p. 2848-2853. doi: 10.1073/pnas.1611576114.
- [36] A. *Simmonds*. Senegal puts the lid on AIDS and now has the best results in Africa. Johannesburg Independent 2001 (From Lps Angeles Times).
- [37] T.M. *Huseynov*, N.S. *Safarov*, Sh.Q. *Qanbarova*, F.R. *Yahyayeva*, E.M. *Zeynalli*. The environmental challenge of selenium deficiency, 9th Baku International Congress "Energy, Ecology, Economy". Baku, 7-9 June, 2007, p. 310-313.
- [38] E.M. *Zeynalli*, R.T. *Guliyeva*, F.R. *Yakhyaeva*. On the problem of the impending deficit of selenium in Azerbaijan, Materials of scientific-practical. confer. dedicated 80th anniversary of prof. E.I. Ibragimov. Center of Oncology of the Ministry of Health of Azerbaijan. Baku, Azerbaijan, April 4-5, 2010, p. 65-66.
- [39] Coronavirus resource center. Johns Hopkins University and Medicine, June, 2020 <https://coronavirus.jhu.edu/map.html>
- [40] M. *Kieliszeka*, B. *Lipinski*. Selenium supplementation in the prevention of coronavirus infections (COVID-19), *Medical Hypotheses* 143 May 2020, p.1, <https://doi.org/10.1016/j.mehy.2020.109878>
- [41] B. *Bikdeli*, M.V. *Madhavan*, D. *Jimenez*, T. *Chuich*, I. *Dreyfus*, E. *Driggin et al.* COVID-19 and Thrombotic or Thromboembolic Disease: Implications for Prevention, Antithrombotic Therapy, and Follow-up. *J. Am CollCardiol*, 2020, v.75, No.23, <https://doi.org/10.1016/j.jacc.2020.04.031>
- [42] J. *Zhang*, E.W. *Taylor*, K. *Bennet*, R. *Saad and M.P. Rayman*. Association between regional selenium status and reported outcome of COVID-19 cases in China. *Am.J.Clin. Nutr.* Apr 28, 2020, doi: 10.1093/ajcn/nqaa095.
- [43] R. *Lu*, X. *Zhao*, J. *Li*, P. *Niu*, B. *Yang*, H. *Wu et al.* Genomic characterisation and epidemiology of 2019 novel coronavirus: implications for virus origins and receptor binding. *The Lancet*, 2020, v.395, №10224, p.565-74. doi: 10.1016/S0140-6736(20)30251-8.
- 43a. A. *Mittal*, K. *Manjunath*, R.K. *Rahjan, et.al.* COVID-19 Pandemic: Insights into Structure, Function, and hACE2 Receptor Recognition by the SARS-CoV-2, Preprints 2020, [10.20944/preprints202005.0260.v1](https://doi.org/10.20944/preprints202005.0260.v1)
- [44] D. *Diwaker*, K.P. *Mishra*, L. *Ganju*. Potential role of protein disulfide isomerase in virus infections, *Acta Virol.*, 2013, v.57, p.293-304.
- [45] K.T. *Suzuki*. Metabolomics of Selenium: Se Metabolites Based on Speciation Studies, *Journal of Health Science*, 2005, v.51, №2, P.107-114, doi: <https://doi.org/10.1248/jhs.51.107>
- [46] K.T. *Suzuki*, Y. *Shiobara*, M. *Itoh et.al.* Selective uptake of selenite by red blood cells, *Analyst*; 1998 v.123 №1, p.63-67. DOI:10.1039/a706230c.
- [47] S.Ya. *Guseinova*. Oxidative metabolism of sodium selenite in isolated human erythrocytes in vitro, *Zh. Biomedicina*, 2019, v. 17, № 3, pp. 18-23.
- [48] O.M. *Guillin*, C. *Vindry*, T. *Ohlmann*, L. *Chavatte*. Selenium, Selenoproteins and Virus Infection. *Nutrients*, 2019, v.11, №9, p.2101. doi: 10.3390/nu11092101.
- [49] M.P. *Rayman*. Selenium and human health. *The Lancet* (2012) 379(9822):1256-68. doi: 10.1016/S0140-6736(11)61452-9.
- [50] F.I. *Abdullaev*, C. *MacVicar*, and G.D. *Frenkel*. Inhibition by selenium of DNA and RNA synthesis in normal and malignant human cells in vitro, *Cancer let.*, 1992, v.65, p.43-49.
- [51] 50a. Z.A. *Lazimova*, I.I. *Abdullaev*, F.I. *Abdullaev*, and T.B. *Asadullaev*. "Inhibitory effect of sodium selenite on influenzavirus reproduction." *VoprosiVirusology*, 1986, v.1, p.236-238.
- [52] Q-J. *Liao*, L-B. *Ye*, K.A. *Timani*, Y-C *Zeng*, Y-L. *She*, L. *Ye et al.* Activation of NF-kappaB by the Full-length Nucleocapsid Protein of the SARS Coronavirus. *Acta BiochimBiophys Sin*, 2005, v.37, №9, p.607-12. doi: 10.1111/j.1745-7270.2005.00082.x.
- [53] M.L. *DeDiego*, J.L. *Nieto-Torres*, J.A. *Regla-Nava*, J.M. *Jimenez-Guardeno*, R. *Fernandez-Delgado*, C. *Fett et al.* Inhibition of NF-kappaB-Mediated Inflammation in Severe Acute Respiratory Syndrome Coronavirus-Infected Mice Increases Survival. *J.Virol*, 2014, v. 88, №2, p. 913-24. doi: 426 10.1128/JVI.02576-13.
- [54] C. *Kretz-Remy*, A-P. *Arrigo*. Selenium: A key element that controls NF-kB activation and IkB α half life. *BioFactors*, 2001, v.14, №1-4, p.117-25. doi: 10.1002/biof.5520140116
- [55] H-S. *Youn*, H.J. *Lim*, Y.J. *Choi*, J.Y. *Lee*, M-Y. *Lee*, J-H. *Ryu*. Selenium suppresses the activation of transcription factor NF-kB and IRF3 induced by TLR3 or TLR4 agonists. *IntImmunopharmacol*, 2008, v.8, No.3, p.495-501. doi: 10.1016/j.intimp.2007.12.008.
- [56] E.M. *Campbell*, T.J. *Hope*. HIV-1 capsid: the multifaceted key player in HIV-1 infection. *NatureReviewsMicrobiology*, 2015, v.13, №8, p.471-483.
- [57] R. *Jayawardena*, P. *Sooriyaarachchi*, M. *Chourdakis*, C. *Jeewandara*, P. *Ranasinghe*. Enhancing immunity in virus infections, with special emphasis on COVID-19: A review. *Diabetes&MetabolicSyndrome: ClinicalResearch&Reviews* 2020, v.14, №4, p.367-82.
- [58] P. *Metha et.all.* COVID-19: consider cytokine storm syndromes and immuno suppression, Published Online, 2020 [https://doi.org/10.1016/S0140-6736\(20\)30628-0](https://doi.org/10.1016/S0140-6736(20)30628-0).
- [59] C.S. *Broome*, E. *McArdle*, J.A.M. *Kyle et al.* An increase in selenium intake improves immune function and poliovirus handling in adults with marginal selenium status *Am. J. Clin. Nutr.* 2004, v.80, p.154-162.

- [60] J.R. Arthur, R.C. McKenzie, G.J. Beckett. Selenium in the Immune System. *Journal of Nutrition*, 2003, v.133, №5, p.1457S–1459S.
- [61] K.M. Brown, K. Pickard, F. Nicol, G.J. Beckett, G.G. Duthie, J.R. Arthur. Effects of organic and inorganic selenium supplementation on selenoenzyme activity in blood lymphocytes, granulocytes, platelets and erythrocytes. *ClinSci*, 2000, v.98, №5, p.593-599. doi: 10.1042/cs0980593.
- [62] J. Avery, P. Hoffmann. Selenium, Selenoproteins, and Immunity. *Nutrients*, 2018, v.10, №9, p.1203. doi: 10.3390/nu10091203.
- [63] 61a. Z. Huang, A.H. Rose, P.R. Hoffmann. The role of selenium in inflammation and immunity: from molecular mechanisms to therapeutic opportunities. *Antioxid Redox Signal*, 2012, v.16, p.705-743.
- [64] Z. Varga, A.J. Flammer, P. Steiger, M. Haberecker, R. Andermatt, A.S. Zinkernagel, et al. Endothelial cell infection and endotheliitis in COVID-19. *The Lancet* 2020, v.10234, p.1417-1418. doi: 10.1016/S0140-6736(20)30937-5.
- [65] M. Ackermann et al., Pulmonary Vascular Endothelialitis, Thrombosis, and Angiogenesis in Covid-19, *The New England Journal of Medicine*, 2020, [10.1056/NEJMoa2015432](https://doi.org/10.1056/NEJMoa2015432)
- [66] G. Lippi, M. Plebani, B.M. Henry. Thrombocytopenia is associated with severe coronavirus disease 2019 (COVID-19) infections: A meta-analysis. *Clin Chim Acta*, 2020, v. 506, p. 145-148. doi: 473 10.1016/j.cca.2020.03.022.
- [67] S. Miller, S.W. Walker, J.R. Arthur, F. Nicol, K. Pickard, M.H. Lewin et al. Selenite protects human endothelial cells from oxidative damage and induces thioredoxinreductase. *ClinSciLondEngl.*, 2001, v.100, №5, p.543-550.
- [68] G. Perona, R. Schiavon, G.C. Guidi, D. Veneri, P. Minuz. Selenium Dependent Glutathione Peroxidase: A Physiological Regulatory System for Platelet Function. *ThrombHaemost*, 1990, v. 64, № 2, p. 312-318. doi: 10.1055/s-0038-1647308.
- [69] P.A. Poluboryaninov, D.G. Elistratov, V.I. Shvets. Metabolism and mechanism of toxicity of selenium-containing drugs used to correct deficiency of the microelement selenium, *g. Fine chemical technologies*, v. 14, No. 1, 2019, p. 5-24 DOI 10.32.362 / 2410-6593-2019-14-1-5-24.
- [70] M.J. Parnham, H. Sies. The early research and development of Ebselen *J. Biochem. Pharmacol.* 2013. v. 86. № 9, p.1248–1253.
- [71] G.K. Azad, R.S. Tomar. Ebselen, a promising antioxidant drug: mechanisms of action and targets of biological pathways. *Molecular Biology Reports*, 2014, v.41, №8, p.4865–4879, doi:10.1007/s11033-014-3417-x.
- [72] R. Zhao, H. Masayasu, A. Holmgren. Ebselen: A substrate for human thioredoxinreductase strongly stimulating its hydroperoxidoreductase activity and a superfast thioredoxin oxidant. *Proceedings of the National Academy of Sciences*, 2002, v.99, №13, p.8579–8584, doi:10.1073/pnas.122061399.
- [73] D. Bhowmick, S. Srivastava, P. D'Silva, G. Mugesh. Highly efficient glutathione peroxidase and peroxiredoxinmimetics protect mammalian cells against oxidative damage. *Angew. Chem. Int. Ed. Engl.*, 2015, v.54, p.8449–8453.
- [74] L. Carroll. Interaction kinetics of selenium-containing compounds with oxidants. *FreeRadic. Biol. Med.*, 2020, v.155, p.58–68.
- [75] D.W. Zhang. The selenium-containing drug Ebselen potently disrupts LEDGF/p75-HIV-1 integrase interaction by targeting LEDGF/p75. *J. Enzym. Inhib. Med. Chem.*, 2020, v.35, p.906–912.
- [76] Z. Jin. Structure of M (pro) from SARS-CoV-2 and discovery of its inhibitors. *Nature*, 2020, v.582, p.289–293.
- [77] H. Sies, M.J&Parnham. (2020). Potential therapeutic use of Ebselen for COVID-19 and other respiratory virus infections. *Free Radical Biology and Medicine*. doi:[10.1016/j.freeradbiomed.2020.06.032](https://doi.org/10.1016/j.freeradbiomed.2020.06.032)
- [78] H.M. Mengist, X. Fan, T. Jin. Designing of improved drugs for COVID-19, Crystal structure of SARS-CoV-2 main protease M (pro)., *Signal. Transduct. Target Ther.* 5, 2020, doi: 10.1038/s41392-020-0178-y.
- [79] R.S. Joshi et al. Discovery of potential multi-target-directed ligands by targeting host-specific SARS-CoV-2 structurally conserved main protease. *J. Biomol. Struct. Dyn.*, 2020, 1-16, doi: 10.1080/07391102.2020.1760137.
- [80] L. Zhang et al. Crystal structure of SARS-CoV-2 main protease provides a basis for design of improved alpha-ketoamide inhibitors. *Science*, 2020, v.368, p.409-412.
- [81] M.L. Reshi, Y.C. Su, J.R. Hong. RNA Viruses: ROS-Mediated Cell Death. *Int. J. Cell Biol.* 2014, 2014:467452, doi: 10.1155/2014/467452.
- [82] L. Delgado-Roche, F. Mesta. Oxidative Stress as Key Player in Severe Acute Respiratory Syndrome Coronavirus (SARS-CoV) Infection. *Arch. Med. Res.*, 2020, v.51, p.384- 387.
- [83] H. Sies, D.P. Jones. Reactive oxygen species (ROS) as pleiotropic physiological signalling agents. *Nat. Rev. Mol. Cell Biol.*, 2020, doi: 10.1038/s41580-020-0230-3.
- [84] C.A. Menendez, F. Bylehn, R. Gustavo. Molecular Characterization of Ebselen Binding Activity to SARS-CoV-2 Main Protease, *Cornell University, Quantitative Biology, Biomolecules*, 20 May 2020.

Received: 20.10.2020

AB INITIO CALCULATION Al, Co, Sr DOPED GRAPHENE

S.S. HUSEYNOVA, S.O. MAMMADOVA, A.A. SADIGOVA

*Institute of Physics of ANAS, H.Javid ave., 131,
AZ1143 Baku, Azerbaijan*

This paper introduces the results of first-principle calculations of the electronic and magnetic properties of graphene doped by Al, Co, Sr. In according to theoretical calculations by doping Co and Al graphene energy gap is opened. Furthermore, substitution of the Sr atom for a carbon atom in graphene increases magnetization. In addition, density of state was explored for Al, Co, Sr atoms doping of the graphene structure.

Keywords: first-principle calculations, DFT, ATK, graphene, Al, Co, Sr-doped, supercell, DOS, magnetic moment.

PACS: 31.10.+z, 31.15.E-, 75.50.Gg.

INTRODUCTION

Graphene is a zero band gap semiconductor or semimetal which consists of an sp^2 hybridized single atomic layer of carbon atoms organized in a hexagonal lattice. Each of tetravalent carbon atoms, connect to three neighboring atoms by covalent bonds, which left a free electron on each carbon atom. These free electrons lead to the high electron mobility and high conductivity of graphene. Graphene has also the advantage of being atomically thin conductive material [1-4].

Ferromagnetic properties for alkaline earth doped graphene such as Mg-graphene, Sr-graphene and Ba-graphene were predicted [5]. The calculations are devoted to the evaluation of electric properties of zigzag graphene nanoribbons influenced by the doping of Co [6,7] and Au [8]. Many studies about transition metal incorporated with armchair graphene nanoribbons have been conducted, such as Mn [9], Fe [10], and Ni [11]. In [6] reported an *ab initio* study of atomic and electronic structure of Co atoms incorporated in graphene nanoribbon with armchair-shaped edges.

In according to the electronic, optical, thermal, magnetic, mechanical and electrochemical properties of graphene become attractive for studying in various fields of research, such as electronics [12], optoelectronics [12,13], energy conversion and storage devices [14,15], sensors [16,17] and biomedicine [18,19]. In [20] have overviewed recent methods adopted to the electronic and magnetic properties of graphene and the possible practical applications of these methods in various areas of research. In addition, the challenges faced by individual methods are also included.

The energy gap (E_g) of Al doped graphene [21] is opened upon adsorption of (CO, CO₂, NH₃, NO, NO₂ and SO₂) in various way. The Al doped graphene with NO gas adsorption has the ability to donate electron; it needs to small energy to remove an electron to become a cation. To overcome the insensitivity of these molecules on pristine graphene, doped graphene will be appreciated because of the formation of a 3D structure. It is set that doping graphene with metals the higher sensitivity of graphene toward different molecules could be

achieved [22–24]. Doping causes an improvement in the electronic behavior of the semiconductor materials. For instance, behind doping with B or N atoms, graphene expanded into p-type or n-type correspondingly [25]. Theoretical studies demonstrated that the doped atom on graphene could transform the band structure as well as the electron transfer so the applications of graphene could be mainly enhanced [26–28]. Among diverse metals, Al, Ag, Cu, Au, and Pt are the atoms which have been the most utilized for the doping of graphene [29]. By doping graphene with Al, the electron density around the doped atom reduces because of catching electron by surrounding C-atoms.

COMPUTATIONAL DETAILS

The electronic properties of vacancy in graphene was studied by the density functional theory (DFT) method within the Generalized Gradient Approximation (GGA). The band structure (BS) and density of states (DOS) have been calculated. DFT have been performed to explore the electronic and magnetic properties of graphene doped Al, Co, Sr. The magnetic moments calculation were down by Mulliken population analysis.

First-principles calculations based on the spin-polarized density functional theory, were performed using the periodic Atomistix Tool Kit (ATK). The generalized gradient approximation in the Perdew–Burke–Ernzerhof (PBE) parameterization was employed for the exchange–correlation functional. The kinetic cut-off energy was 150 Ry. The primitive cell of Graphene was relaxed and optimized with force and stress tolerances of 0.01eV/Å and 0.01eV/Å³, respectively. A 4 x 4 x 1 k point was used for geometry optimization and total energy calculations. Our calculations were performed for a number of supercells with as many atoms as 18.

Al, Co, Sr-DOPED IN GRAPHENE

In result of our theoretical calculations we observed that energy gap opening of graphene by doping Co and Al. We calculated the energy gap for Co and Al is $E_g=0.76\text{eV}$, $E_g=0.375\text{eV}$ respectively. Figure 1 displays the Projected Density of States

(PDOS) which was constructed for s-, p- and d-electrons of Al atom in the 18-atom graphene supercell. The upper curve correspond to electrons with the direction of the spin up and the lower the direction of the spin down. Ab initio calculation

PDOS for graphene showed that Fermi level for the p, s, d- electrons with spin-up and spin-down are almost similar [Fig. 1 b,c,d]. In figure 1-d is shown for the spin-down and spin up d- state below Fermi level.

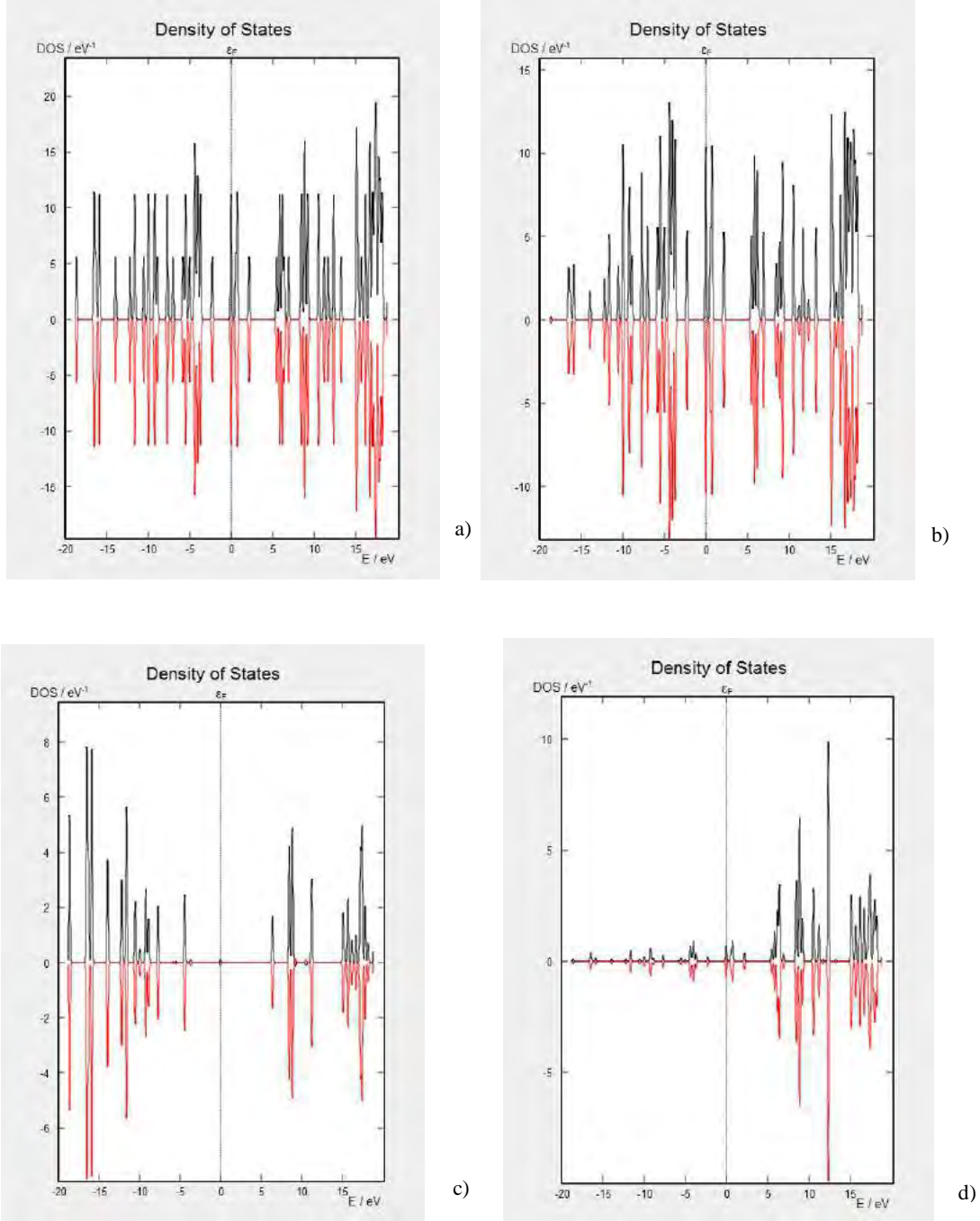


Fig. 1. The DOS for spin up and spin down p-, s-, d- electrons of the dopant Al atom in the 18 atom supercell: a) DOS, b) p-state, c) s-state, d) d-state.

Figure 2 illustrates the atomic structure of the Sr doped graphene plane and density of state.

In addition, this paper is devoted to investigation of magnetic properties of graphene doped with Sr (Fig. 2). In case of Sr atom substituted C 18 atoms in

graphene calculated magnetic moment acquired 1,349 μ B. According to calculations, Sr (C) substitution leads to the ferromagnetic (FM) spin ordering.

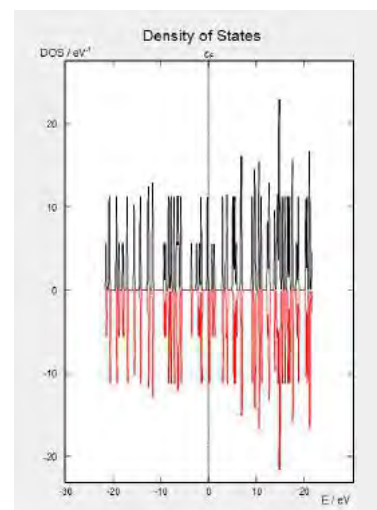
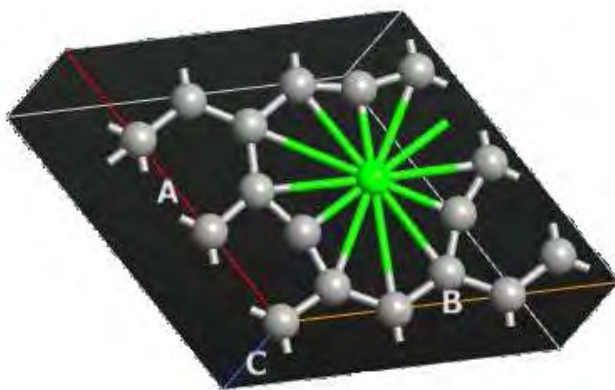


Fig. 2. Sr doped 18 atoms graphene.

CONCLUSIONS

Ab initio calculated electronic and magnetic properties of Al, Co, Sr atoms doped graphene. To simulate the doping effect, we have introduced our calculations for 18 atom-contained supercells. In addition, our investigation demonstrated that Sr doping graphene is an effective route to obtain a magnetization. Total magnetic moment derived from Mulliken population analysis in the graphene by doping Sr is $1,349\mu\beta$. In this paper has been also

explored theoretically that in supercell constitute of 18 atom graphene carbon atom substitution with Al and Co this supercell appeared band gap 0.375eV, 0.76eV, respectively. Note that, we investigated density of state for graphene structure by the doping of Al, Co, Sr atoms.

According to providing theoretical program packet we are grateful to Guliyev Jeyhun programmer of the Institute of Physics.

- [1] K.S. Novoselov, A.K. Geim, S.V. Morozov, D. Jiang, Y. Zhang, S.V. Dubonos, I.V. Grigorieva, A.A. Firsov. Electric field effect in atomically thin carbon films, *Science* 306 (5696) (2004) 666–669.
- [2] K.S. Novoselov, D. Jiang, F. Schedin, T.J. Booth, V.V. Khotkevich, S.V. Morozov, A.K. Geim. Two-dimensional atomic crystals, *Proc. Natl. Acad. Sci. U.S.A* 102 (30) (2005) 10451–10453.
- [3] L. Wirtz, A. Rubio. The phonon dispersion of graphite revisited, *Solid State Commun.* 131 (3) (2004) 141 – 152.
- [4] L. Malard, M. Pimenta, G. Dresselhaus, M. Dresselhaus. Raman spectroscopy in graphene, *Phys. Reports* 473 (5) (2009) 51 – 87.
- [5] A.C.F. Serrano, A.A.B. Padima, J.A. Del Rosario, J.D. Ocon. *ECS Transactions*, 77 (11) 629-636 2017.
- [6] A.T. Lee and K.J. Chang. *Physical Review B*, vol. 87, no. 8, Article ID 085435, 2013.
- [7] S. Lisenkov, A.N. Andriotis, and M. Menon. *Physical Review Letters*, vol. 108, no. 18, Article ID 187208, 2012.
- [8] X.-H. Hu, W. Zhang, L.-T. Sun, and A.V. Krasheninnikov. *Physical Review B*, vol. 86, no. 19, Article ID 195418, 2012.
- [9] S.S. Chauhan, P. Srivastava and A.K. Shrivastava. *Solid State Communications*, 2013. vol. 154, no. 1, pp. 69–71.
- [10] N.K. Jaiswal and P. Srivastava. *IEEE Transactions on Nanotechnology*, vol. 12, no. 5, pp. 685–691, 2013.
- [11] N.K. Jaiswal and P. Srivastava. *Solid State Communications*, vol. 151, no. 20, pp. 1490–1495, 2011.
- [12] D. Jariwala, V.K. Sangwan, L.J. Lauhon, T.J. Marks and M.C. Hersam. *Chem. Soc. Rev.*, 2013, 42, 2824–2860.
- [13] B.H. Nguyen and V.H. Nguyen. *Adv. Nat. Sci.: Nanosci. Nanotechnol.*, 2016, 7, 013002.
- [14] W. Lv, Z. Li, Y. Deng, Q.-H. Yang and F. Kang. *Energy Storage Materials*, 2016, 2, 107–138.
- [15] N. Mahmood, C. Zhang, H. Yin and Y. Hou. *Mater. Chem. A*, 2014, 2, 15–32.
- [16] S.S. Varghese, S. Lonkar, K. Singh, S. Swaminathan and A. Abdala. *Sens. Actuators, B*, 2015, 218, 160–183.
- [17] Y. Shao, J. Wang, H. Wu, J. Liu, I. A. Aksay and Y. Lin, *Electroanalysis*, 2010, 22, 1027–1036.
- [18] S. Kumar and K. Chatterjee. *ACS Appl. Mater. Interfaces*, 2016, 8, 26431–26457.
- [19] R. Zhou and H. Gao. *WIREs Nanomed. Nanobiotechnol.*, 2014, 6, 452–474.
- [20] Salma Nigar, Zhongfu Zhou, Hao Wang and Muhammad Imtiaz. Modulating the electronic and magnetic properties of graphene, (Review Article) *RSC Adv.*, 2017, 7, 51546-51580 DOI: 10.1039/C7RA08917A.

- [21] *Jappor, Hamad Rahman; Khudair, Salah Abdul Mahdi*. American Scientific Publishers, Volume 15, Number 12, December 2017, pp. 1023-1030(8), doi.org/10.1166/sl.2017.39011023
- [22] *Y. Chen, X.C. Yang, .J. Liu, J.X. Zhao, Q.H. Cai, X.Z. Wang*. J.Mol.Graph.Model. 39 (2013) 126.
- [23] *Z. Ao, J. Yang, S. Li, Q. Jiang*. Chem. Phys. Lett. 461 (2008)276.
- [24] *S. Sharma, A.S. Verma*. Physica B 427 (2013) 12.
- [25] *A. Shokuhi Rad, A. Shadravan, A.A. Soleymani, N.Motaghedi*. Curr.Appl. Phys. 15 (2015) 1271.
- [26] *M. Deifallah, P.F. McMillan, F. Cora*. Phys.Chem.C 112 (2008)5447.
- [27] *F. Cervantes-Sodi, G. Csanyi, S. Piskanec, A.C. Ferrari*. Phys.Rev.B77 (2008)165427.
- [28] *L. Ferrighi, M. Datteo, C.D. Valentin*. J.Phys.Chem.C 118 (2014)223.
- [29] *G. Giovannetti, P.A. Khomyakov, G. Brocks, V.M. Karpan, J. vandenBrink, P.J.Kelly*. Phys.Rev. Lett.101 (2008) 026803.

Received:27.10.2020

THE THERMAL POWER AND CONDUCTIVITY OF SUPERCONDUCTING $\text{Bi}_2\text{Sr}_2\text{Ca}_{0.4}\text{Zn}_{0.6}\text{Cu}_2\text{O}_y$

G.I. AGAYEVA

Institute of Physics of Azerbaijan National Academy of Sciences

H. Javid ave., 131, AZ-1143, Baku, Azerbaijan

E-mail: agayevagunel@myrambler.ru

The temperature dependence of the resistivity and thermoelectric power of bismuth $\text{Bi}_2\text{Sr}_2\text{Ca}_{0.4}\text{Zn}_{0.6}\text{Cu}_2\text{O}_y$ superconductor in the range 77-320K is carried out. The experimental results on thermoelectric power are analyzed within the framework of the Xin's two-band model and the band gap of Bi-O layers is determined as $E_g=0.059$ eV.

Keywords: superconducting material, specific resistivity, thermal power.

PACS: 74.62.Bf; 74.25.F

1. INTRODUCTION

The discovery of high-temperature superconductors $\text{La}_{2-x}(\text{Ba}/\text{Sr})_x\text{CuO}_4$ and $\text{YBa}_2\text{Cu}_3\text{O}_{7-x}$ with critical superconducting transition temperatures $T_c \sim 40\text{K}$ and $T_c \sim 90\text{K}$, respectively, led to an intensive search for new oxide superconductors with even higher T_c . Michel et al. [1] reported the discovery of superconductivity between 7 and 22K in Bi-Sr-Cu-O, which was not a rare earth element. However, due to the great interest in yttrium superconductors with a critical temperature of 90 K, this report did not generate wide interest. However, the addition of the element Ca to the Bi-Sr-Cu-O cuprate system led to the discovery of bulk superconductivity at 85K and the proof of superconductivity up to 110K in the Bi-Sr-Ca-Cu-O system [2].

It is known that in bismuth superconductors there are phases with different numbers of CuO (n) atomic planes [3, 4]. With an increase in the number of planes to $n=3$, the critical temperature increases to $T_c = 110\text{K}$.

Investigation of the transport properties of bismuth superconductors $\text{Bi}_2\text{Sr}_2\text{CuO}_6$ ($n=1$), $\text{Bi}_2\text{Sr}_2\text{CaCu}_2\text{O}_8$ ($n=2$) and $\text{Bi}_2\text{Sr}_2\text{Ca}_2\text{Cu}_3\text{O}_{10}$ ($n=3$) have been devoted to many works [1-7]. However, there is still no consensus on the mechanism of HTSC superconductivity. The transport properties of the normal state of HTSC, namely, the linear temperature dependence of the resistivity in a wide temperature range, as well as the strong dependence of the thermoelectric power on the hole concentration in the CuO_2 layers are unusual.

It is known that the coherence length of HTSC is rather small. This leads to the fact that structural inhomogeneities such as double boundaries, defects, grain boundaries, etc., will affect the transport properties of the superconductor in the normal state. The introduction of various impurities and various modes of synthesis affect both the phase formation and the physical properties in this system. On the other hand, atomic-crystal defects arising due to distortions of superconducting CuO_2 layers, as well as point defects in layers formed by calcium atoms when they are replaced with various elements, are pinning centers in Bi based high-temperature superconductors.

Therefore, it is of interest to replace the element Ca by others, in particular, zinc.

This paper analyzes the results of studying transport properties, such as resistivity and thermoelectric power of $\text{Bi}_2\text{Sr}_2\text{Ca}_{0.4}\text{Zn}_{0.6}\text{Cu}_2\text{O}_8$.

2. EXPERIMENTAL RESULTS AND DISCUSSION

The investigated superconducting composition $\text{Bi}_2\text{Sr}_2\text{Ca}_{0.4}\text{Zn}_{0.6}\text{Cu}_2\text{O}_8$ was obtained by solid-phase synthesis, mixing in a stoichiometric proportion of highly pure powders Bi_2O_3 , CaCO_3 , SrCO_3 , ZnO and CuO . The sample was annealed for 10 hours at a temperature of 840°C , then cooled at a rate of $1.5^\circ\text{C}/\text{min}$ to room temperature.

X-ray structural analysis was carried out on a Bruker-D2 Phaser at room temperature with a resolution of $\Delta(2\theta)=0.05^\circ$ in the range $5^\circ \leq 2\theta \leq 80^\circ$. The obtained result is shown in Fig. 1. Some structural parameters of the investigated sample were determined from the data of X-ray structural analysis.

It was found that $\text{Bi}_2\text{Sr}_2\text{Ca}_{0.4}\text{Zn}_{0.6}\text{Cu}_2\text{O}_y$ consists of two phases. The main phase corresponds to the orthorhombic Pnnn group with lattice parameters $a=5,429$, $b=5,431$, $c=30,840$ Å. And the other phase is the tetragonal I4/mmm group with lattice parameters $a=3.8097$, $c=24.607$ Å, respectively. According to the intensities of the diffraction peaks, the tetragonal phase prevails.

The crystallographic structure of bismuth high-temperature superconductors is given in [8, 9]. The crystal structure can be considered as a three-dimensional packing of $\text{Bi}_2\text{Sr}_2\text{CaCu}_2\text{O}_8$ along the c axis, the main feature of which is the presence of two Bi-O layers separated by 3.0 Å and shifted relative to each other (crystallographic shift) in the diagonal direction of the perovskite subcell. Tarascan et al. [10] showed that the 100K phase has the formula Bi-2:2:2:3 and its structure contains three CuO_2 layers. The three phases Bi-Sr-Ca-Cu-O can be represented by the general formula $\text{Bi}_2\text{Sr}_2\text{Ca}_n\text{Cu}_n\text{O}_y$ ($n=1, 2$ and 3) and have a pseudo-tetragonal structure (Fig. 2), which can be described as the packing of the basic block $\text{Bi}_2\text{Sr}_2\text{CuO}_6$ with zero, one or two inserted CaCuO_2 plates.

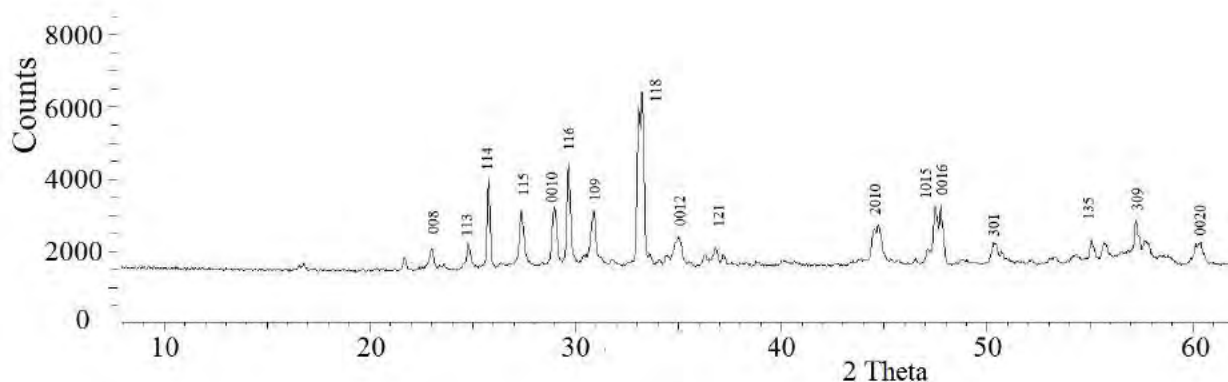


Fig.1. X-ray diffractogram of $\text{Bi}_2\text{Sr}_2\text{Ca}_{0.4}\text{Zn}_{0.6}\text{Cu}_2\text{O}_8$.

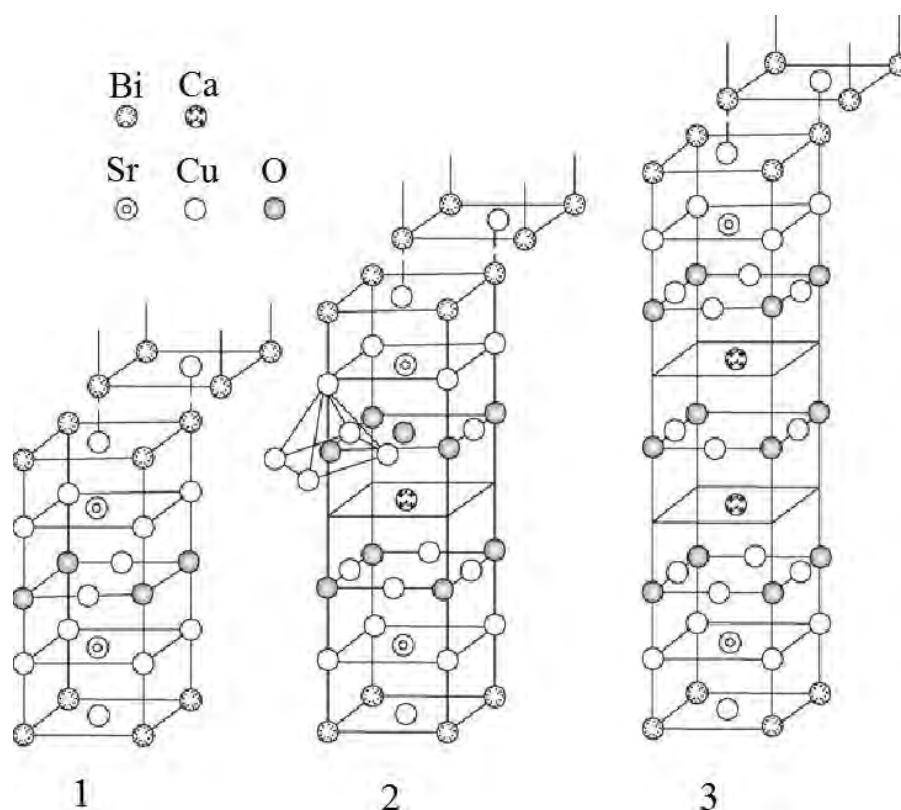


Fig. 2. Crystallographic structure of bismuth superconductors: 1- $\text{Bi}_2\text{Sr}_2\text{CuO}_{6+y}$ ($c=24.6 \text{ \AA}$); 2- $\text{Bi}_2\text{Sr}_2\text{CaCu}_2\text{O}_{8+y}$ ($c=30.7 \text{ \AA}$); 3- $\text{Bi}_2\text{Sr}_2\text{Ca}_2\text{Cu}_3\text{O}_{10+y}$ ($c=37.1 \text{ \AA}$) [11].

The lattice parameter - c increases from 24.6 to 30.6 \AA and finally to 37.1 \AA when going from $n = 1$ to 2 and 3. This increase is the result of the gradual addition of 2×1 and 2×2 (doubled from - due to crystallographic shift) CaCuO_2 , each with a thickness of about 3 \AA , packing sequence in a unit cell. For $\text{Bi}_2\text{Sr}_2\text{CaCu}_2\text{O}_8$, the folding sequence is Bi-Sr-Cu-Ca-Cu-Sr-Bi. In $\text{Bi}_2\text{Sr}_2\text{Ca}_2\text{Cu}_3\text{O}_{10}$ the sequence of layers is Bi-Sr-Cu-Ca-Cu-Ca-Cu-Sr-Bi.

As can be seen from the crystal structure, the element Ca plays an essential role in the critical temperature of a bismuth superconductor. Naturally, it was interesting to determine the effect of the

substitution of zinc for the element calcium on the conductivity and thermo power.

Figures 3 and 4 show the temperature dependences of the resistivity and thermoelectric power of the investigated superconductor. As can be seen from the figure, the temperature dependence of the resistivity in the normal state has a linear course and decreases with temperature. This indicates that the concentration of charge carriers increases with temperature. The superconducting critical temperature of $\text{Bi}_2\text{Sr}_2\text{Ca}_{0.4}\text{Zn}_{0.6}\text{Cu}_2\text{O}_8$ was $T_c=78.2\text{K}$. The temperature coefficient of specific resistivity is $dp/dT=1,2 \cdot 10^{-6} \text{ Ohm} \cdot \text{cm/K}$.

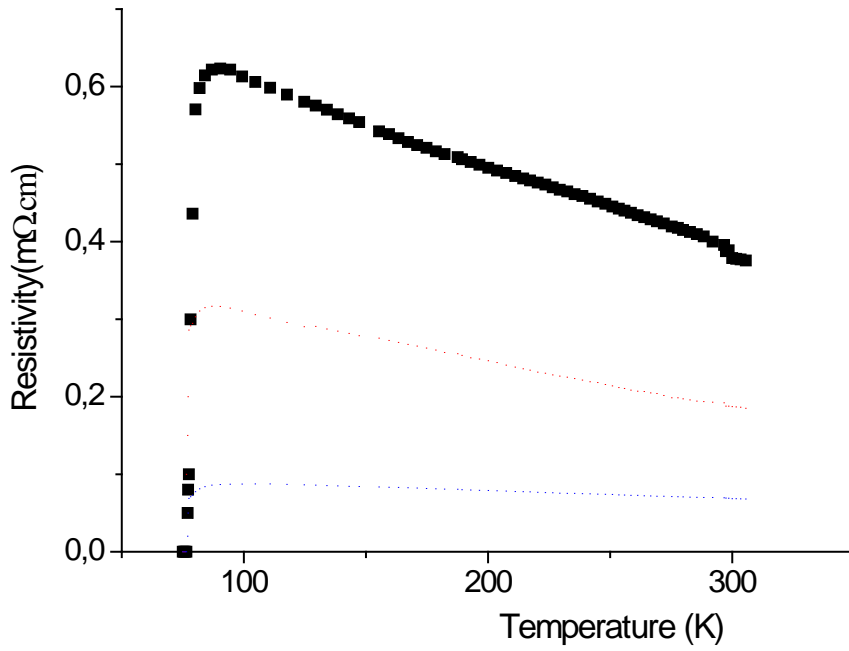


Fig.3. The temperature dependence of specific resistivity of $\text{Bi}_2\text{Sr}_2\text{Ca}_{0.4}\text{Zn}_{0.6}\text{Cu}_2\text{O}_8$.

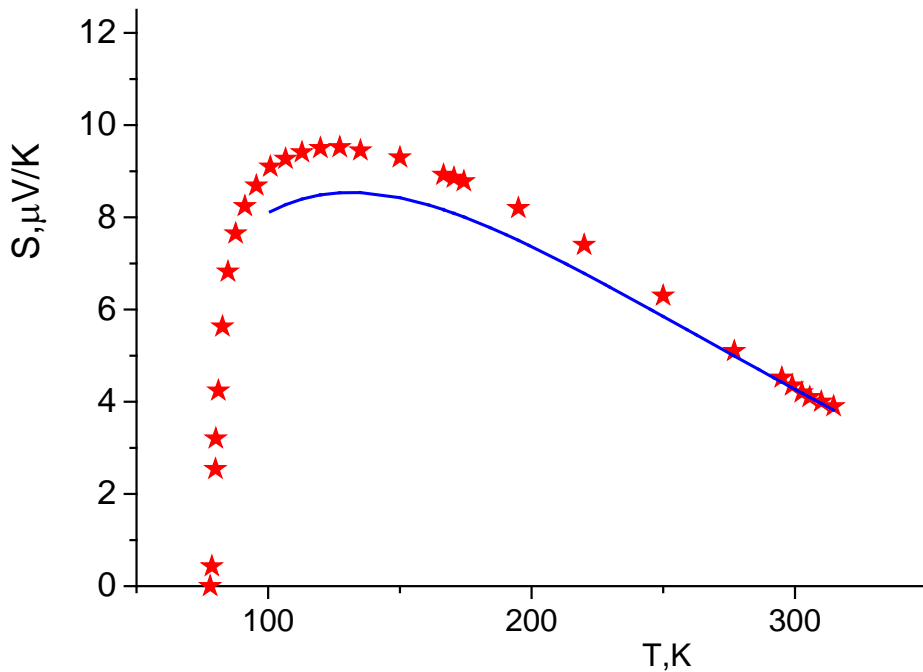


Fig.4. The temperature dependence of thermal power of $\text{Bi}_2\text{Sr}_2\text{Ca}_{0.4}\text{Zn}_{0.6}\text{Cu}_2\text{O}_8$.

In the entire investigated temperature range, the thermopower has a positive sign corresponding to the hole type of conductivity. The $S(T)$ dependence passes through a maximum before the phase transition and sharply decreases to zero with decreasing temperature. In the normal state, the thermoelectric power decreases with increasing temperature. The

temperature of the maximum thermopower is $\sim 117\text{K}$ and has a negative slope $dS/dT = -0,015\mu\text{V}/\text{K}^2$. Hole type of conductivity and negative temperature coefficient of thermoelectric power, indicates the participation of electrons in conduction at the same time. It is known that in bismuth superconductors in

Bi-O layers, electronic conductivity dominates, and in Cu-O, hole conductivity prevails [5, 12, 13].

Xin et al. [3] propose a two-zone model, where one zone is formed by Cu-O and the other by Bi-O planes. The Cu-O plane contributes to the conductivity of holes, while the conduction electrons in the Bi-O planes are of a semiconducting nature. According to [3], the thermopower is determined by the expression:

$$S = -g\pi^2 \left[\frac{d\ln\sigma^+(E)}{d\ln E} \right] T + \left[\frac{E_c}{e} + \frac{k}{e} \frac{d\ln\tau(E)}{d\ln E} T \right] e^{-E_a/kT} \quad (1)$$

Taking into account the linear and exponential parts, expression (2) can be represented as

$$S = AT + (B\lambda + CT)\exp(-\lambda/T) \quad (2)$$

where A, B and C are constants for a given material, T is the temperature, $\lambda = E_c/k_B$, $E_c = E_g/2$ - is the energy gap between the bottom of the conduction band and the middle of the band gap, k_B is the Boltzmann constant. As can be seen from expression (2), the value of the

constant A determines the contribution of holes in the Cu-O planes.

The obtained value of λ was used to calculate the band gap of the semiconductor type Bi-O layers. The parameter λ , which is included in the exponent depends on the band gap between the Bi-O band and the conduction band. From the expression $\lambda = E_c/k_B$ and $E_c = E_g/2$, the band gap of the investigated sample is determined as $E_g = 0.059$ eV. The values of the adjustable constants A, B, C were equal to $A = 0.068 \mu\text{V}/\text{K}^2$, $B = -0.13435 \mu\text{V}/\text{K}^2$, $C = -0.03746 \mu\text{V}/\text{K}^2$, respectively.

CONCLUSION

The temperature dependence of the thermopower of $\text{Bi}_2\text{Sr}_2\text{Ca}_{0.4}\text{Zn}_{0.6}\text{Cu}_2\text{O}_y$ is analyzed within the framework of the Xin's two-band model. The calculation is carried out and the width of the forbidden zone of the semiconductor type Bi-O layers is determined $E_g = 0.059$ eV.

-
- [1] C. Michel et al. Z. Phys. B, 1987, 68(4), p. 421-423.
- [2] H. Maeda et al. Jpn. J. Appl. Phys., 1988, 27(2), L209-L210.
- [3] Y. Xin, K.W. Wong, C.X. Fan, Z. Z. Sheng, and F. T. Chan. Phys. Rev. B, 1993, 48(1), p. 557-561.
- [4] S.S. Ragimov, I.N. Askerzade. Zh. Tekh. Fiz., 2010, 80(10), p. 150-151.
- [5] A.M. Savchenko and M.A. Savchenko. Low Temp. Phys. 2016, 42(10), p. 940-945.
- [6] S.A. Aliev, S.S. Ragimov, V.M. Aliev. Fizika Nizkikh Temperatur (in Russian), 1996, 22(6), p. 679-682.
- [7] S.S. Ragimov, I.N. Askerzade, G.I. Agayeva. J. Supercond. Nov. Magn., 2019, 32(10), p.3033-3036 <https://doi.org/10.1007/s10948-019-5010-y>
- [8] J.M. Tarascon et al., Phys. Rev. B, 1988, 37(16), p. 9382-9389.
- [9] S.A. Sunshine et al., Phys. Rev. B, 38(1), 1988, p. 893-896.
- [10] J.M. Tarascon et al., Phys. Rev. B, 38(13), 1988, p. 8885-8892.
- [11] A.K. Saxena. Crystal Structure of High Temperature Superconductors. In: High-Temperature Superconductors. Springer Series in Materials Science, Springer, Berlin, Heidelberg. vol 125. 2012, https://doi.org/10.1007/978-3-642-28481-6_2.
- [12] V.P.S. Awana, V.N. Moorthy and A.V. Narlikar. Phys. Rev. B, 1994, 49(9), p. 6385-6387.
- [13] M. Chandra Sekhar, S.V. Suryanarayana. Physica C, 2004, 415(4), p. 209-219.

Received: 17.11.2020

THE PRODUCTION OF A CHARGINO PAIR IN POLARIZED LEPTON-ANTILEPTON COLLISIONS (II)

S.K. ABDULLAYEV, M.Sh. GOJAYEV, A.K. GULAYEVA

*Baku State University, Azerbaijan, AZ 1148,
Baku, st. Z. Khalilova, 23, m_qocayev@mail.ru*

Within the framework of the Minimal Supersymmetric Standard Model, the process of annihilation of a lepton-antilepton pair into a pair of charginos is considered: $\ell^- + \ell^+ \rightarrow \tilde{\chi}_i^- + \tilde{\chi}_j^+$. Taking into account the polarization states of the lepton-antilepton pair and the chargino, an analytical expression is obtained for the effective cross section of the process. Diagrams with the exchange of Higgs bosons H , h , A and scalar neutrinos $\tilde{\nu}_L$ are considered in detail. The longitudinal and transverse spin asymmetries caused by the polarizations of the lepton and antilepton, as well as the degrees of the longitudinal and transverse polarization of the chargino, are determined. It is found that the longitudinal spin asymmetry arising from the interaction of polarized leptons with unpolarized antileptons is equal to the longitudinal spin asymmetry arising from the interaction of polarized antileptons with unpolarized leptons.

Keywords: Minimal Supersymmetric Standard Model, Higgs boson, lepton-antilepton pair, chargino, longitudinal spin asymmetry, transverse spin asymmetry.

PACS: 12.10.-g, 12.15.-y, 12.60.-i, 14.80.Ly, 14.70.Bh, 14.70.Hp

1. INTRODUCTION

With the discovery of the Higgs boson H_{SM} at the Large Hadron Collider (LHC) by the ATLAS and CMS collaborations in 2012 [1, 2] (see also reviews [3-5]), a new era in elementary particle physics began. The Standard Model (SM) of fundamental interactions received its logical conclusion and acquired the status of a standard theory. According to SM, there are six leptons and six quarks in nature, making up three generations and three types of interactions: electromagnetic, weak and strong, which are transported by a photon, W^\pm , Z -bosons and gluons (gravitational interaction is still described by Einstein's general theory of relativity). Now they are supplemented by the Yukawa interaction carried by the Higgs boson H_{SM} . Based on the SM, one can calculate Feynman diagrams of various processes and compare them with the corresponding experimental data. The agreement between standard theory and empirical evidence is convincing.

Despite the success of SM, this theory has its own difficulties. One of the difficulties is related to the renormalization of the Higgs boson mass. The fact is that for all SM particles, the mass renormalization works well, and in the case of the Higgs boson H_{SM} a problem arises: the vacuum has a strong effect on the mass of the Higgs boson, its mass increases trillions of times, and such a particle can no longer play the role of the Higgs boson. Note that there is no restraining factor inside the SM that stops the growth of the Higgs boson mass due to virtual particles. Here such a way out of the difficult situation is possible. If there are some other particles in nature that are absent in the SM, then in virtual form they can compensate for the increase in the Higgs boson mass. In the Minimal Supersymmetric Standard Model (MSSM), the compensation of the Higgs boson masses arises by itself by the construction of the theory.

The MSSM introduces two doublets of the scalar field with hypercharges -1 and $+1$ [6-10]:

$$\varphi_1 = \begin{pmatrix} H_1^0 \\ H_1^- \end{pmatrix}, \quad \varphi_2 = \begin{pmatrix} H_2^+ \\ H_2^0 \end{pmatrix}.$$

To obtain physical Higgs bosonic fields φ_1 and φ_2 are written in the form:

$$\varphi_1 = \frac{1}{\sqrt{2}} \begin{pmatrix} \nu_1 + H_1^0 + iP_1^0 \\ H_1^- \end{pmatrix},$$

$$\varphi_2 = \frac{1}{\sqrt{2}} \begin{pmatrix} H_2^+ \\ \nu_2 + H_2^0 + iP_2^0 \end{pmatrix}.$$

Here H_1^0 , P_1^0 , H_2^0 and P_2^0 are the fields describing the excitations of the system with respect to vacuum states $\langle \varphi_1 \rangle = \frac{1}{\sqrt{2}} \nu_1$ and $\langle \varphi_2 \rangle = \frac{1}{\sqrt{2}} \nu_2$.

By mixing the fields H_1^0 and H_2^0 , one obtains CP-even Higgs bosons H and h (mixing angle α):

$$\begin{pmatrix} H \\ h \end{pmatrix} = \begin{pmatrix} \cos \alpha & \sin \alpha \\ -\sin \alpha & \cos \alpha \end{pmatrix} \begin{pmatrix} H_1^0 \\ H_2^0 \end{pmatrix}.$$

Similarly, the fields P_1^0 and P_2^0 are mixed, as well as H_1^\pm and H_2^\pm and get the Goldston bosons G^0 and the CP-odd Higgs boson A , Goldston bosons G^\pm and charged Higgs bosons H^\pm (mixing angle β):

$$\begin{pmatrix} G^0 \\ A \end{pmatrix} = \begin{pmatrix} \cos \beta & \sin \beta \\ -\sin \beta & \cos \beta \end{pmatrix} \begin{pmatrix} P_1^0 \\ P_2^0 \end{pmatrix},$$

$$\begin{pmatrix} G^\pm \\ H^\pm \end{pmatrix} = \begin{pmatrix} \cos \beta & \sin \beta \\ -\sin \beta & \cos \beta \end{pmatrix} \begin{pmatrix} H_1^\pm \\ H_2^\pm \end{pmatrix}.$$

Thus, five Higgs bosons appear in the MSSM:

CP-even H and h bosons, CP-odd A -boson and charged H^\pm -bosons. In this model, the Higgs sector is characterized by mass parameters M_H , M_h , M_A , M_{H^\pm} and angular parameters α and β . Of these,

only two parameters are considered free: mass M_A and angle $\text{tg}\beta$. The rest of the parameters are expressed through them:

$$M_{H(h)}^2 = \frac{1}{2}[M_A^2 + M_Z^2 \pm \sqrt{(M_A^2 + M_Z^2)^2 - 4M_A^2 M_Z^2 \cos^2 2\beta}].$$

$$M_{H^\pm}^2 = M_A^2 + M_Z^2,$$

$$\text{tg}2\alpha = \text{tg}2\beta \frac{M_A^2 + M_Z^2}{M_A^2 - M_Z^2}, \quad \left(-\frac{\pi}{2} \leq \alpha < 0\right),$$

M_Z and M_W – masses of gauge Z - and W^\pm -bosons.

Wine \tilde{W}^\pm and higgsino \tilde{H}^\pm are superpartners of gauge W^\pm - and charged Higgs H^\pm -bosons. The mass matrix of wine \tilde{W}^\pm and higgsino \tilde{H}^\pm is nondiagonal, which results in mixing of these spinor fields. The resulting new particles are called charginos $\tilde{\chi}_{1,2}^\pm$. The masses and constants of interaction with Higgs bosons are determined by the mass matrix [6, 10]

$$M_C = \begin{pmatrix} M_2 & \sqrt{2}M_W \sin \beta \\ \sqrt{2}M_W \cos \beta & \mu \end{pmatrix},$$

where M_2 and μ – are the mass parameters of wine \tilde{W}^\pm and higgsino \tilde{H}^\pm . The matrix M_C is diagonalized by two real two-row matrices U and V . After diagonalizing the matrix M_C , new chargino states with masses are obtained

$$m_{\tilde{\chi}_{1,2}^\pm}^2 = \frac{1}{2}\{M_2^2 + \mu^2 + 2M_W^2 \mp \sqrt{(M_2^2 - \mu^2)^2 + 4M_W^2(M_W^2 \cos^2 2\beta + M_2^2 + \mu^2 + 2M_2\mu \sin 2\beta)}\}.$$

With a very large value of the parameter $|\mu|$ ($|\mu| \rightarrow \infty$), light chargino corresponds to the state of wine with mass $m_{\tilde{\chi}_1^\pm} \approx M_2$, and heavy chargino corresponds to the state of higgsino with mass $m_{\tilde{\chi}_2^\pm} \approx |\mu|$. However, when $M_2 \gg |\mu|$ and $|\mu| \sim M_Z$ both chargino $\tilde{\chi}_1^\pm$ and $\tilde{\chi}_2^\pm$ exchange roles: $m_{\tilde{\chi}_1^\pm} \approx |\mu|$, $m_{\tilde{\chi}_2^\pm} \approx M_2$.

Supersymmetric (SUSY) particles can be produced in the LHC in the decays of squarks and gluinos: $\tilde{g} \rightarrow q + \tilde{q}$, $\tilde{q} \rightarrow q + \tilde{\chi}_i$. One of the main sources of pair production of charginos is high-energy lepton-antilepton (electron-positron and muon-antimuon) colliders of the new generation [11, 12].

In a number of works, the processes of production of a pair of charginos and neutralinos in electron-positron collisions have been considered [14-16].

In the present work, we study the process of creation of a chargino pair upon annihilation of an arbitrarily polarized lepton-antilepton pair:

$$\ell^- + \ell^+ \rightarrow \tilde{\chi}_i^- + \tilde{\chi}_j^+. \quad (1)$$

Taking into account the polarization states of the lepton-antilepton pair and the chargino, an analytical expression is obtained for the effective cross section of reaction (1).

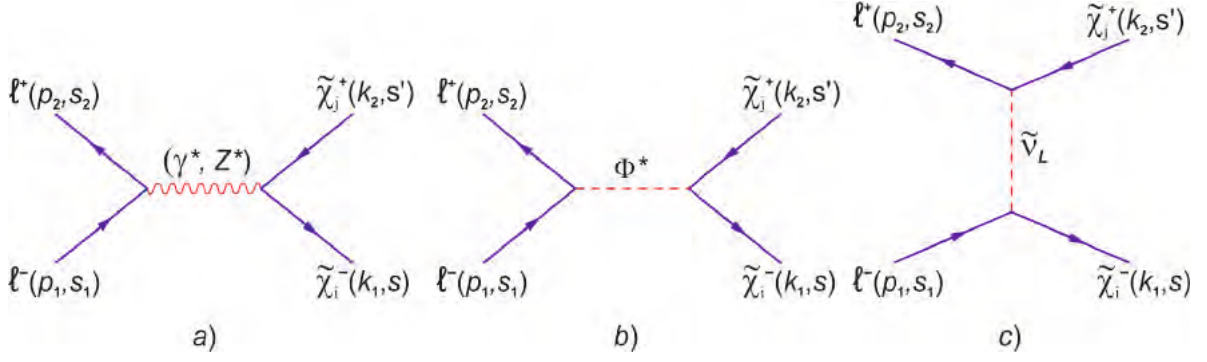
The longitudinal and transverse spin asymmetries caused by the polarizations of the lepton-antilepton pair, as well as the degrees of the longitudinal and transverse polarization of the chargino, have been determined. The dependence of these characteristics and the cross section of reaction (1) was studied depending on the energy of the lepton-antilepton pair and the angle θ .

2. AMPLITUDE AND WIDTH OF DECAY

$$\ell^- \ell^+ \rightarrow \tilde{\chi}_i^- \tilde{\chi}_j^+$$

The annihilation of a lepton-antilepton pair into a chargino pair is described by the Feynman diagrams shown in Fig. 1 a), b) and c) (4-momenta and polarization vectors of particles are written in brackets). Diagram 1a) corresponds to the exchange of a photon and a neutral Z -boson between a lepton-antilepton pair and a chargino pair. This diagram was studied in detail in the first work (I) [13].

The second diagram corresponds to the exchange of a virtual Higgs boson Φ^* (H^* , h^* or A^*). From this diagram for the matrix element of the process $\ell^- + \ell^+ \rightarrow \tilde{\chi}_i^- + \tilde{\chi}_j^+$, we obtain the following expression (we assume that the intermediate Φ^* -boson interacting with the lepton-antilepton pair simultaneously possesses CP-even and CP-odd components):


 Fig. 1. Feynman diagrams of process $\ell^- \ell^+ \rightarrow \tilde{\chi}_i^- \tilde{\chi}_j^+$.

$$M_{i \rightarrow f} = ig_{\Phi \ell \ell} [\bar{v}(p_2, s_2)(a + b\gamma_5)u(p_1, s_1)] \cdot \frac{1}{s - M_\Phi^2 + i\Gamma_\Phi M_\Phi} \times g[\bar{u}(k_1, s)(g_{ijk}^L P_L + g_{ijk}^R P_R)v(k_2, s')]. \quad (2)$$

Here $g_{\Phi \ell \ell}$ – is the constant of interaction of a Φ -boson with a lepton-antilepton pair; a and b – are some constants, and at $a=1$ and $b=0$ the Φ -boson is CP-even (like the bosons H, h), and at $a=0$ and $b=1$ we obtain the CP-odd A -boson; $\frac{1}{s - M_\Phi^2 + i\Gamma_\Phi M_\Phi}$ – Φ -boson propagator; M_Φ and Γ_Φ – its mass and overall width; g – is the constant that determines the mass of the calibration W^\pm -boson

$$M_W^2 = \frac{1}{2} g^2 (v_1^2 + v_2^2);$$

$P_{L,R} = \frac{1}{2}(1 \pm \gamma_5)$ – chirality matrices; $g_{ijk}^L = G_L$ and $g_{ijk}^R = G_R$ – Higgs boson coupling constants H_k ($k=1,2,3$ for H, h, A bosons) with a chargino pair [6-8]:

$$G_L = \frac{1}{\sqrt{2} \sin \theta_W} [U_{i2} V_{j1} e_k - U_{i1} V_{j2} d_k], \quad (3)$$

$$G_R = \frac{1}{\sqrt{2} \sin \theta_W} [V_{i1} U_{j2} e_k - V_{i2} U_{j1} d_k] \varepsilon_k;$$

θ_W – Weinberg angle; $\varepsilon_1 = \varepsilon_2 = 1$, $\varepsilon_3 = -1$; coefficients e_k and d_k are equal:

$$e_1 = +\cos \alpha, \quad e_2 = -\sin \alpha, \quad e_3 = -\sin \beta,$$

$$d_1 = -\sin \alpha, \quad d_2 = -\cos \alpha, \quad d_3 = +\cos \beta.$$

In a standard way, for the square of the amplitude, we find:

$$|M_{i \rightarrow f}|^2 = \frac{g_{\Phi \ell \ell}^2 g^2}{(s - M_\Phi^2)^2 + \Gamma_\Phi^2 M_\Phi^2} \cdot \frac{1}{2} \{ [|a|^2 + |b|^2] [(p_1 \cdot p_2) + m_\ell^2 (s_1 \cdot s_2)] + [|a|^2 - |b|^2] \times$$

$$\times [-m_\ell^2 - (s_1 \cdot s_2)(p_1 \cdot p_2) + (p_1 \cdot s_2)(p_2 \cdot s_1)] - 2 \operatorname{Re}(ab^*) m_\ell [(p_1 \cdot s_2) + (p_2 \cdot p_1)] -$$

$$- 2 \operatorname{Im}(ab^*) p_{1\mu} p_{2\nu} s_{1\rho} s_{2\sigma} \varepsilon_{\mu\nu\rho\sigma} \} \times \{ (G_L^2 + G_R^2) [(k_1 \cdot k_2) + m_{\tilde{\chi}_i^-} m_{\tilde{\chi}_j^+} (s \cdot s')] +$$

$$+ (G_L^2 - G_R^2) [m_{\tilde{\chi}_i^-} (k_2 \cdot s) + m_{\tilde{\chi}_j^+} (k_1 \cdot s')] + 2G_L G_R [-m_{\tilde{\chi}_i^-} m_{\tilde{\chi}_j^+} - (k_1 \cdot k_2)(s \cdot s') + (k_1 \cdot s')(k_2 \cdot s)] \},$$

where m_ℓ – is the lepton mass

Let us find the effective cross section for reaction (1) in the case when the lepton-antilepton pair is polarized arbitrarily, and the chargino pair is polarized longitudinally:

$$\sigma = \frac{g_{\Phi \ell \ell}^2 g^2 s}{2^7 [(s - M_\Phi^2)^2 + \Gamma_\Phi^2 M_\Phi^2]} \sqrt{\lambda(r_{\chi_i}, r_{\chi_j})} \cdot \{ [|a|^2 + |b|^2] [1 - (\vec{n} \cdot \vec{\xi}_1)(\vec{n} \cdot \vec{\xi}_2)] + [|a|^2 - |b|^2] \times$$

$$\times [(\vec{\xi}_1 \cdot \vec{\xi}_2) - (\vec{n} \cdot \vec{\xi}_1)(\vec{n} \cdot \vec{\xi}_2)] + 2 \operatorname{Re}(ab^*) [(\vec{n} \cdot \vec{\xi}_2) - (\vec{n} \cdot \vec{\xi}_1)] - 2 \operatorname{Im}(ab^*) (\vec{n} \cdot \vec{\xi}_1 \vec{\xi}_2) \} \{ (G_L^2 + G_R^2) \times$$

$$\times (1 - r_{\chi_i} - r_{\chi_j})(1 + h_1 h_2) + (G_L^2 - G_R^2)(h_1 + h_2) \sqrt{\lambda(r_{\chi_i}, r_{\chi_j})} - 4G_L G_R (1 + h_1 h_2) \sqrt{r_{\chi_i} \cdot r_{\chi_j}} \}. \quad (4)$$

Here \vec{n} – is the unit vector directed along the lepton momentum; $\vec{\xi}_1$ and $\vec{\xi}_2$ – are unit vectors directed

along the spins of the lepton and antilepton in the rest systems of each of these particles, respectively; h_1 and h_2 – helicity of chargino $\tilde{\chi}_i^-$ and $\tilde{\chi}_j^+$; $s = (p_1 + p_2)^2$ – the square of the total energy of a lepton-antilepton pair in their center-of-mass system; $\lambda(r_{\chi_i}, r_{\chi_j})$ – is the known kinematic function of the two-particle phase volume:

$$\lambda(r_{\chi_i}, r_{\chi_j}) = (1 - r_{\chi_i} - r_{\chi_j})^2 - 4r_{\chi_i}r_{\chi_j},$$

where the notation:

$$\sigma = \frac{g_{\Phi\ell\ell}^2 g^2 s}{2^7 [(s - M_\Phi^2)^2 + \Gamma_\Phi^2 M_\Phi^2]} \sqrt{\lambda(r_{\chi_i}, r_{\chi_j})} \cdot \{[|a|^2 + |b|^2](1 + \lambda_1\lambda_2) - 2\text{Re}(ab^*)(\lambda_1 + \lambda_2)\} \cdot \{(G_L^2 + G_R^2) \times$$

$$\times (1 + h_1h_2)(1 - r_{\chi_i} - r_{\chi_j}) - 4G_LG_R(1 + h_1h_2)\sqrt{r_{\chi_i} \cdot r_{\chi_j}} + (G_L^2 - G_R^2)(h_1 + h_2)\sqrt{\lambda(r_{\chi_i}, r_{\chi_j})}\}. \quad (5)$$

As can be seen from this section, the lepton and antilepton, as well as the charginos $\tilde{\chi}_i^-$ and $\tilde{\chi}_j^+$ separately, must have the same helicities: $\lambda_1 = -\lambda_2 = \pm 1$, $h_1 = h_2 = \pm 1$. Consequently, diagram b) in Fig. 1 corresponds to four spiral sections: lepton-antilepton pair and chargino $\tilde{\chi}_i^-$ and $\tilde{\chi}_j^+$ polarized right ($\lambda_1 = \lambda_2 = h_1 = h_2 = +1$):

$$\sigma_{RRRR} \sim |a - b|^2 \{(G_L^2 + G_R^2)(1 - r_{\chi_i} - r_{\chi_j}) - 4G_LG_R\sqrt{r_{\chi_i}r_{\chi_j}} + (G_L^2 - G_R^2)\sqrt{\lambda(r_{\chi_i}, r_{\chi_j})}\}; \quad (6)$$

lepton-antilepton pair and chargino $\tilde{\chi}_i^-, \tilde{\chi}_j^+$ polarized to the left ($\lambda_1 = \lambda_2 = h_1 = h_2 = -1$):

$$\sigma_{LLLL} \sim |a + b|^2 \{(G_L^2 + G_R^2)(1 - r_{\chi_i} - r_{\chi_j}) - 4G_LG_R\sqrt{r_{\chi_i}r_{\chi_j}} - (G_L^2 - G_R^2)\sqrt{\lambda(r_{\chi_i}, r_{\chi_j})}\}; \quad (7)$$

the lepton-antilepton pair is polarized to the right, and the chargino $\tilde{\chi}_i^-$ and $\tilde{\chi}_j^+$ – to the left

$$\sigma_{RRLL} \sim |a - b|^2 \{(G_L^2 + G_R^2)(1 - r_{\chi_i} - r_{\chi_j}) - 4G_LG_R\sqrt{r_{\chi_i}r_{\chi_j}} - (G_L^2 - G_R^2)\sqrt{\lambda(r_{\chi_i}, r_{\chi_j})}\}; \quad (8)$$

the lepton-antilepton pair is polarized to the left, and the chargino $\tilde{\chi}_i^-$ and $\tilde{\chi}_j^+$ – to the right:

$$\sigma_{LLRR} \sim |a + b|^2 \{(G_L^2 + G_R^2)(1 - r_{\chi_i} - r_{\chi_j}) - 4G_LG_R\sqrt{r_{\chi_i}r_{\chi_j}} - (G_L^2 - G_R^2)\sqrt{\lambda(r_{\chi_i}, r_{\chi_j})}\}. \quad (9)$$

In these cases, the directions of momenta and particle spins are shown in Fig. 2. As can be seen from the figure, the directions of the spins of the lepton-antilepton pair and the chargino $\tilde{\chi}_i^-, \tilde{\chi}_j^+$ are oriented oppositely, therefore, the sum of their spins is equal to zero, the spin of the intermediate Φ -boson is also equal to zero. As noted in the previous work (I), due

$$\ell_L^- + \ell_R^+ \rightarrow \tilde{\chi}_{iL}^- + \tilde{\chi}_{jR}^+; \ell_L^- + \ell_R^+ \rightarrow \tilde{\chi}_{iR}^- + \tilde{\chi}_{jL}^+; \ell_L^- + \ell_L^+ \rightarrow \tilde{\chi}_{iL}^- + \tilde{\chi}_{jR}^+; \ell_R^- + \ell_L^+ \rightarrow \tilde{\chi}_{iR}^- + \tilde{\chi}_{jL}^+.$$

The directions of momenta and particle spins in these spiral processes are shown in Fig. 3. As you can see, in all cases the directions of the spins of the initial (final) particles are parallel to each other, their sum is equal to 1 (in units \hbar). That is how it should be, since the photon and Z-boson carrying the interaction have

$$r_{\chi_i} = \left(\frac{m_{\tilde{\chi}_i^-}}{\sqrt{s}} \right)^2, \quad r_{\chi_j} = \left(\frac{m_{\tilde{\chi}_j^+}}{\sqrt{s}} \right)^2.$$

Let us consider some special cases of the effective cross section (4). First, assume that the lepton-antilepton pair is longitudinally polarized:

$$\vec{\xi}_1 = \vec{n}\lambda_1, \quad \vec{\xi}_2 = -\vec{n}\lambda_2,$$

where λ_1 and λ_2 – are the helicities of the lepton and antilepton. In this case, the effective section (4) takes the form

to the conservation of helicity of particles in the process $\ell^- + \ell^+ \rightarrow (\gamma^*; Z^*) \rightarrow \tilde{\chi}_i^- + \tilde{\chi}_j^+$, the lepton-antilepton pair (also the chargino pair) should have opposite helicities $\lambda_1 = -\lambda_2 = \pm 1$, $h_1 = -h_2 = \pm 1$:

spin 1.

From the above considerations it follows that using left- or right-handed lepton-antilepton beams, it is possible to separate the contribution to the cross section of the diagram b) from the contribution of the diagram a) in Fig. 1.

THE PRODUCTION OF A CHARGINO PAIR IN POLARIZED LEPTON-ANTILEPTON COLLISIONS (II)

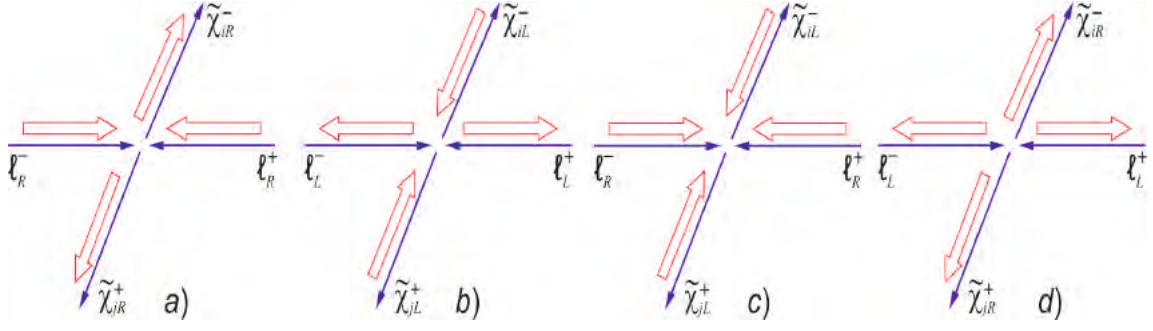


Fig. 2. Directions of momenta and particle spins in the process $\ell^- \ell^+ \rightarrow (\Phi^*) \rightarrow \tilde{\chi}_i^- \tilde{\chi}_j^+$.

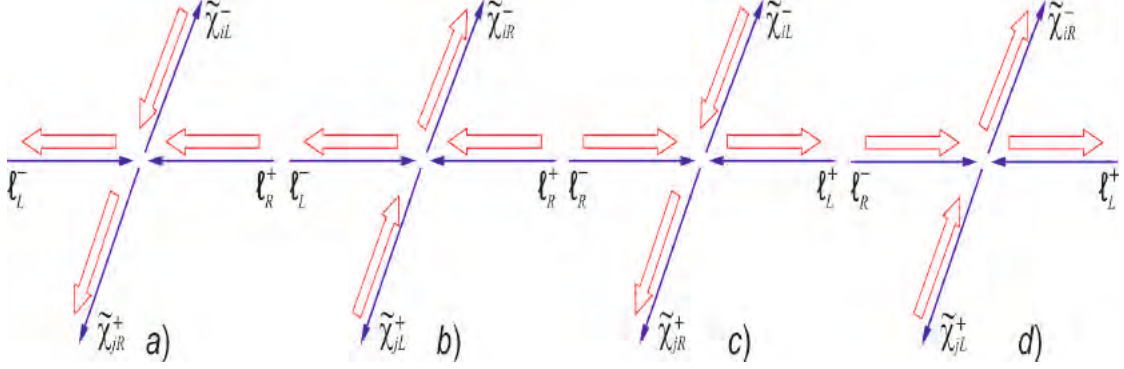


Fig. 3. Directions of momenta and particle spins in the reaction $\ell^- \ell^+ \rightarrow (\gamma^*; Z^*) \rightarrow \tilde{\chi}_i^- \tilde{\chi}_j^+$.

Summing over the chargino polarizations in (5), we represent the resulting expression in the form:

$$\sigma(\lambda_1, \lambda_2) = \frac{g_{\Phi\ell\ell}^2 g^2 s}{32[(s - M_\Phi^2)^2 + \Gamma^2 \Phi^2]} \sqrt{\lambda(r_{\chi_i}, r_{\chi_j})} \cdot \{[|a|^2 + |b|^2](1 + \lambda_1 \lambda_2) - 2 \operatorname{Re}(ab^*) (\lambda_1 + \lambda_2)\} \times \\ \times \{(G_L^2 + G_R^2)(1 - r_{\chi_i} - r_{\chi_j}) - 4G_L G_R \sqrt{r_{\chi_i} \cdot r_{\chi_j}}\}. \quad (10)$$

Let us determine the longitudinal spin asymmetries due to the polarizations of the lepton and antilepton:

$$A_{\ell^-} = \frac{1}{\lambda_1} \frac{\sigma(\lambda_1, 0) - \sigma(-\lambda_1, 0)}{\sigma(\lambda_1, 0) + \sigma(-\lambda_1, 0)} = -\frac{2 \operatorname{Re}(ab^*)}{|a|^2 + |b|^2}, \quad (11)$$

$$A_{\ell^+} = \frac{1}{\lambda_2} \frac{\sigma(0, \lambda_2) - \sigma(0, -\lambda_2)}{\sigma(0, \lambda_2) + \sigma(0, -\lambda_2)} = -\frac{2 \operatorname{Re}(ab^*)}{|a|^2 + |b|^2}.$$

Here $\sigma(\lambda_1, 0)$ ($\sigma(0, \lambda_2)$) – is the annihilation cross section for the interaction of a longitudinally polarized lepton with an unpolarized antilepton (an unpolarized lepton with a polarized antilepton). From expressions (11) it follows that the longitudinal spin asymmetries A_{ℓ^-} and A_{ℓ^+} are equal to each other. This means that

the longitudinal spin asymmetry arising from the interaction of polarized leptons with unpolarized antileptons is equal to the longitudinal spin asymmetry arising from the interaction of polarized antileptons with unpolarized leptons.

Note that the study of longitudinal spin asymmetries can provide valuable information about the CP-even or odd nature of the Higgs boson Φ . If the Φ -boson is a CP-even particle (like the bosons H, h) or a CP-odd particle (like a A -boson), then the experiments will not reveal longitudinal spin asymmetry.

Now suppose the lepton-antilepton pair is transversely polarized. Wherein

$$(\vec{n} \vec{\xi}_1) = (\vec{n} \vec{\eta}_1) = 0, \quad (\vec{n} \vec{\xi}_2) = (\vec{n} \vec{\eta}_2) = 0, \quad (\vec{\xi}_1 \vec{\xi}_2) = (\vec{\eta}_1 \vec{\eta}_2) = \eta_1 \eta_2 \cos \phi,$$

where $\vec{\eta}_1$ and $\vec{\eta}_2$ – are the transverse components of the spin vectors of the lepton and antilepton (at full transverse polarization $\eta_1 = \eta_2 = 1$), ϕ – is the angle between these vectors. In this case, for the effective section of the process $\ell^- + \ell^+ \rightarrow \tilde{\chi}_i^- + \tilde{\chi}_j^+$, the expression is obtained:

$$\sigma(\eta_1, \eta_2) = \frac{g_{\Phi\ell\ell}^2 g^2 s}{32[(s - M_\Phi^2)^2 + \Gamma_\Phi^2 \Phi_\Phi^2]} \sqrt{\lambda(r_{\chi_i}, r_{\chi_j})} \cdot \{|a|^2 + |b|^2 + [|a|^2 - |b|^2] \eta_1 \eta_2 \cos \phi -$$

$$-2 \operatorname{Im}(ab^*) \eta_1 \eta_2 \sin \phi \} [(G_L^2 + G_R^2)(1 - r_{\chi_i} - r_{\chi_j}) - 4G_L G_R \sqrt{r_{\chi_i} \cdot r_{\chi_j}}]. \quad (12)$$

This effective cross section leads to the following transverse spin asymmetries associated with the polarizations of the lepton-antilepton pair:

$$A_1 = \frac{\sigma(\phi = 0) - \sigma(\phi = \pi)}{\sigma(\phi = 0) + \sigma(\phi = \pi)} = \frac{|a|^2 - |b|^2}{|a|^2 + |b|^2} \eta_1 \eta_2, \quad (13)$$

$$A_2 = \frac{\sigma(\phi = -\pi/2) - \sigma(\phi = \pi/2)}{\sigma(\phi = -\pi/2) + \sigma(\phi = \pi/2)} = \frac{2 \operatorname{Im}(ab^*)}{|a|^2 + |b|^2} \eta_1 \eta_2. \quad (14)$$

For a complete transversely polarized lepton-antilepton pair ($\eta_1 = \eta_2 = 1$), we have $A_1 = 1$, if the intermediate Φ -boson is a CP-even boson H or h ($a = 1, b = 0$). For an odd CP $\Phi = A$ boson, the transverse spin asymmetry is $A_1 = -1$ ($a = 0, b = 1$). Hence, by measuring the transverse spin asymmetry A_1 , one can obtain information about the nature of the Higgs boson.

The nonzero transverse spin asymmetry also indicates CP-parity violation in the reaction $\ell^- + \ell^+ \rightarrow (\Phi^*) \rightarrow \tilde{\chi}_i^- + \tilde{\chi}_j^+$.

The effective cross section of the reaction with allowance for the longitudinal polarizations of the chargino can be represented as:

$$\sigma(h_1, h_2) = \frac{1}{4} \sigma_0 [1 + h_1 h_2 + (h_1 + h_2) P_{\parallel}], \quad (15)$$

where

$$\sigma_0 = \frac{g_{\Phi \ell \ell}^2 g^2 \cdot s \sqrt{\lambda(r_{\chi_i}, r_{\chi_j})}}{32[(s - M_{\Phi}^2)^2 + \Gamma_{\Phi}^2 \Phi_{\Phi}^2]} \cdot [|a|^2 + |b|^2] [(G_L^2 + G_R^2)(1 - r_{\chi_i} - r_{\chi_j}) - 4G_L G_R \sqrt{r_{\chi_i} \cdot r_{\chi_j}}] \quad (16)$$

– the effective cross section of the considered process in the case of unpolarized particles, and P_{\parallel} the degree of longitudinal polarization of the chargino

$$P_{\parallel} = \frac{(G_L^2 - G_R^2) \sqrt{\lambda(r_{\chi_i}, r_{\chi_j})}}{(G_L^2 + G_R^2)(1 - r_{\chi_i} - r_{\chi_j}) - 4G_L G_R \sqrt{r_{\chi_i} \cdot r_{\chi_j}}}. \quad (17)$$

If the charginos are transversely polarized, then the cross section of the process under consideration can be represented in the following form:

$$\sigma(\eta, \eta') = \frac{1}{4} \sigma_0 (1 + \eta \eta' P_{\perp}), \quad (18)$$

where

$$P_{\perp} = \frac{2 \cos \varphi \cdot [G_L G_R (1 - r_{\chi_i} - r_{\chi_j}) - (G_L^2 + G_R^2) \sqrt{r_{\chi_i} \cdot r_{\chi_j}}]}{(G_L^2 + G_R^2)(1 - r_{\chi_i} - r_{\chi_j}) - 4G_L G_R \sqrt{r_{\chi_i} \cdot r_{\chi_j}}} \quad (19)$$

– is the degree of transverse polarization of the chargino due to the polarizations η and η' , φ – is the angle between the spin vectors of the chargino $\vec{\eta}$ and $\vec{\eta}'$.

Let us estimate the degree of longitudinal and transverse polarization of the chargino in the processes $\ell^- + \ell^+ \rightarrow \tilde{\chi}_1^- + \tilde{\chi}_1^+, \ell^- + \ell^+ \rightarrow \tilde{\chi}_2^- + \tilde{\chi}_2^+, \ell^- + \ell^+ \rightarrow \tilde{\chi}_1^- + \tilde{\chi}_2^+$ and $\ell^- + \ell^+ \rightarrow \tilde{\chi}_2^- + \tilde{\chi}_1^+$. Calculations show that in all these processes the constants of the interaction of the chargino with the Higgs bosons $\Phi = H, h$ and A $G_L = G_R$, because of this, the degree of longitudinal polarization of the chargino P_{\parallel} vanishes, and the degree of transverse

polarization of the chargino P_{\perp} is equal to the cosine of the angle φ between the spin vectors $\vec{\eta}$ and $\vec{\eta}'$:

$$P_{\perp} = \cos \varphi. \quad (20)$$

In Fig. 4 shows the dependence of the degree of transverse polarization of the chargino P_{\perp} on the angle φ . When $\varphi = 0$ the degree of transverse polarization is maximum and is 1, with an increase in the angle φ , the degree of transverse polarization of the chargino decreases and vanishes at $\varphi = 90^\circ$. Then the sign changes and becomes negative at the end of the angular spectrum at $\varphi = 180^\circ$ $P_{\perp} = -1$.

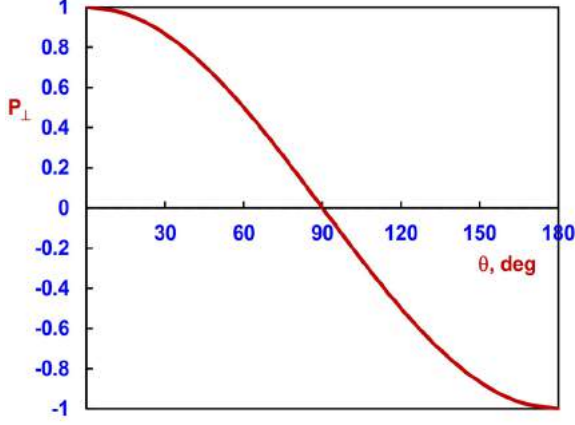


Fig. 4. Dependence of the degree of transverse polarization on the angle φ .

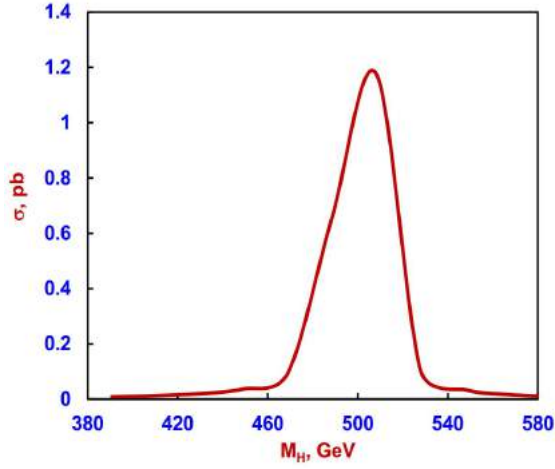


Fig. 5. Dependence of the reaction $\mu^- \mu^+ \rightarrow (H^*) \rightarrow \tilde{\chi}_1^- \tilde{\chi}_2^+$ cross section on the Higgs boson mass.

In Fig. 5 shows the dependence of the cross section of the process $\mu^- + \mu^+ \rightarrow \tilde{\chi}_1^- + \tilde{\chi}_2^+$ at an energy of colliding muon-antimuon beams of $\sqrt{s} = 500$ GeV on the Higgs boson M_H mass. Chargino masses $m_{\tilde{\chi}_1^-}$

and $m_{\tilde{\chi}_2^+}$ are determined at parameter values of $\text{tg}\beta = 1$, $M_2 = 150$ GeV, $\mu = 200$ GeV. The total width of the Higgs boson decay was chosen to be $\Gamma_H = 4$ GeV, and the Weinberg parameter was $x_W = 0.2315$. With an increase in the Higgs boson mass, the effective cross section increases and at $M_H = \sqrt{s} = 500$ GeV reaches its maximum value. Further increase in mass leads to a decrease in the cross section.

Fig. 6 illustrates the dependence of the effective cross section of the process $\mu^- + \mu^+ \rightarrow (H^*) \rightarrow \tilde{\chi}_1^- + \tilde{\chi}_2^+$ on the energy \sqrt{s} of muon-antimuon beams at the same values of the parameters as in Fig. 5. The mass of the Higgs boson is chosen to be $M_H = 600$ GeV. With increasing energy, the cross section increases and reaches its maximum value at $\sqrt{s} = M_H = 600$ GeV.

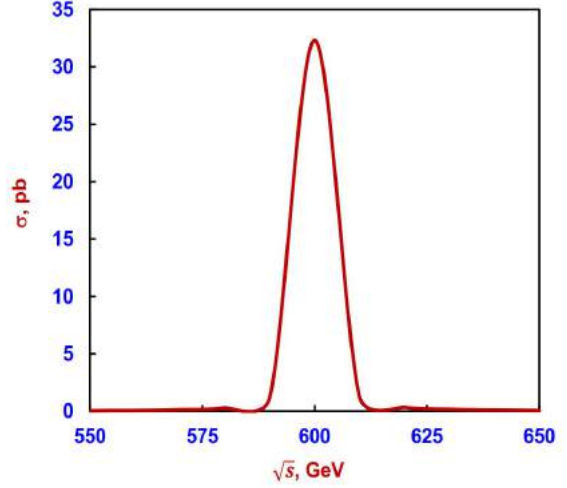


Fig. 6. Energy dependence of the reaction $\mu^- \mu^+ \rightarrow (H^*) \rightarrow \tilde{\chi}_1^- \tilde{\chi}_2^+$ cross section at $M_H = 600$ GeV, $\Gamma_H = 4$ GeV.

3. AMPLITUDE AND CROSS SECTION OF THE REACTION $\ell^- \ell^+ \rightarrow (\tilde{\nu}_L) \rightarrow \tilde{\chi}_i^- \tilde{\chi}_j^+$

Now we turn to the calculation of the diagram c) Fig. 1 with scalar neutrino $\tilde{\nu}_L$ exchange. The amplitude corresponding to this diagram can be written as

$$M_{i \rightarrow f} = ie^2 g_{\tilde{\chi}\ell\tilde{\nu}_L}^2 [\bar{u}_i(k_1, s) P_L u_\ell(p_1, s_1)] \cdot \frac{1}{(k_1 - p_1)^2 - m_{\tilde{\nu}_L}^2} [\bar{v}_\ell(p_2, s_2) P_L v_j(k_2, s')], \quad (21)$$

where $g_{\tilde{\chi}\ell\tilde{\nu}_L}^2 = G^2 = \frac{(V_{i\ell})^2}{x_W^2}$ – is the constant of interaction of the chargino with the lepton and the sneutrino [6];

$\frac{1}{(k_1 - p_1)^2 - m_{\tilde{\nu}_L}^2}$ – scalar neutrino propagator.

We define the square of the modulus of the matrix element (21) in the standard way:

$$|M_{i \rightarrow f}|^2 = \frac{e^4 G^4}{[(k_1 - p_1)^2 - m_{\tilde{\nu}_L}^2]} \cdot \frac{1}{4} [(p_1 \cdot k_1) - m_\ell m_{\tilde{\chi}_i} (s \cdot s_1) - m_\ell (s_1 \cdot k_1) + m_{\tilde{\chi}_i} (s \cdot p_1)] \times \\ \times [(p_2 \cdot k_2) - m_\ell m_{\tilde{\chi}_j} (s_2 \cdot s') - m_\ell (s_2 \cdot k_2) + m_{\tilde{\chi}_j} (p_2 \cdot s')]. \quad (22)$$

Using (22), for the cross section of the process under consideration in the case of longitudinally polarized lepton-antilepton pairs, we find the following expression:

$$\frac{d\sigma}{d(\cos\theta)} = \frac{\pi\alpha^2 G^4 s}{32[(k_1 - p_1)^2 - m_{\tilde{\nu}_L}^2]^2} \sqrt{\lambda(r_{\chi_i}, r_{\chi_j})} \cdot (1 - \lambda_1)(1 - \lambda_2) \times \\ \times [1 + r_{\tilde{\chi}_i} - r_{\tilde{\chi}_j} - \sqrt{\lambda(r_{\chi_i}, r_{\chi_j})} \cos\theta][1 - r_{\chi_i} + r_{\chi_j} - \sqrt{\lambda(r_{\chi_i}, r_{\chi_j})} \cos\theta], \quad (23)$$

here (the lepton mass is neglected in comparison with the energy \sqrt{s})

$$(k_1 - p_1)^2 = \frac{s}{2} [r_{\chi_i} + r_{\chi_j} - 1 + \sqrt{\lambda(r_{\chi_i}, r_{\chi_j})} \cos\theta].$$

As seen from the differential effective cross section (23), the lepton and antilepton should have left-handed helicities $\lambda_1 = \lambda_2 = -1$. At $\lambda_1 = +1$ or $\lambda_2 = +1$, the process is prohibited by the law of conservation of the total moment at the vertex $\ell^- \rightarrow \tilde{\nu}_\ell + \tilde{\chi}_i^-$ ($\ell^+ \rightarrow \tilde{\nu}_\ell + \tilde{\chi}_j^+$). This means that there is no interference between diagrams a) and c) at $\lambda_1 = \lambda_2 = -1$.

Now we assume that the lepton-antilepton pair is unpolarized and the chargino $\tilde{\chi}_i^-$ is longitudinally polarized. In this case, the differential cross section of the process under consideration is determined by the following expression:

$$\frac{d\sigma}{d(\cos\theta)} = \frac{1}{2} \frac{d\sigma_0}{d(\cos\theta)} (1 + h_1 P_\parallel), \quad (24)$$

where

$$\frac{d\sigma_0}{d(\cos\theta)} = \frac{\pi\alpha^2 G^4 s}{32[(k_1 - p_1)^2 - m_{\tilde{\nu}_L}^2]^2} \sqrt{\lambda(r_{\chi_i}, r_{\chi_j})} \cdot [1 + r_{\chi_i} - r_{\chi_j} - \sqrt{\lambda(r_{\chi_i}, r_{\chi_j})} \cos\theta] \times \\ \times [1 - r_{\chi_i} + r_{\chi_j} - \sqrt{\lambda(r_{\chi_i}, r_{\chi_j})} \cos\theta] \quad (25)$$

is the differential cross section of the reaction in the case of unpolarized particles, and P_\parallel – is the degree of longitudinal polarization of the chargino:

$$P_\parallel = \frac{\sqrt{\lambda(r_{\chi_i}, r_{\chi_j})} - (1 + r_{\chi_i} - r_{\chi_j}) \cos\theta}{1 + r_{\chi_i} - r_{\chi_j} - \sqrt{\lambda(r_{\chi_i}, r_{\chi_j})} \cos\theta}. \quad (26)$$

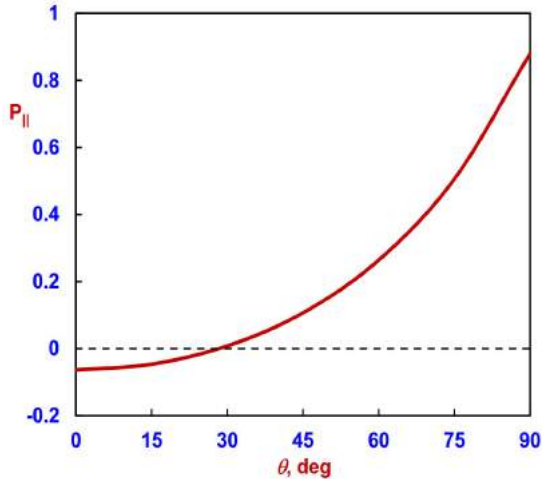


Fig. 7. Angular dependence of the P_\parallel on the angle θ .

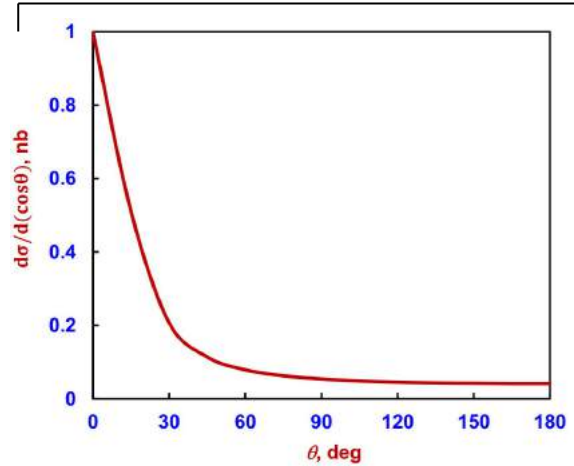


Fig. 8. Angular dependence of the cross section in the reaction $e^- e^+ \rightarrow (\tilde{\nu}_L^*) \rightarrow \tilde{\chi}_1^- \tilde{\chi}_2^+$.

In Fig. 7 shows the dependence of the degree of longitudinal polarization of the chargino on the angle θ at energy $\sqrt{s} = 500$ GeV, $M_2 = 150$ GeV, $\mu = 200$ GeV, $M_W = 80.385$ GeV. At the beginning of the angular spectrum ($0^\circ \leq \theta \leq 90^\circ$), the degree of longitudinal polarization is negative and with an increase in the emission angle θ it increases.

The dependence of the effective cross section on

the angle θ is illustrated in Fig. 8 at $\sqrt{s}=500$ GeV, $x_W=0.2315$, $M_2=150$ GeV, $\mu=200$ GeV, $m_{\tilde{\nu}_L}=40$ GeV. As follows from the figure, with an increase in the angle θ , the effective cross section at the beginning of the angular spectrum ($0^\circ \leq \theta \leq 90^\circ$) decreases, and at $\theta > 90^\circ$ it no changes.

CONCLUSION

We discussed the creation of a chargino pair in the annihilation of an arbitrarily polarized lepton-antilepton pair $\ell^- + \ell^+ \rightarrow \tilde{\chi}_i^- + \tilde{\chi}_j^+$. The contribution to

the cross section of the diagram with the exchange of the Higgs bosons H , h and A , as well as the scalar neutrino $\tilde{\nu}_L$ is studied in detail.

The longitudinal and transverse spin asymmetries caused by the polarizations of the lepton-antilepton pair, as well as the degrees of the longitudinal and transverse polarization of the chargino, have been determined. The angular and energy dependences of these characteristics, as well as the cross section of the considered reaction, are investigated in detail. The calculation results are illustrated with graphs.

-
- [1] ATLAS Collaboration. Observation of a new particle in the search for the Standard Model Higgs boson with the ATLAS detector of the LHC Phys. Letters, 2012, B 716, p. 1-29.
 - [2] CMS Collaboration. Observation of a new boson at mass of 125 GeV with the CMS experiment at the LHC Phys. Letters, 2012, B 716, p. 30-60.
 - [3] V.A. Rubakov. On Large Hadron Colliders discovery of a new particle with Higgs Boson properties UFN, 2012, V.182, No 10, p.1017-1025 (in Russian).
 - [4] A.V. Lanev. CMS Collaboration results: Higgs boson and search for new physics UFN, 2014, V. 184, No 9, p. 996-1004 (In Russian).
 - [5] D.I. Kazakov. The Higgs boson is found: what is next? UFN, 2014, V. 184, No 9, p. 1004-1017 (In Russian).
 - [6] A. Djouadi. The Anatomy of Electro-Weak Symmetry Breaking. Tome II: The Higgs boson in the Minimal Supersymmetric Standard Model. arXiv: hep-ph/0503172v2, 2003; DOI: 10.1016/j.physrep.2007.10.004.
 - [7] M. Spira. QCD effects in Higgs Physics. arXiv: hep-ph / 9705337v2, 1997.
 - [8] J.F. Gunion, H.E. Haber. Higgs bosons in Supersymmetric Phys. Rev., 2003, D 67, p. 0750.19.
 - [9] H.E. Haber, G. Kane. The search for supersymmetry: Probing physics beyond the Standard Model Phys. Rep., 1985, C 117, No 2-4, p. 75-263.
 - [10] D.I. Kazakov. Beyond the Standart Model (in search of Supersymmetry). arXiv: hep-ph/0012288.2000, 80p.
 - [11] V.D. Shiltsev. High energy particle colliders: past 20 years, next 20 years and beyond UFN, 2012, V. 182, No 10, p. 1033-1046 (in Russian).
 - [12] K. Peters. Prospects for beyond Standard Model Higgs boson searches at future LHC runs and other machines. arXive: 1701.05124v2 [hep-ex], 2007, 8p.
 - [13] S.K. Abdullayev, M.Sh. Gojayev, A.K. Gulayeva. The production of a chargino pair in polarized lepton-antilepton collisions (I) AJP, Fizika, 2020, V. XXVI, No 3, p. 20-30.
 - [14] A. Bartl, H. Fraas, W. Majerotto. Signatures of chargino production in e^+e^- -collisions. Z. Phys., 1986, B 30, p. 441-449.
 - [15] A. Bartl, H. Fraas, W. Majerotto. Production and decay of neutralinos in e^+e^- -collisions. J. Nucl. Phys., 1986, B 278, p. 1-25
 - [16] A. Djouadi, J. Kalinowski, P. Ohmann, P.M. Zerwas. Heavy SUSY Higgs bosons at e^-e^+ linear colliders. Z. Phys., 1997, C 74, p. 93-111.

Received:17.11.2020

PHASE TRANSITION AT THERMAL TREATMENT OF $\text{TlIn}_{1-x}\text{Sn}_x\text{Se}_2$ AMORPHOUS FILMS

M.M. PANAKHOV¹, E.Sh.ALEKPEROV¹, E.S. GARAYEV¹, S.A. SADRADDINOV¹,
A.M. NAZAROV², S.S. FARZALIYEV²

¹*Baku State University, AZ1148, Z. Khalilov str., 23, Baku, Azerbaijan*

²*Institute of Physics of ANAS, AZ1143, H.Javid ave., 131, Baku, Azerbaijan*

alekperoveldar@mail.ru

The crystallization process of TlInSe_2 amorphous films doped by tin impurity is investigated by method of high-energy electron diffraction. It is shown that crystallization of amorphous films by width 30nm obtained in high vacuum by thermal method takes place by regularities established by Abraham-Kolmogorov and it is described by analytical expression $V_t = V_0[1 - \exp(-kt^m)]$. The influence of tin impurity on values of nucleation activation energies and their further growth is defined by kinematic electron diffraction pattern of $\text{TlIn}_{1-x}\text{Sn}_x\text{Se}_2$ films.

Keywords: electrography, doping, structure, amorphous phase, kinetics, crystallization.

PACS: 61.66.Fn

INTRODUCTION

The investigation of structural characteristics of nanothickness semiconductor films of $A^{\text{III}}B^{\text{III}}C$ type with different impurities and solid solutions on their base becomes more actual one day by day. The compounds including in the given group, belong to the wide-band-gap semiconductors in which the forbidden band width can be gradually changed. Their structure can be modified by change of technological process of film obtaining and also by doping [1 – 4]. These complex semiconductor compounds are anisotropic ones and they are of interest for modern optoelectronics [5 -8].

TlInSe_2 compound is the one of the representatives of incomplete valence semiconductor compounds with chain structure having the specific structure of crystal lattice. The crystallization kinetic parameters of TlInSe_2 nano-dimensional films are investigated and established in [9]. The experimental data on atom interactions in solid substances, valence electrons in atoms can be obtained by methods of electron diffraction [10, 11] from which the electron diffraction method is the more suitable for the investigations in the given direction. Using this method the influence of Sn chemical element doping on phase transition kinetics of TlInSe_2 amorphous films crystallizing in structure with tetragonal volume-centered lattice corresponding to symmetry group D_{4h}^{18} -I4/mcm were investigated [12]. The experiments on semiconductor study doped by impurities can be divided on two groups. The works in which the band structure change is studied caused mainly by distortion of semiconductor crystal lattice, belong to the first group. The investigation of state density tail spreading deep into the forbidden band belong to the second group.

The study difficulty of these questions is in the fact that the film growth mechanism is often unknown. The investigation of temperature-time dependence of film crystallization promotes the explanation of their growth mechanism.

EXPERIMENTAL PART

The investigated thin films are obtained by different methods the one of which is the thermal evaporation in vacuum installation. In the given work $\text{TlIn}_{1-x}\text{Sn}_x\text{Se}_2$ ($x=0.02\div 0.09$) amorphous films of width ~30 nm are obtained in vacuum 3×10^{-5} Pa in installation BYII-5 by thermal method and simultaneous deposition of TlInSe_2 and Sn from two molybdenum furnaces on the substrate consisting of fresh cleavages of KCl, NaCl and KJ being lower than 403K and previously covered by carbonic film. The deposition time is 5-10 sec. The value of substance separation coefficient is taken under consideration for obtaining of films with impurity uniform distribution. The carbonic film by width 2-3 nm is marked again on obtained films for prevention of evaporation of easily volatile component and oxidation processes in the result of further thermal treatment of films. Dissolving the substrate, the investigated film is transferred on tungsten furnace-substrate where it is subjected by thermal treatment.

The distribution of condensate composition on coordinates on condensation plane is defined with the help of known formula in crystallography [10]:

$$q = \frac{Q}{4\pi h^2} \frac{1}{(1 + \alpha)^{3/2}} \quad (1).$$

Here q is amount of substance per unit of substrate surface plane, Q is amount of evaporated substance, h is distance from evaporation source to any point on condensate plane, coefficient $\alpha = x/h$, where x is distance from the point being directly under evaporator to any point on substrate plane. The film thickness obtained by vacuum evaporation is calculated by following formula:

$$H = \frac{q}{\rho} \quad (2),$$

where ρ is substance density. Besides, the film thickness is controlled by spectrometer «Spekor-250»,

and film composition is controlled by atomic-adsorption spectrophotometer «ShimadzuAA-6300».

The crystallization kinetics of $TlIn_{1-x}Sn_xSe_2$ amorphous films is investigated on electron diffractometer of ЭМР-102 type using the energy filter for separation of inelastically scattered electrons and electric registration of diffraction line intensity appearing as a result of amorphous phase crystallization. The size of intensity electronic pickup slot at electric registration of chosen line intensity of crystal phase is defined from ratio $2/3d=l$, where d is slot width, l is half-width of registered line. The recording maximum level of chosen line intensity can be achieved by regulation of signal amplification. The investigated film is heated at constant temperature in region of phase transformation, i.e. crystallization on this recording level. The crystallization temperature of $TlIn_{1-x}Sn_xSe_2$ amorphous films is 420 – 480K. The thermal treatment of amorphous films at the given temperature leads to the fact that phase transformation begins. The investigated film being in the original carbonic capsule, is totally defend from oxidation and evaporation at transfer in electron diffractometer and further thermal treatment. The high quality of electron diffraction patterns obtained from the films deposited on KCl is observed. But not all obtained samples are seemed applicable for the investigation as substrate roughness on atomic level and stress on interface film-substrate influence the destructive action on the films during their separation from the substrates that is confirmed in [13].

The kinematic electron diffraction patterns in which the isothermal phase transformation is observed, i.e. the changes of the quantity and intensities of increasing crystal phase lines corresponding to different time moments are observed, are obtained at temperatures 420, 450 and 480K.

RESULTS AND THEIR DISCUSSION

$TlIn_{0.93}Sn_{0.07}Se_2$ films are chosen from obtained $TlIn_{1-x}Sn_xSe_2$ ($x=0.02\pm 0.09$) films by the way of change of phase composition. Three diffraction lines: $S=4\pi\sin\theta/\lambda = 0.212; 0.349; 0.519 \text{ nm}^{-1}$ are observed in the beginning on kinematic electron diffraction pattern obtained at 450K (Fig.1) showing the process phase transformation.



Fig. 1. Kinematic electron diffraction pattern showing $TlIn_{0.93}Sn_{0.07}Se_2$ crystallization at temperature 450K.

The threshold temperature at which the instantaneous crystallization of amorphous film not allowing us to observe the whole dynamics of phase transformation process takes place, is 483K. The diffraction lines from polycrystal on kinematic electron diffraction pattern are indicated on the base of parameters of tetragonal cell $TlInSe_2$ with values $a=b=0.8075, c=0.6847 \text{ nm}$ [12].

The measurements of intensity, reflex radius and others are carried out for interpretation of electron diffraction pattern. As it is known [10], I_{hkl} line intensity is connected with irradiated volume of crystalline substance by following expression:

$$I_{hkl} = I_o \lambda \left| \frac{\Phi_{hkl}}{\Omega} \right|^2 V \frac{d_{hkl}^2 \Delta}{4\pi L \lambda} P \quad (3).$$

where I_o is intensity of primary beam radiation, λ is electron wavelength, Φ is structural amplitude of diffraction reflection which is calculated from atomic scattering factors in kinematic approximation, Ω is volume of elementary cell, V is irradiated volume of polycrystal preparation. Parameters d_{hkl} and Δ show the interplanar spacing and small region of Debye ring correspondingly, P is multiplicity factor of diffraction reflex amplification, $L\lambda$ is device constant which is defined in the dependence on applied voltage accelerating electrons.

The measurements of diffraction lines on electron diffraction pattern show that process of amorphous film crystallization takes place regularly, i.e. $I_{hkl} \sim V$. The widths and intensities of lines from different regions of kinematic electron diffraction pattern is defined by microphotometer MF-4 (Fig.2).

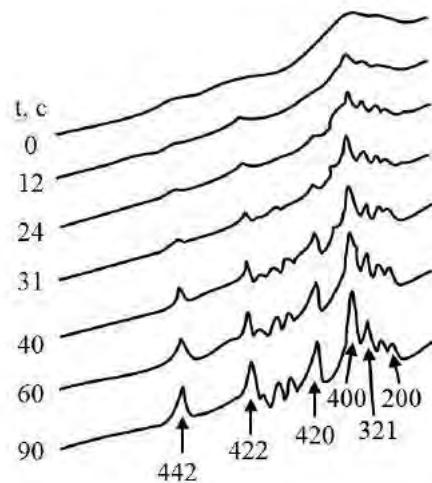


Fig.2. Microphotograms from different regions of kinematic electron diffraction pattern taken at 450K.

The temperature-time dependences of crystallization are formed with taking under consideration the intensities of diffraction lines of increasing crystal phase corresponding to different annealing moments (Fig.3).

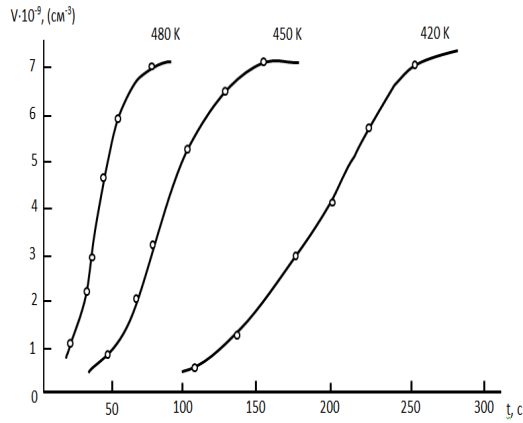


Fig.3. Kinematic curves of crystallization of amorphous TlIn_{0.93}Sn_{0.07}Se₂.

The obtained isotherms are compared with analytical expression (4) for kinetic curves of phase transformation:

$$V_t = V_0[1 - \exp(-kt^m)] \quad (4)$$

where V_t is crystallized volume in the given time moment t ; V_0 is amorphous phase volume in the process beginning; $k=1/3\pi\omega c^3$ is reaction rate constant; ω is the rate of germ-formation of new phase in unit of non-transformed volume; c is crystal linear rate of growth; m is parameter characterizing the crystal growth dimension which is seemed equal approximately to 3 ($m \sim 3$) in considered case. This confirms the two-dimensional growth of forming germs. The dependence graph $\ln \ln V_0/V_0 - V_t$ on $\ln t$ for 420, 450 and 480K temperatures (Fig.4) which is described by analytic expression (4) is constructed on the base of electric registration on reflex intensities of diffraction pattern (t, I, V_t).

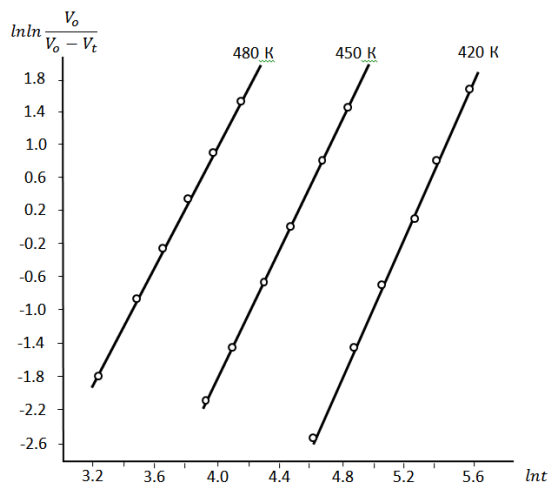


Fig.4. Dependence of $\ln \ln V_0/V_0 - V_t$ on $\ln t$ for crystallization of amorphous TlIn_{0.93}Sn_{0.07}Se₂.

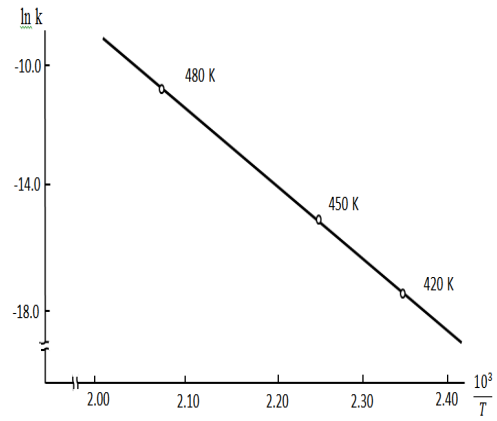


Fig.5. Dependence of $\ln k$ on reversal temperature for crystallization of amorphous TlIn_{0.93}Sn_{0.07}Se₂.

The value of total activation energy of crystallization process is equal to $E_{tot} = 48.85$ kcal/mol and it is defined by inclination of $\ln k$ dependence on inverse temperature $10^3/T$ (Fig.5). The values of germ-formation activation energy E_g and activation energy of their further growth E_{gr} which are given in table are also defined.

Table

Compounds	m	Activation energy		
		E_{tot} (kcal/mol)	E_{gr} (kcal/mol)	E_g (kcal/mol)
TlInSe ₂	3	45.74	14.71	16.32
TlIn _{1-x} Sn _x Se ₂	3	48.85	15.69	17.47

CONCLUSION

The investigation results by electron diffraction methods of crystallization kinetics of TlIn_{0.93}Sn_{0.07}Se₂ thin amorphous films are presented in the given paper. It is confirmed that for these compounds the effective crystallization activation energy increases on 6,8%, i.e. crystallization of amorphous films with impurity takes place at more high temperatures than without impurity. The increase of temperature interval of amorphous film crystallization up to 60°C is observed. It is established that in phase transition process in the investigated temperature interval the two-dimensional crystal growth takes place. The lattice parameters of elementary cells increase correspondingly to syngonies in the given composition (at $x=0.07$) on 3.5% in crystalline films obtained after phase transition. The change of lattice parameters in the dependence on composition is non-linear one. The increase of activation energy and lattice parameters at doping of TlInSe₂ with Sn impurity at unchangeable space symmetry group with taking under consideration of tin physical properties can be considered as regular one.

PHASE TRANSITION AT TERMAL TREATMENT OF $TlIn_{1-x}Sn_xSe_2$ AMORPHOUS FILMS

- [1] V. Kovanda, Vicek Mir, H. Jain. J. Non-Cryst. Solids. 2003. vol.326. p.88.
- [2] A.M. Pashayev, T.D. Jafarov. Nanoelectronics physical basements. Baku, 2014. p.88 .
- [3] T.S. Kavetsky, O.I. Shpotyuk, V.T. Boyko. J. Phys. and Chem. Of solids. 2007.vol.68. p.712.
- [4] A.M. Filachev, I.I. Taubkin, M.A. Trishenkov. Solid-state photoelectronics. M., 2012. p.363.
- [5] J.S. Sanghera, I.D. Aggarwal, L.B. Shaw,
- [6] C.M. Florea et. al. J. Optoelectronics and Advancedmaterials. 2006. vol. 8. p.2148.
- [7] Ah.U. Malsagov. Reference review on semiconductor compounds of $A^I B^{III} C_2^{IV}$, $TlB^{III} C_2^{VI}$ type. Nalchik:El-Fa, 2007. p.692.
- [8] V. Kovanda, Vicek Mir, H. Jain. J. Non-Cryst. Solids. 2003. vol. 326.pP.88.
- [9] R.M. Sardarli, O.A. Samedov, A.P. Abdullayev, F.T. Salmanov and others //FTP, 2011. vol.45. B. 11. p. 1441
- [10] F.I. Aliyev, D.I. Ismayilov, E.Sh. Alekperov. Proceedings of Academy of Sciences of Azerbaijan. 1989. №11-12, vol.45, pp.27-29.
- [11] A.S. Avilov. Precision electron diffraction. Doctoral thesis on phys-math sciences: 01.04.18. Moscow,1999. p. 274.
- [12] D.I. Ismailov, M.F. Aliyeva, E.Sh. Alekperov,
- [13] F.I. Aliyev. Semiconductors. 2003, vol.37, №7, p.744.
- [14] D. Muller, G. Eulenberger H. Hahn, Z. Anorg. Allg. Chem., 398, 207 (1973).
- [15] F.F. Volkenstein. Electron processes on the surface of semiconductors at chemisorption. M.: Science, 1987, p.43.

Received:12.11.2020

LONGITUDINAL SPIN ASYMMETRIES IN SEMI-INCLUSIVE DEEP-INELASTIC SCATTERING OF POLARIZED LEPTONS BY POLARIZED NUCLEONS

S.K. ABDULLAYEV, M.Sh. GOJAYEV

*Baku State University, Azerbaijan, AZ 1148, Baku, acad. Z. Khalilov, 23,
m_qocayev@mail.ru*

Within the framework of the Standard Model, the processes of semi-inclusive deep inelastic scattering of longitudinally polarized leptons (antileptons) by polarized nucleons are considered: $\ell^-(\ell^+)N \rightarrow \ell^-(\ell^+)h^\pm X$, here $\ell^-(\ell^+)$ – an electron or muon (positron or antimuon), h^\pm – charged π^\pm - or K^\pm -meson, X – a system of undetected hadrons. By introducing non-polarization and polarization structure functions of hadrons and taking into account the longitudinal polarizations of the lepton and target nucleon, analytical expressions are obtained for the differential cross sections of the processes. All structure functions of hadrons are found in the quark-parton model; they depend on the distribution and fragmentation functions of quarks and antiquarks. The longitudinal spin asymmetries $A_N^{h^+h^-}$, $A_N^{h^+}$, $A_N^{h^-}$ and others are determined, the dependence of the asymmetries on the invariant variables x , y and z is studied. The longitudinal spin asymmetry $A_q^{\pi^+\pi^-}$ is compared with the experimental data of the COMPASS collaboration.

Keywords: Semi-inclusive deep inelastic scattering, structure functions, longitudinal spin asymmetries, spiral amplitudes, distribution functions, fragmentation functions.

PACS: 12.15.-Y, 13.60.-R, 13.85.NI, 13.87.FH

1. INTRODUCTION

The study of the quark structure of nucleons is one of the main tasks of modern high-energy physics. In this direction, the processes of deep inelastic scattering (DIS) of longitudinally polarized leptons (muons, electrons) by polarized nucleons are intensively investigated in various laboratories around the world (COMPASS, EIC, EMC, DEZY, HERMES) [1-8]. In the first experiments, the polarization structure functions (SF) of the proton $F_2^p(x)$ and neutron $F_2^n(x)$ were measured in a wide range of variation of the Bjorken variable x and it was established that the integral

$$\int_0^1 \frac{dx}{x} [F_2^p(x) - F_2^n(x)] = 0.235 \pm 0.0026.$$

However, this result contradicts the Gottfried sum rules, according to which this integral is equal to 1/3. The experimental results show that the distribution densities of sea u - and d -quarks in the proton $\bar{u}(x)$ and $\bar{d}(x)$ are different:

$$\int_0^1 dx [\bar{d}(x) - \bar{u}(x)] = 0.148 \pm 0.039 \neq 0.$$

Thus, in the DIS processes of unpolarized leptons in unpolarized nucleons $\ell^\mp + N \rightarrow \ell^\mp + X$, we determine the distribution of sea (\bar{q}) and valence ($q_v = q - \bar{q}$) quarks in a nucleon. The question arises, what new information does the investigation of the DIS of polarized leptons on polarized nucleons provide? Here it becomes possible to determine the density of distributions of polarized sea and valence quarks in polarized nucleons:

$$\Delta q(x, Q^2) = q^\uparrow(x, Q^2) - q^\downarrow(x, Q^2),$$

$$\Delta \bar{q}(x, Q^2) = \bar{q}^\uparrow(x, Q^2) - \bar{q}^\downarrow(x, Q^2),$$

$$\Delta q_v(x, Q^2) = \Delta q(x, Q^2) - \Delta \bar{q}(x, Q^2),$$

where q^\uparrow and q^\downarrow (\bar{q}^\uparrow and \bar{q}^\downarrow) is the distribution density of a quark (antiquark) whose spin is parallel and antiparallel to the nucleon spin. This arises a very interesting question: is the difference between the distributions of polarized sea \bar{u} - and \bar{d} -quarks $\Delta \bar{u}(x, Q^2) - \Delta \bar{d}(x, Q^2)$ equal to zero or is it different from zero? We can give a positive answer to this question by studying the processes of semi-inclusive deep inelastic scattering (SIDIS) of polarized leptons by polarized nucleons

$$\ell^-(\lambda) + N(h_N) \rightarrow \ell^-(\lambda) + h^\pm + X, \quad (1)$$

$$\ell^+(\lambda) + N(h_N) \rightarrow \ell^+(\lambda) + h^\pm + X, \quad (2)$$

where λ – is the helicity of the lepton (antilepton), h_N – is the longitudinal polarization of the target nucleon, $h^\pm(\pi^\pm, K^\pm)$ – is the recorded hadron in the final state together with the lepton at coincidence, X – is the system of nondetectable hadrons.

In [9, 10], the spin asymmetries in reactions (1) and (2) were studied within the framework of the quark-parton model (QPM). However, these works did not consider the non-polarization and polarization structure functions of hadrons. In this paper, within the framework of the Standard Model (SM), by introducing the SF of hadrons, analytical expressions are obtained for the differential cross sections of processes (1) and (2), a number of longitudinal spin asymmetries are determined, and the dependence of these asymmetries on invariant variables is studied in detail, x , y and z .

2. KINEMATIC VARIABLES OF REACTION

The SIDIS process of a lepton on a nucleon is described by the Feynman diagrams shown in Fig. 1.

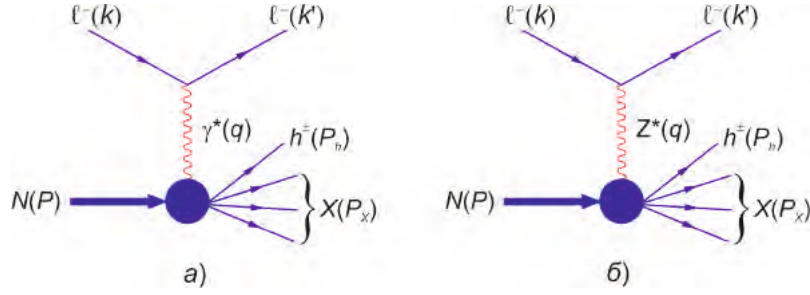


Fig. 1. Feynman diagrams of process $\ell^- N \rightarrow \ell^- h^\pm X$.

Here k and k' – are the 4-momenta of the incident and scattered leptons, P and P_h – are the 4-momenta of a nucleon and an inclusive hadron h^\pm , P_X – is the total 4-momentum of undetected hadrons X . The exchange between a lepton and a nucleon occurs by a virtual photon γ^* and a neutral Z^* -boson, these particles transfer a 4-momentum $q = k - k'$ from a lepton to a nucleon. A number of invariant variables are introduced to describe the SIDIS of a lepton on nucleons:

1) energy transfer from lepton to nucleon

$$\nu = \frac{(P \cdot q)}{M} = E - E', \quad (3)$$

where M – is the mass of the nucleon, $E(E')$ – is the energy of the initial (final) lepton;

2) square of transmitted momentum

$$Q^2 = -q^2 = -(k - k')^2 = 4EE' \sin^2 \frac{\theta}{2} - 2m_\ell^2,$$

where m_ℓ and θ – are the mass and scattering angle of the lepton; for the lepton mass $EE' \sin^2 \frac{\theta}{2} \gg m_\ell^2$

we can neglect and

$$Q^2 = 4EE' \sin^2 \frac{\theta}{2}; \quad (4)$$

3) ordinary Bjorken variables DIS

$$x = \frac{Q^2}{2M\nu}, \quad y = \frac{(P \cdot q)}{(P \cdot k)} = \frac{\nu}{E}, \quad (5)$$

which range from 0 to 1;

4) variable z that determines the fraction of the energy transferred to the nucleon carried away by the hadron h

$$z = \frac{(P \cdot P_h)}{(P \cdot q)} = \frac{E_h}{\nu}; \quad (6)$$

The shaded area in the diagrams shows that the nucleon has an internal structure, which is taken into account by introducing the SF.

5) the square of the total energy of the lepton-nucleon system in the center of mass system

$$s = (k + P)^2 = \frac{Q^2}{xy} + M^2 + m_\ell^2,$$

when $Q^2 \gg M^2$ we get

$$s = \frac{Q^2}{xy}. \quad (7)$$

Shown in Fig. 1, the process is called SIDIS of a lepton on a nucleon if $Q^2 \gg M^2$ and $\nu \gg M$. In this case, we can neglect the masses of the nucleon and lepton.

3. NON-POLARIZING AND POLARIZING SF

According to the SM, the Lagrangian of the interaction of an Z -boson with a fermion pair is:

$$L_{Zff} = -\frac{g}{2 \cos \theta_w} \gamma_\alpha [g_L(f)(1 + \gamma_5) + g_R(f)(1 - \gamma_5)] \cdot Z_\alpha$$

where $g_L(f)$ ($g_R(f)$) – is the left (right) constant of the interaction of the fermion with the Z -boson:

$$\begin{aligned} g_L(\ell) &= -\frac{1}{2} + x_w, & g_R(\ell) &= x_w, \\ g_L(u) &= \frac{1}{2} - \frac{2}{3} x_w, & g_R(u) &= -\frac{2}{3} x_w, \\ g_L(d) &= -\frac{1}{2} + \frac{1}{3} x_w, & g_R(d) &= \frac{1}{3} x_w, \end{aligned} \quad (8)$$

$x_w = \sin^2 \theta_w$ – Weinberg parameter (θ_w – Weinberg angle).

The amplitude corresponding to the diagrams in Fig. 1 is written as:

$$\begin{aligned} M_{i \rightarrow f} &= i \frac{e^2}{Q^2} \{ [\bar{u}(k') \gamma_\alpha u(k)] \langle P_X, P_h | J_\alpha^{(\gamma)} | P, S \rangle + \\ &+ G_{eff} \{ \bar{u}(k') \gamma_\alpha [g_L(\ell)(1 + \gamma_5) + g_R(\ell)(1 - \gamma_5)] u(k) \} \langle P_X, P_h | J_\alpha^{(Z)} | P, S \rangle, \end{aligned} \quad (9)$$

where

$$G_{eff} = -\frac{G_F M_Z^2}{2\sqrt{2}\pi\alpha} \cdot \frac{Q^2}{Q^2 + M_Z^2}, \quad (10)$$

M_Z – Z -boson mass, $J_\alpha^{(\gamma)}$ and $J_\alpha^{(Z)}$ – electromagnetic and weak neutral hadron currents, G_F – Fermi constant of weak interactions, S – 4-vector of target nucleon polarization.

The differential cross section of the SIDIS of polarized leptons on polarized nucleons with registration of the lepton and hadron h in the final state is expressed by the product of the lepton and hadron tensors:

$$\frac{d\sigma^{(-)}}{dx dy dz} = \frac{2\pi y \alpha^2}{Q^4} [L_{\mu\nu}^{(\gamma)} H_{\mu\nu}^{(\gamma)} + G_{eff} L_{\mu\nu}^{(I)} H_{\mu\nu}^{(I)} + G_{eff}^2 L_{\mu\nu}^{(Z)} H_{\mu\nu}^{(Z)}]. \quad (11)$$

Here $L_{\mu\nu}^{(\gamma)}$ and $H_{\mu\nu}^{(\gamma)}$ ($L_{\mu\nu}^{(Z)}$ and $H_{\mu\nu}^{(Z)}$) – are the tensors corresponding to the photon (Z -boson) exchange, $L_{\mu\nu}^{(I)}$ and $H_{\mu\nu}^{(I)}$ – are the interference of the photon and boson mechanisms. Lepton tensors $L_{\mu\nu}^{(\gamma)}$, $L_{\mu\nu}^{(Z)}$ and $L_{\mu\nu}^{(I)}$ are easily calculated based on the amplitude (9):

$$\begin{aligned} L_{\mu\nu}^{(\gamma)} &= 2[k_\mu k'_\nu + k'_\mu k_\nu - (k \cdot k') g_{\mu\nu} + i\lambda \varepsilon_{\mu\nu\rho\sigma} k_\rho k'_\sigma], \\ L_{\mu\nu}^{(I)} &= [g_L(\ell) + g_R(\ell) - \lambda(g_L(\ell) - g_R(\ell))] L_{\mu\nu}^{(\gamma)}, \\ L_{\mu\nu}^{(Z)} &= 2[g_L^2(\ell) + g_R^2(\ell) - \lambda(g_L^2(\ell) - g_R^2(\ell))] L_{\mu\nu}^{(\gamma)}, \end{aligned} \quad (12)$$

where $\lambda = +1$ (-1) – corresponds to the right (left) -polarized lepton.

The hadron tensor in $H_{\mu\nu}^{(i)}$ ($i = \gamma, I, Z$) the general case contains three non-polarization ($F_1^{(i)}, F_2^{(i)}, F_3^{(i)}$) and five polarization ($G_1^{(i)}, G_2^{(i)}, G_3^{(i)}, G_4^{(i)}, G_5^{(i)}$) hadron SF [11, 12]:

$$\begin{aligned} H_{\mu\nu}^{(i)} &= \left(-g_{\mu\nu} + \frac{q_\mu q_\nu}{q^2} \right) F_1^{(i)} + \frac{\tilde{P}_\mu \tilde{P}_\nu}{(P \cdot q)} F_2^{(i)} - i\varepsilon_{\mu\nu\alpha\beta} \frac{q_\alpha P_\beta}{2(P \cdot q)} F_3^{(i)} + \\ &+ i\varepsilon_{\mu\nu\alpha\beta} \frac{q_\alpha}{(P \cdot q)} \left[S_\beta G_1^{(i)} + \left(S_\beta - \frac{(S \cdot q)}{(P \cdot q)} P_\beta \right) G_2^{(i)} \right] + \frac{1}{(P \cdot q)} \left[\frac{1}{2} (\tilde{P}_\mu \tilde{S}_\nu + \tilde{S}_\mu \tilde{P}_\nu) - \frac{(S \cdot q)}{(P \cdot q)} \tilde{P}_\mu \tilde{P}_\nu \right] G_3^{(i)} + \\ &+ \frac{(S \cdot q)}{(P \cdot q)} \left[\frac{\tilde{P}_\mu \tilde{P}_\nu}{(P \cdot q)} G_4^{(i)} + \left(-g_{\mu\nu} + \frac{q_\mu q_\nu}{q^2} \right) G_5^{(i)} \right]. \end{aligned} \quad (13)$$

Here

$$\tilde{P}_\mu = P_\mu - \frac{(P \cdot q)}{q^2} q_\mu, \quad \tilde{S}_\mu = S_\mu - \frac{(S \cdot q)}{q^2} q_\mu,$$

all structure functions depend on three invariant variables x, z, Q^2 :

$$F_n = F_n(x, z, Q^2) \quad (n=1,2,3); \quad G_m = G_m(x, z, Q^2) \quad (m=1 \div 5).$$

The differential cross section of the SIDIS of polarized leptons on unpolarized nucleons depends on the SF $F_1^{(i)}, F_2^{(i)}, F_3^{(i)}$:

$$\frac{d\sigma^{(-)}(\lambda)}{dx dy dz} = \frac{4\pi\alpha^2}{xyQ^2} \eta_i \left[xy^2 F_1^{(i)} + \left(1 - y - x^2 y^2 \frac{M^2}{Q^2} \right) F_2^{(i)} \pm xy \left(1 - \frac{y}{2} \right) F_3^{(i)} \right], \quad (14)$$

$i = \gamma, Z$ and γZ correspond to the exchange of a photon, Z -boson and their interference, the factor η_i is determined as follows:

$$\eta_\gamma = 1, \quad \eta_{\gamma Z} = -G_{eff}, \quad \eta_Z = G_{eff}^2,$$

lepton (antilepton) scattering corresponds to the upper (lower) sign.

SF for the processes of DIS leptons (antileptons) are equal:

$$\begin{aligned} F_{1,2}^{(i)} &= F_{1,2}^\gamma + [\pm \lambda g_A(\ell) - g_V(\ell)] F_{1,2}^{\gamma Z} + [g_V^2(\ell) + g_A^2(\ell) \mp 2\lambda g_V(\ell) g_A(\ell)] F_{1,2}^Z, \\ F_3^{(i)} &= [\pm \lambda g_V(\ell) - g_A(\ell)] F_3^{\gamma Z} + [2g_V(\ell) g_A(\ell) \mp \lambda [g_V^2(\ell) + g_A^2(\ell)]] F_3^Z. \end{aligned} \quad (15)$$

Here $g_V(\ell) = g_L(\ell) + g_R(\ell)$ and $g_A(\ell) = g_L(\ell) - g_R(\ell)$ – vector and axial constants of interaction of a lepton with a Z -boson.

The addition of polarized leptons (antileptons) by a polarized target to the differential cross section of the

SIDIS is proportional to the polarization of the nucleon h_N and depends on the polarization SF $G_1^{(i)} - G_5^{(i)}$:

$$\frac{d\sigma^{(-)}(\lambda; h_N)}{dx dy dz} = \frac{4\pi\alpha^2}{xyQ^2} \eta_i h_N \left\{ \lambda xy \left(2 - y - 2x^2 y^2 \frac{M^2}{Q^2} \right) G_1^{(i)} - 4\lambda x^3 y^2 \frac{M^2}{Q^2} G_2^{(i)} - 2x^2 y \frac{M^2}{Q^2} \times \right. \\ \left. \times \left(1 - y - x^2 y^2 \frac{M^2}{Q^2} \right) G_3^{(i)} + \left(1 + 2x^2 y \frac{M^2}{Q^2} \right) \left[\left(1 - y - x^2 y^2 \frac{M^2}{Q^2} \right) G_4^{(i)} + xy^2 G_5^{(i)} \right] \right\}. \quad (16)$$

It follows from this expression that the contributions to the cross section of polarization SF $G_2^{(i)}$ and $G_3^{(i)}$ are proportional to the ratio M^2/Q^2 , and therefore are suppressed, since in the DIS region $Q^2 \gg M^2$.

In the deep inelastic region of lepton-nucleon scattering for differential cross sections of processes $\ell^\mp + N \rightarrow \ell^\mp + h + X$, we obtain the expressions (it is taken into account that $M^2/Q^2 \rightarrow 0$):

$$\frac{d\sigma^{(\mp)}(\lambda; h_N)}{dx dy dz} = \frac{4\pi\alpha^2}{xyQ^2} \eta_i \left\{ [1 + (1-y)^2] x F_1^{(i)} \pm \frac{1}{2} [1 - (1-y)^2] x F_3^{(i)} + (1-y) F_L^{(i)} - \right. \\ \left. - h_N [[1 + (1-y)^2] x G_5^{(i)} \mp \lambda [1 - (1-y)^2] x G_1^{(i)} + 2(1-y) G_L^{(i)}] \right\}, \quad (17)$$

here we have introduced longitudinal SF by means of the relations

$$F_L^{(i)} = F_2^{(i)} - 2x F_1^{(i)}, \quad G_L^{(i)} = G_4^{(i)} - 2x G_5^{(i)}. \quad (18)$$

Polarizing SF are determined by the expressions:

$$G_1^{(i)} = \mp \lambda G_1^\gamma - [g_A(\ell) \mp \lambda g_V(\ell)] \cdot G_1^{\gamma Z} + [2g_V(\ell) g_A(\ell) \mp \lambda (g_V^2(\ell) + g_A^2(\ell))] G_1^Z, \\ G_4^{(i)} = 2x G_5^{(i)} = 2x \{ -[g_V(\ell) \mp g_A(\ell)] \cdot G_5^{\gamma Z} + [g_V^2(\ell) + g_A^2(\ell) \mp 2\lambda g_V(\ell) g_A(\ell)] G_5^Z \}. \quad (19)$$

4. SF IN THE QUARK-PATRON MODEL

Let's calculate the SF of hadrons in the QPM. The electromagnetic and weak neutral quark currents are determined by the formulas

$$J_\mu^{(\gamma)} = \sum_q Q_q (\bar{q} \gamma_\mu q), \\ J_\mu^{(Z)} = \sum_q \bar{q} \gamma_\mu [g_V(q) + \gamma_5 g_A(q)] q, \quad (20)$$

Q_q – where is the quark charge.

On the basis of these currents, the following expressions were obtained in the QPM for the SF of hadrons (the contribution of valence quarks and sea quark-antiquark pairs is taken into account):

$$F_1^\gamma = \frac{1}{2} \sum_q Q_q^2 [q(x) D_q^h(z) + \bar{q}(x) D_{\bar{q}}^h(z)], \\ F_2^\gamma = x \sum_q Q_q^2 [q(x) D_q^h(z) + \bar{q}(x) D_{\bar{q}}^h(z)], \\ F_3^\gamma = 0, \\ F_1^{\gamma Z} = \sum_q Q_q g_V(q) [q(x) D_q^h(z) + \bar{q}(x) D_{\bar{q}}^h(z)], \\ F_2^{\gamma Z} = x \sum_q 2Q_q g_V(q) [q(x) D_q^h(z) + \bar{q}(x) D_{\bar{q}}^h(z)], \\ F_3^{\gamma Z} = \sum_q 2Q_q g_A(q) [q(x) D_q^h(z) - \bar{q}(x) D_{\bar{q}}^h(z)], \quad (21)$$

$$F_1^Z = \frac{1}{2} \sum_q [g_V^2(q) + g_A^2(q)] [q(x) D_q^h(z) + \bar{q}(x) D_{\bar{q}}^h(z)], \\ F_2^Z = x \sum_q [g_V^2(q) + g_A^2(q)] [q(x) D_q^h(z) + \bar{q}(x) D_{\bar{q}}^h(z)], \\ F_3^Z = \sum_q 2g_V(q) g_A(q) [q(x) D_q^h(z) - \bar{q}(x) D_{\bar{q}}^h(z)], \\ G_1^\gamma = \frac{1}{2} \sum_q Q_q^2 [\Delta q(x) D_q^h(z) + \Delta \bar{q}(x) D_{\bar{q}}^h(z)],$$

$$\begin{aligned}
 G_4^\gamma &= G_5^\gamma = 0, \\
 G_1^{\gamma Z} &= \sum_q Q_q g_V(q) [\Delta q(x) D_q^h(z) + \Delta \bar{q}(x) D_{\bar{q}}^h(z)], \\
 G_4^{\gamma Z} &= x \sum_q 2Q_q g_A(q) [\Delta q(x) D_q^h(z) - \Delta \bar{q}(x) D_{\bar{q}}^h(z)], \\
 G_5^{\gamma Z} &= \sum_q Q_q g_A(q) [\Delta q(x) D_q^h(z) - \Delta \bar{q}(x) D_{\bar{q}}^h(z)], \\
 G_1^Z &= \frac{1}{2} \sum_q [g_V^2(q) + g_A^2(q)] [\Delta q(x) D_q^h(z) + \Delta \bar{q}(x) D_{\bar{q}}^h(z)], \\
 G_4^Z &= x \sum_q 2g_V(q) g_A(q) [\Delta q(x) D_q^h(z) - \Delta \bar{q}(x) D_{\bar{q}}^h(z)], \\
 G_5^Z &= \sum_q g_V(q) g_A(q) [\Delta q(x) D_q^h(z) - \Delta \bar{q}(x) D_{\bar{q}}^h(z)].
 \end{aligned}$$

Here $q(x)$ ($\bar{q}(x)$) – are the variable distributions of the number x of quarks (antiquarks) in a nucleon, $\Delta q(x) = q^\uparrow(x) - q^\downarrow(x)$ ($\Delta \bar{q}(x) = \bar{q}^\uparrow(x) - \bar{q}^\downarrow(x)$) – is the difference between the distributions of a quark (antiquark) whose spin is parallel and antiparallel to the spin of a nucleon, $D_q^h(z)$ ($D_{\bar{q}}^h(z)$) – is the function of fragmentation of a q quark (\bar{q} antiquark) into a hadron h . Summation over q propagates over all quarks and antiquarks, which are present in a nucleon at a given value of the variable x .

As can be seen from expressions (21), in the QPM, the SF of deep inelastic scattering of leptons by nucleons depend on the scaling variables x and z , and satisfy the relations

$$F_2^i = 2xF_1^i, \quad G_4^i = 2xG_5^i,$$

which leads to the vanishing of the longitudinal SF: $F_L^i = 0$, $G_L^i = 0$. The reason for this is the lack of interaction between quarks. In reality, however, quarks interact by exchanging gluons with each other. Quark-gluon interaction is described by quantum chromody-

namics. According to quantum chromodynamics, the emission of hard gluons by quarks leads to logarithmic breaking of scaling. With an increase in the square of the transmitted momentum Q^2 , the number of gluons emitted by quarks increases sharply, gluons give rise to a quark-antiquark pair $q\bar{q}$. These processes lead to an increase in the density of gluons and sea $q\bar{q}$ -pairs in the nucleon at large x . Thus, taking into account quark-gluon interactions leads to the dependence of the distribution functions and quark fragmentation on the square of the momentum transfer Q^2 :

$$q(x, Q^2), \quad \bar{q}(x, Q^2), \quad D_q^h(z, Q^2), \quad D_{\bar{q}}^h(z, Q^2).$$

Let us now substitute the hadron SF obtained in the QPM (21) into the general expressions for the cross sections (17). In the quark-parton approximation for the cross section of the process $\ell^- + N \rightarrow \ell^- + h + X$, we obtain [9]:

$$\begin{aligned}
 \frac{d\sigma^{(-)}(\lambda; h_N)}{dx dy dz} &= \pi\alpha^2 s x \times \\
 &\times \sum_q \{ q(x) D_q^h(z) [(1+\lambda)(F_{RR}^2 + (1-y)^2 F_{RL}^2) + (1-\lambda)(F_{LL}^2 + (1-y)^2 F_{LR}^2)] + \\
 &\quad + \bar{q}(x) D_{\bar{q}}^h(z) [(1+\lambda)(F_{RL}^2 + (1-y)^2 F_{RR}^2) + (1-\lambda)(F_{LR}^2 + (1-y)^2 F_{LL}^2)] + \\
 &\quad + h_N \Delta q(x) D_q^h(z) [(1+\lambda)(F_{RR}^2 - (1-y)^2 F_{RL}^2) - (1-\lambda)(F_{LL}^2 - (1-y)^2 F_{LR}^2)] + \\
 &\quad + h_N \Delta \bar{q}(x) D_{\bar{q}}^h(z) [(1+\lambda)(F_{RL}^2 - (1-y)^2 F_{RR}^2) - (1-\lambda)(F_{LR}^2 - (1-y)^2 F_{LL}^2)] \}. \quad (22)
 \end{aligned}$$

Here, $F_{RR}(q)$, $F_{RL}(q)$, $F_{LL}(q)$ and $F_{LR}(q)$ are the spiral amplitudes of the quark-parton subprocesses

$$\begin{aligned}
 \ell_R + q_R &\rightarrow \ell_R + q_R, \quad \ell_R + q_L \rightarrow \ell_R + q_L, \\
 \ell_L + q_R &\rightarrow \ell_L + q_R, \quad \ell_L + q_L \rightarrow \ell_L + q_L,
 \end{aligned}$$

respectively (the first and second indices correspond to the helicities of the lepton and quark). The spiral amplitudes depend on the square of the momentum transfer Q^2 and on the charges of the neutral weak currents of the lepton and quarks

$$F_{\alpha\beta}(q) = \frac{Q_\ell Q_q}{Q^2} + \frac{g_\alpha(\ell)g_\beta(q)}{Q^2 + M_Z^2} \quad (\alpha; \beta = L, R). \quad (23)$$

The differential cross section of the SIDIS of a polarized antilepton on a polarized nucleon $\ell^+ + N \rightarrow \ell^+ + h + X$ is obtained from the differential cross section (22), replacing the indices of the spiral amplitudes $F_{RR}(q) \leftrightarrow F_{LR}(q)$, $F_{LL}(q) \leftrightarrow F_{RL}(q)$:

$$\begin{aligned} \frac{d\sigma^{(+)}(\lambda; h_N)}{dxdydz} &= \pi\alpha^2_{SX} \times \\ &\times \sum_q \{ q(x) D_q^h(z) [(1+\lambda)(F_{LR}^2 + (1-y)^2 F_{LL}^2) + (1-\lambda)(F_{RL}^2 + (1-y)^2 F_{RR}^2)] + \\ &+ \bar{q}(x) D_{\bar{q}}^h(z) [(1+\lambda)(F_{LL}^2 + (1-y)^2 F_{LR}^2) + (1-\lambda)(F_{RR}^2 + (1-y)^2 F_{RL}^2)] + \\ &+ h_N \Delta q(x) D_q^h(z) [(1+\lambda)(F_{LR}^2 - (1-y)^2 F_{LL}^2) - (1-\lambda)(F_{RL}^2 - (1-y)^2 F_{RR}^2)] + \\ &+ h_N \Delta \bar{q}(x) D_{\bar{q}}^h(z) [(1+\lambda)(F_{LL}^2 - (1-y)^2 F_{LR}^2) - (1-\lambda)(F_{RR}^2 - (1-y)^2 F_{RL}^2)] \}. \end{aligned} \quad (24)$$

5. LONGITUDINAL SPIN ASYMMETRIES

The set of spiral amplitudes $F_{\alpha\beta}(q)$ ($\alpha; \beta = L, R$) introduced above also determine the longitudinal spin asymmetries in semi-inclusive reactions (1) and (2). The study of longitudinal spin asymmetries in semi-inclusive reactions $\ell^\mp + N \rightarrow \ell^\mp + h^\mp + X$ is an important source of information on the distribution functions of polarized quarks, antiquarks and gluons in polarized nucleons. The longitudinal spin asymmetries include the following expressions:

$$\begin{aligned} A_{N1}^{h^+ - h^-} &= \frac{[\sigma_{LL}^{(\mp)}(h^+) - \sigma_{LL}^{(\mp)}(h^-)] - [\sigma_{LR}^{(\mp)}(h^+) - \sigma_{LR}^{(\mp)}(h^-)]}{[\sigma_{LL}^{(\mp)}(h^+) - \sigma_{LL}^{(\mp)}(h^-)] + [\sigma_{LR}^{(\mp)}(h^+) - \sigma_{LR}^{(\mp)}(h^-)]}, \\ A_{N2}^{h^+ - h^-} &= \frac{[\sigma_{RR}^{(\mp)}(h^+) - \sigma_{RR}^{(\mp)}(h^-)] - [\sigma_{RL}^{(\mp)}(h^+) - \sigma_{RL}^{(\mp)}(h^-)]}{[\sigma_{RR}^{(\mp)}(h^+) - \sigma_{RR}^{(\mp)}(h^-)] + [\sigma_{RL}^{(\mp)}(h^+) - \sigma_{RL}^{(\mp)}(h^-)]}, \end{aligned} \quad (25)$$

$$\begin{aligned} A_{N1}^{h^\pm} &= \frac{\sigma_{LL}^{(\mp)}(h^\pm) - \sigma_{LR}^{(\mp)}(h^\pm)}{\sigma_{LL}^{(\mp)}(h^\pm) + \sigma_{LR}^{(\mp)}(h^\pm)}, \\ A_{N2}^{h^\pm} &= \frac{\sigma_{RR}^{(\mp)}(h^\pm) - \sigma_{RL}^{(\mp)}(h^\pm)}{\sigma_{RR}^{(\mp)}(h^\pm) + \sigma_{RL}^{(\mp)}(h^\pm)}; \end{aligned} \quad (26)$$

$$\begin{aligned} A_1(e_R^- - e_L^+) &= \frac{\sigma_R^{(-)}(h^\pm) - \sigma_L^{(+)}(h^\pm)}{\sigma_R^{(-)}(h^\pm) + \sigma_L^{(+)}(h^\pm)}, \\ A_2(e_L^- - e_R^+) &= \frac{\sigma_L^{(-)}(h^\pm) - \sigma_R^{(+)}(h^\pm)}{\sigma_L^{(-)}(h^\pm) + \sigma_R^{(+)}(h^\pm)}; \end{aligned} \quad (27)$$

$$\begin{aligned} A_1 &= \frac{\sigma_{RL}^{(-)}(h^\pm) - \sigma_{LR}^{(+)}(h^\pm)}{\sigma_{RL}^{(-)}(h^\pm) + \sigma_{LR}^{(+)}(h^\pm)}, \\ A_2 &= \frac{\sigma_{RR}^{(-)}(h^\pm) - \sigma_{LR}^{(+)}(h^\pm)}{\sigma_{RR}^{(-)}(h^\pm) + \sigma_{LR}^{(+)}(h^\pm)}. \end{aligned} \quad (28)$$

Here $\sigma_{LL}^{(-)}(h^\pm)$ ($\sigma_{LL}^{(+)}(h^\pm)$), $\sigma_{LR}^{(-)}(h^\pm)$ ($\sigma_{LR}^{(+)}(h^\pm)$), $\sigma_{RR}^{(-)}(h^\pm)$ ($\sigma_{RR}^{(+)}(h^\pm)$) and $\sigma_{RL}^{(-)}(h^\pm)$ ($\sigma_{RL}^{(+)}(h^\pm)$) are the differential cross sections of semi-inclusive reactions

$\ell^- + N \rightarrow \ell^- + h^\mp + X$
($\ell^+ + N \rightarrow \ell^+ + h^\mp + X$) at helicities of the lepton (antilepton), $\lambda = -1$, $h_N = -1$, $\lambda = -1$, $h_N = +1$, $\lambda = 1$, $h_N = 1$ and $\lambda = 1$, $h_N = -1$, $\sigma_L^{(-)}(h^\pm)$ and $\sigma_R^{(-)}(h^\pm)$, ($\sigma_L^{(+)}(h^\pm)$ and $\sigma_R^{(+)}(h^\pm)$) – are the differential cross sections of the SIDIS of the left and right polarized lepton (antilepton) on an unpolarized nucleon target. It should be noted that it is precisely this kind of longitudinal spin asymmetries that are experimentally investigated in a number of laboratories around the world (COMPASS, HERMES, EMC, SLAC, SMC, etc. [1-8]).

When determining the «difference» longitudinal spin asymmetry $A_N^{h^+ - h^-}$ the polarization states of the target lepton and nucleon are shown in the diagram in Fig. 2. First, left-handed leptons (ℓ_L^-) are scattered by a left-handed nucleon (N_L) (the nucleon spin vector is oriented against the motion of the lepton), and then the direction of the nucleon spin vector is reversed, i.e. left-handed leptons are already scattered by a right-handed nucleon (N_R).

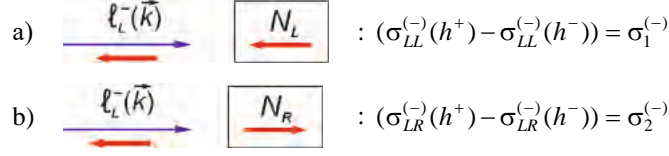


Fig. 2. Directions of the spins of the lepton and nucleon of the target.

The «difference» longitudinal spin asymmetry is equal to the ratio of the difference of the cross sections to their sum ($\sigma_1^{(-)} + \sigma_2^{(-)}$):

$$A_N^{h^+ - h^-} = \frac{[\sigma_{LL}^{(-)}(h^+) - \sigma_{LL}^{(-)}(h^-)] - [\sigma_{LR}^{(-)}(h^+) - \sigma_{LR}^{(-)}(h^-)]}{[\sigma_{LL}^{(-)}(h^+) - \sigma_{LL}^{(-)}(h^-)] + [\sigma_{LR}^{(-)}(h^+) - \sigma_{LR}^{(-)}(h^-)]}.$$

Based on the formulas for the differential cross sections of the processes $\ell^- + N \rightarrow \ell^- + h^\mp + X$ and $\ell^+ + N \rightarrow \ell^+ + h^\mp + X$ (22) and (24) for the longitudinal spin asymmetries (25) - (28), the expressions are obtained:

$$\begin{aligned} A_{N1}^{h^+ - h^-} = & \left\{ \sum_q \Delta q(x) [D_q^{h^+}(z) - D_q^{h^-}(z)] [F_{LL}^2(q) - (1-y)^2 F_{LR}^2(q)] + \right. \\ & + \sum_q \Delta \bar{q}(x) [D_{\bar{q}}^{h^+}(z) - D_{\bar{q}}^{h^-}(z)] [F_{LR}^2(q) - (1-y)^2 F_{LL}^2(q)] \left. \right\} \times \\ & \times \left\{ \sum_q q(x) [D_q^{h^+}(z) - D_q^{h^-}(z)] [F_{LL}^2(q) + (1-y)^2 F_{LR}^2(q)] + \right. \\ & \left. + \sum_q \bar{q}(x) [D_{\bar{q}}^{h^+}(z) - D_{\bar{q}}^{h^-}(z)] [F_{LR}^2(q) + (1-y)^2 F_{LL}^2(q)] \right\}^{-1}. \end{aligned} \quad (29)$$

$$\begin{aligned} A_{N2}^{h^+ - h^-} = & \left\{ \sum_q \Delta q(x) [D_q^{h^+}(z) - D_q^{h^-}(z)] [F_{RR}^2(q) - (1-y)^2 F_{RL}^2(q)] + \right. \\ & + \sum_q \Delta \bar{q}(x) [D_{\bar{q}}^{h^+}(z) - D_{\bar{q}}^{h^-}(z)] [F_{RL}^2(q) - (1-y)^2 F_{RR}^2(q)] \left. \right\} \times \\ & \times \left\{ \sum_q q(x) [D_q^{h^+}(z) - D_q^{h^-}(z)] [F_{RR}^2(q) + (1-y)^2 F_{RL}^2(q)] + \right. \\ & \left. + \sum_q \bar{q}(x) [D_{\bar{q}}^{h^+}(z) - D_{\bar{q}}^{h^-}(z)] [F_{RL}^2(q) + (1-y)^2 F_{RR}^2(q)] \right\}^{-1}. \end{aligned} \quad (30)$$

$$\begin{aligned} A_{N1}^{h^\pm} = & \left\{ \sum_q \Delta q(x) D_q^{h^\pm}(z) [F_{LL}^2(q) - (1-y)^2 F_{LR}^2(q)] + \right. \\ & + \sum_q \Delta \bar{q}(x) D_{\bar{q}}^{h^\pm}(z) [F_{LR}^2(q) - (1-y)^2 F_{LL}^2(q)] \left. \right\} \times \\ & \times \left\{ \sum_q q(x) D_q^{h^\pm}(z) [F_{LL}^2(q) + (1-y)^2 F_{LR}^2(q)] + \right. \\ & \left. + \sum_q \bar{q}(x) D_{\bar{q}}^{h^\pm}(z) [F_{LR}^2(q) + (1-y)^2 F_{LL}^2(q)] \right\}^{-1}. \end{aligned} \quad (31)$$

$$\begin{aligned} A_{N2}^{h^\pm} = & \left\{ \sum_q \Delta q(x) D_q^{h^\pm}(z) [F_{RR}^2(q) - (1-y)^2 F_{RL}^2(q)] + \right. \\ & + \sum_q \Delta \bar{q}(x) D_{\bar{q}}^{h^\pm}(z) [F_{RL}^2(q) - (1-y)^2 F_{RR}^2(q)] \left. \right\} \times \\ & \times \left\{ \sum_q q(x) D_q^{h^\pm}(z) [F_{RR}^2(q) + (1-y)^2 F_{RL}^2(q)] + \right. \\ & \left. + \sum_q \bar{q}(x) D_{\bar{q}}^{h^\pm}(z) [F_{RL}^2(q) + (1-y)^2 F_{RR}^2(q)] \right\}^{-1}. \end{aligned} \quad (32)$$

$$A_1(e_R^- - e_L^+) = f(y) \frac{\sum_q [q(x) D_q^{h^\pm}(z) - \bar{q}(x) D_{\bar{q}}^{h^\pm}(z)] [F_{RR}^2(q) - F_{RL}^2(q)]}{\sum_q [q(x) D_q^{h^\pm}(z) + \bar{q}(x) D_{\bar{q}}^{h^\pm}(z)] [F_{RR}^2(q) + F_{RL}^2(q)]}, \quad (33)$$

$$A_2(e_L^- - e_R^+) = f(y) \frac{\sum_q [q(x)D_q^{h\pm}(z) - \bar{q}(x)D_{\bar{q}}^{h\pm}(z)][F_{LL}^2(q) - F_{LR}^2(q)]}{\sum_q [q(x)D_q^{h\pm}(z) + \bar{q}(x)D_{\bar{q}}^{h\pm}(z)][F_{LL}^2(q) + F_{LR}^2(q)]}. \quad (34)$$

$$\begin{aligned} A_1 = f(y) & \left\{ \sum_q [q(x)D_q^{h\pm}(z) - \bar{q}(x)D_{\bar{q}}^{h\pm}(z)][F_{RR}^2(q) - F_{RL}^2(q)] - \right. \\ & - \sum_q [\Delta q(x)D_q^{h\pm}(z) + \Delta \bar{q}(x)D_{\bar{q}}^{h\pm}(z)][F_{RR}^2(q) + F_{RL}^2(q)] \times \\ & \times \left\{ \sum_q [q(x)D_q^{h\pm}(z) + \bar{q}(x)D_{\bar{q}}^{h\pm}(z)][F_{RR}^2(q) + F_{RL}^2(q)] + \right. \\ & \left. \left. + \sum_q [\Delta q(x)D_q^{h\pm}(z) - \Delta \bar{q}(x)D_{\bar{q}}^{h\pm}(z)][F_{RR}^2(q) - F_{RL}^2(q)] \right\}^{-1}. \right. \end{aligned} \quad (35)$$

$$\begin{aligned} A_2 = f(y) & \left\{ \sum_q [q(x)D_q^{h\pm}(z) - \bar{q}(x)D_{\bar{q}}^{h\pm}(z)][F_{RR}^2(q) - F_{RL}^2(q)] + \right. \\ & + \sum_q [\Delta q(x)D_q^{h\pm}(z) + \Delta \bar{q}(x)D_{\bar{q}}^{h\pm}(z)][F_{RR}^2(q) + F_{RL}^2(q)] \times \\ & \times \left\{ \sum_q [q(x)D_q^{h\pm}(z) + \bar{q}(x)D_{\bar{q}}^{h\pm}(z)][F_{RR}^2(q) + F_{RL}^2(q)] + \right. \\ & \left. \left. + \sum_q [\Delta q(x)D_q^{h\pm}(z) - \Delta \bar{q}(x)D_{\bar{q}}^{h\pm}(z)][F_{RR}^2(q) + F_{RL}^2(q)] \right\}^{-1}. \right. \end{aligned} \quad (36)$$

Introduced here function

$$f(y) = \frac{1 - (1 - y)^2}{1 + (1 - y)^2}. \quad (37)$$

Due to the charge independence of strong interactions, the quark fragmentation functions in π^\pm - and K^\pm -mesons satisfy a number of relations

$$\begin{aligned} D_u^{\pi^\pm}(z) &= D_d^{\pi^\pm}(z) = D_d^{\pi^\mp}(z) = D_u^{\pi^\mp}(z), \\ D_u^{K^\pm}(z) &= D_s^{K^\pm}(z) = D_s^{K^\mp}(z) = D_u^{K^\mp}(z). \end{aligned}$$

Calculations show that because of these relations, the «difference» longitudinal spin asymmetries

$A_{N1}^{h^+ - h^-}$ and $A_{N2}^{h^+ - h^-}$ do not depend on the functions of quark fragmentation into hadron h . These asymmetries include only the distribution functions of quarks in a nucleon $q(x)$, $\bar{q}(x)$, $\Delta q(x)$ and $\Delta \bar{q}(x)$. For example, in the processes $\ell^- + p \rightarrow \ell^- + \pi^\mp + X$ (only the contribution of valence and sea u - and d -quarks is taken into account), $\ell^- + N \rightarrow \ell^- + K^\mp + X$ (only the contribution of valence and sea u - and s -quarks is taken into account), longitudinal spin asymmetries $A_{p1}^{\pi^+ - \pi^-}$ and $A_{p1}^{K^+ - K^-}$ are expressed by formulas [9, 10]:

$$\begin{aligned} A_{p1}^{\pi^+ - \pi^-} &= \{ \Delta u_v(x)[F_{LL}^2(u) - (1 - y)^2 F_{LR}^2(u)] - \Delta d_v(x)[F_{LL}^2(d) - (1 - y)^2 F_{LR}^2(d)] + \\ & + [1 + (1 - y)^2] [\Delta u_s(x)(F_{LL}^2(u) - F_{LR}^2(u)) - \Delta d_s(x)(F_{LL}^2(d) - F_{LR}^2(d))] \} \times \\ & \times \{ u_v(x)[F_{LL}^2(u) + (1 - y)^2 F_{LR}^2(u)] - d_v(x)[F_{LL}^2(d) + (1 - y)^2 F_{LR}^2(d)] + \\ & + [1 - (1 - y)^2] [u_s(x)(F_{LL}^2(u) - F_{LR}^2(u)) - d_s(x)(F_{LL}^2(d) - F_{LR}^2(d))] \}^{-1}, \end{aligned} \quad (38)$$

$$\begin{aligned} A_{p1}^{K^+ - K^-} &= \{ \Delta u_v(x)[F_{LL}^2(u) - (1 - y)^2 F_{LR}^2(u)] + [1 + (1 - y)^2] [\Delta u_s(x)(F_{LL}^2(u) - F_{LR}^2(u)) - \\ & - \Delta s(x)(F_{LL}^2(s) - F_{LR}^2(s))] \} \times \{ u_v(x)[F_{LL}^2(u) + (1 - y)^2 F_{LR}^2(u)] + \\ & + [1 - (1 - y)^2] [u_s(x)(F_{LL}^2(u) - F_{LR}^2(u)) - s(x)(F_{LL}^2(s) - F_{LR}^2(s))] \}^{-1}. \end{aligned} \quad (39)$$

Here $u_v(x)$ and $d_v(x)$, $u_s(x)$, $d_s(x)$ and $s(x)$ are the distribution functions of valence u - and d (sea u -, d - and s -)quarks in a proton.

The expressions for longitudinal spin asymmetries (38) and (39) contain phenomenological parameters

– the distribution functions of valence and sea quarks in a polarized nucleon. There are a number of sets in the literature for the distribution functions of quarks in nucleons [11, 13-19]. For numerical estimates of asymmetries, we used the distribution functions of valence and sea polarized quarks in nucleons

given in [19].

In Fig. 3 shows the dependence of the «difference» longitudinal spin asymmetry $A_{p1}^{\pi^+-\pi^-}$ in reaction $e^- + p \rightarrow e^- + \pi^\mp + X$ on variable x at energy $\sqrt{s}=300$ GeV and various fixed $y=0.1$ (curve 1), $y=0.4$ (curve 2) and $y=0.9$ (curve 3). As follows from the figure, the longitudinal spin asymmetry $A_{p1}^{\pi^+-\pi^-}$ in reactions $e^- + p \rightarrow e^- + \pi^\mp + X$ is positive and monotonically increases with increasing variable x . A similar dependence is observed for the longitudinal spin asymmetry $A_{p1}^{K^+-K^-}$ in the processes $e^- + N \rightarrow e^- + K^\mp + X$ (see Fig. 4, which illustrates the dependence of the asymmetry $A_{p1}^{K^+-K^-}$ on the variable x for different y).

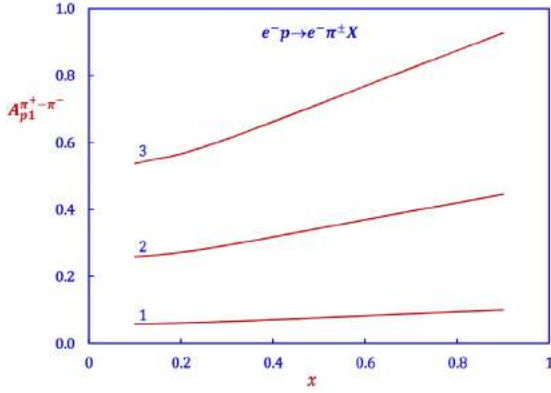


Fig. 3. Dependence of asymmetry $A_{p1}^{\pi^+-\pi^-}$ on x in reactions $e^- p \rightarrow e^- \pi^\mp X$ at $y = 0.1$; 0.4 and 0.9 (curves 1, 2, and 3, respectively).

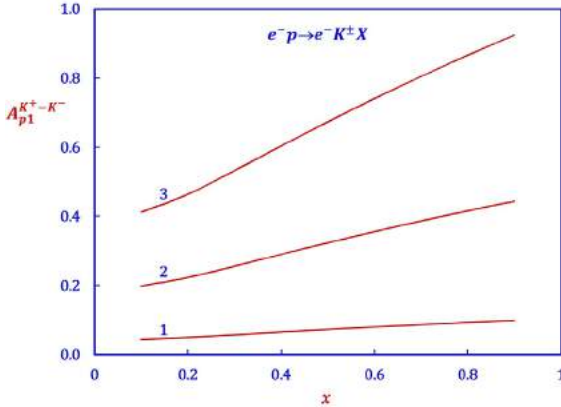


Fig. 4. Dependence of asymmetry $A_{p1}^{K^+-K^-}$ on x in reactions $e^- p \rightarrow e^- K^\mp X$ at $y = 0.1$; 0.4 and 0.9 (curves 1, 2, and 3, respectively).

For small values of the square of the momentum transfer ($Q^2 \ll M_Z^2$), the contribution of the Z -boson diagram to the cross section of the processes $e^\mp + p \rightarrow e^\mp + \pi^\pm + X$, $e^\mp + N \rightarrow e^\mp + K^\pm + X$ can be neglected, while all spiral amplitudes for a given quark subprocesses are the same

$$F_{LL}(q) = F_{LR}(q) = F_{RL}(q) = F_{RR}(q) = \frac{Q_e Q_q}{Q^2},$$

then the «difference» longitudinal two-spin asymmetry $A_N^{h^+-h^-}$ will depend only on the distribution functions of valence quarks:

$$\begin{aligned} A_{p1}^{\pi^+-\pi^-} &= \frac{4\Delta u_v(x) - \Delta d_v(x)}{4u_v(x) - d_v(x)} \cdot f(y), \\ A_{n1}^{\pi^+-\pi^-} &= \frac{4\Delta d_v(x) - \Delta u_v(x)}{4d_v(x) - u_v(x)} \cdot f(y), \\ A_{p1}^{K^+-K^-} &= \frac{\Delta u_v(x)}{u_v(x)} \cdot f(y), \\ A_{n1}^{K^+-K^-} &= \frac{\Delta d_v(x)}{d_v(x)} \cdot f(y), \\ A_{d1}^{\pi^+-\pi^-} &= A_{d1}^{K^+-K^-} = \frac{\Delta u_v(x) + \Delta d_v(x)}{u_v(x) + d_v(x)} \cdot f(y). \end{aligned} \quad (40)$$

As can be seen, for a polarized isoscalar deuteron target, the «difference» longitudinal spin asymmetries coincide:

$$A_d^{\pi^+-\pi^-} = A_d^{K^+-K^-} = \frac{\Delta u_v(x) + \Delta d_v(x)}{u_v(x) + d_v(x)}, \quad (41)$$

where $\Delta q_v(x) = \Delta q(x) - \Delta \bar{q}(x)$.

Longitudinal spin asymmetries $A_N^{h^+}$ and $A_N^{h^-}$ contain the functions of fragmentation of quarks (anti-quarks) into a hadron h^+ and h^- :

$$A_N^{h^\pm} = \frac{\sum_q Q_q^2 [\Delta q(x) D_q^{h^\pm} + \Delta \bar{q}(x) D_{\bar{q}}^{h^\pm}]}{\sum_q Q_q^2 [q(x) D_q^{h^\pm} + \bar{q}(x) D_{\bar{q}}^{h^\pm}]}, \quad (42)$$

where

$$D_q^{h^\pm} = \int_0^1 D_q^{h^\pm}(z) dz.$$

Using $SU(2)$ and C -charge symmetries, at the production of π^\pm -mesons, we have three fragmentation functions:

$$\begin{aligned} D_1 &= D_u^{\pi^+} = D_d^{\pi^-} = D_{\bar{d}}^{\pi^+} = D_{\bar{u}}^{\pi^-}, \\ D_2 &= D_{\bar{u}}^{\pi^+} = D_d^{\pi^-} = D_d^{\pi^+} = D_{\bar{u}}^{\pi^-}, \\ D_3 &= D_s^{\pi^+} = D_s^{\pi^-} = D_{\bar{s}}^{\pi^+} = D_{\bar{s}}^{\pi^-}. \end{aligned}$$

Experiments conducted by the NMC, E866 and HERMES collaborations revealed that the unpolarized sea is not symmetrical:

$$\int_0^1 [\bar{d}(x) - \bar{u}(x)] dx = \begin{cases} 0.148 \pm 0.039 \text{ (NMC)}, \\ 0.118 \pm 0.012 \text{ (E866)}, \\ 0.16 \pm 0.03 \text{ (HERMES)}. \end{cases}$$

What we know about the polarized sea $\int_0^1 [\Delta \bar{u}(x) + \Delta \bar{d}(x)] dx = ?$

To answer this question, consider the flavor symmetry of quarks $SU_f(3)$ ($m_u \cong m_d \cong m_s \cong 0$). We introduce the following notation

$$\begin{aligned} a_0 &= \Delta u + \Delta\bar{u} + \Delta d + \Delta\bar{d} + \Delta s + \Delta\bar{s}, \\ a_3 &= \Delta u + \Delta\bar{u} - (\Delta d + \Delta\bar{d}), \\ a_8 &= \Delta u + \Delta\bar{u} + \Delta d + \Delta\bar{d} - 2(\Delta s + \Delta\bar{s}), \end{aligned} \quad (43)$$

where

$$\Delta q = \int_0^1 \Delta q(x) dx, \quad \Delta\bar{q} = \int_0^1 \Delta\bar{q}(x) dx.$$

From (43) we find the sum $\Delta\bar{u} + \Delta\bar{d}$:

$$\Delta\bar{u} + \Delta\bar{d} = (\Delta s + \Delta\bar{s}) + \frac{1}{2}(a_8 - \Gamma_v), \quad (44)$$

here Γ_v – is the first moment of the valence polarized quarks in the proton:

$$\Gamma_v = \Delta u_v + \Delta d_v = \int_0^1 [\Delta u_v(x) + \Delta d_v(x)] dx. \quad (45)$$

Thus, knowing the distribution of valence quarks in a nucleon $\Delta u_v(x) + \Delta d_v(x)$, we can find the sum $\Delta\bar{u} + \Delta\bar{d}$. The dependence of this sum on is a straight line (see Fig. 5, which shows the dependence of $\Delta\bar{u} + \Delta\bar{d}$ on Γ_v).

From experiments carried out by the COMPASS collaboration on the DIS of leptons on nucleons, the value a_0 :

$$a_0 = 0.35 \pm 0.03 \pm 0.15.$$

By the width of the decays of hyperons found a_8 :

$$a_8 = 0.59 \pm 0.03.$$

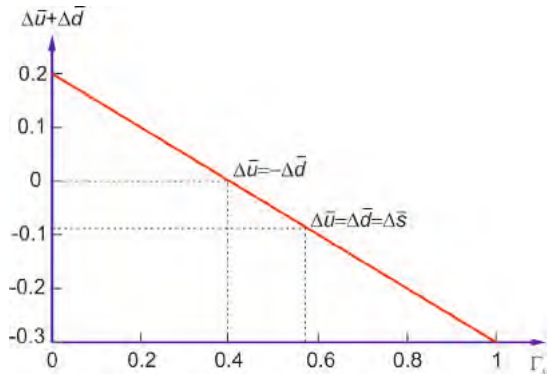


Fig. 5. Dependence of the amount $\Delta\bar{u} + \Delta\bar{d}$ on Γ_v .

Knowing (a_0) and (a_8), from formulas (43) we find the sum ($\Delta s + \Delta\bar{s}$):

$$\Delta s + \Delta\bar{s} = \frac{1}{3}(a_0 - a_8) = -0.09 \pm 0.01 \pm 0.02.$$

For the sum of the polarized sea $\Delta\bar{u} + \Delta\bar{d}$, the following linear dependence is obtained:

$$\Delta\bar{u}_v + \Delta\bar{d}_v = 0.2 - 0.5\Gamma_v. \quad (46)$$

With a symmetric distribution of quarks in a nucleon, we have:

$$\Gamma_v = a_8 = 0.59 \text{ and } \Delta\bar{u} = \Delta\bar{d} = -0.075.$$

If $\Gamma_v = 0.4$, then the distribution of polarized quarks in the proton is asymmetric:

$$\Delta\bar{u} + \Delta\bar{d} = 0 \rightarrow \Delta\bar{u} = -\Delta\bar{d}.$$

From formula (41), we determine the distribution of polarized valence quarks in a nucleon:

$$\begin{aligned} \Delta u_v(x) + \Delta d_v(x) &= A_d^{\pi^+ - \pi^-}(x) \cdot (u_v(x) + d_v(x)) \\ \Delta\bar{u} &= \Delta\bar{d} = \Delta\bar{s} \end{aligned} \quad (47)$$

where $A_d^{\pi^+ - \pi^-}(x)$ is the «difference» longitudinal spin asymmetry, $(u_v(x) + d_v(x))$ – is the distribution of valence unpolarized quarks in a proton.

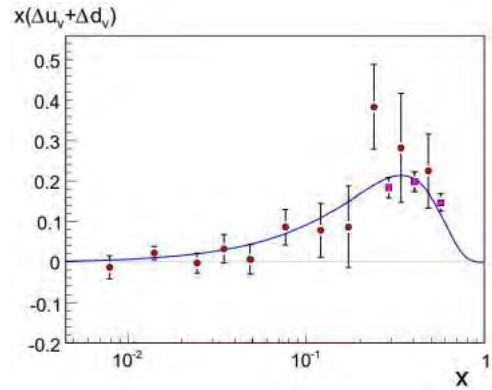


Fig. 6. Dependence of polarized valence quark Distributions $x(\Delta u_v + \Delta d_v)$ from a variable x .

The x distribution of polarized valence quarks in the nucleon was studied by the COMPASS collaboration in the SIDIS processes of polarized muons with an energy of 160 GeV on a polarized deuteron target at $Q^2 = 10 \text{ GeV}^2$ and $0.006 < x < 0.7$ [20]. In Fig. 6 shows the dependence of the valence polarized quark distributions $x(\Delta u_v + \Delta d_v)$ on the variable x . The experimental results of COMPASS with the corresponding errors are also noted there. The solid line corresponds to the distribution functions of polarized quarks from [17]. The results of the COMPASS experiments show that the first moment of polarized quark distributions is

$$\int_{0.006}^{0.7} [\Delta u_v(x) + \Delta d_v(x)] dx = 0.40 \pm 0.08 \pm 0.05.$$

This result is consistent with the fact that the asymmetric distribution of quarks ($\Delta\bar{u} = -\Delta\bar{d}$) prevails over the symmetric distribution ($\Delta\bar{u} = \Delta\bar{d}$).

It should be noted that the longitudinal spin asymmetries $A_{N1}^{h^\pm}$, $A_{N2}^{h^\pm}$, $A_1(e_R^- - e_L^+)$, $A_2(e_L^- - e_R^+)$, A_1 and A_2 , in contrast to the «difference» spin asymmetries, depend on the functions of quark fragmentation into a hadron h^\pm . For example, the asymmetries $A_{p1}^{\pi^+}$ and A_1 in the reactions $e^\mp + p \rightarrow e^\mp + \pi^+ + X$ are determined by the formulas (only the contribution of the diagram with the γ -quant exchange is taken into account):

$$\begin{aligned}
 A_{p1}^{\pi^+} = -A_1 = f(y) \{ & Q_u^2 [\Delta u_\nu(x) D_u^{\pi^+}(z) + \Delta u_s(x) (D_u^{\pi^+}(z) + D_u^{\pi^+}(z))] + \\
 & + Q_d^2 [\Delta d_\nu(x) D_d^{\pi^+}(z) + \Delta d_s(x) (D_d^{\pi^+}(z) + D_d^{\pi^+}(z) + 2D_s^{\pi^+}(z))] \} \times \\
 & \times \{ Q_u^2 [u_\nu(x) D_u^{\pi^+}(z) + u_s(x) (D_u^{\pi^+}(z) + D_u^{\pi^+}(z))] + \\
 & + Q_d^2 [d_\nu(x) D_d^{\pi^+}(z) + d_s(x) (D_d^{\pi^+}(z) + D_d^{\pi^+}(z) + 2D_s^{\pi^+}(z))] \}^{-1}. \quad (48)
 \end{aligned}$$

As for the asymmetry $A_1(e_R^- - e_L^+)$, we note that, in contrast to other longitudinal two-spin asymmetries, this asymmetry is due to the longitudinal polarizations of the lepton and antilepton. This one-spin asymmetry $P -$ is odd and is expressed by the formula:

$$\begin{aligned}
 A_1(e_R^- - e_L^+) = f(y) \{ & [F_{RR}^2(u) - F_{RL}^2(u)] [u_\nu(x) D_u^{\pi^+}(z) + u_s(x) (D_u^{\pi^+}(z) - D_u^{\pi^+}(z))] + \\
 & + [F_{RR}^2(d) - F_{RL}^2(d)] [d_\nu(x) D_d^{\pi^+}(z) + d_s(x) (D_d^{\pi^+}(z) - D_d^{\pi^+}(z))] \} \times \\
 & \times \{ [F_{RR}^2(u) + F_{RL}^2(u)] [u_\nu(x) D_u^{\pi^+}(z) + u_s(x) (D_u^{\pi^+}(z) + D_u^{\pi^+}(z))] + \\
 & + [F_{RR}^2(d) + F_{RL}^2(d)] [d_\nu(x) D_d^{\pi^+}(z) + d_s(x) (D_d^{\pi^+}(z) + D_d^{\pi^+}(z) + 2D_s^{\pi^+}(z))] \}^{-1}. \quad (49)
 \end{aligned}$$

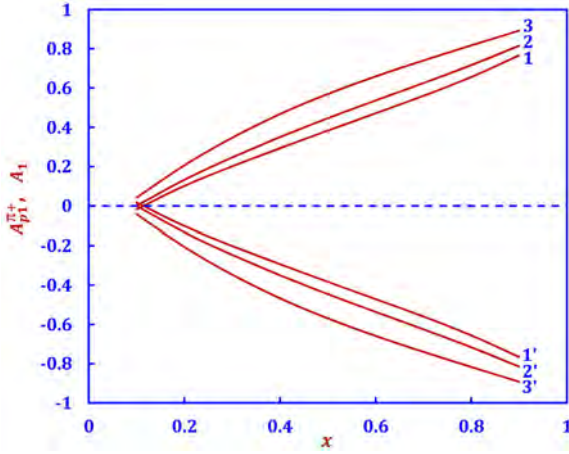


Fig. 7. Dependence of asymmetries $A_{p1}^{\pi^+}$ (curves 1, 2 and 3) and A_1 (curves 1', 2' and 3') on the variable x at $z = 0.2, 0.5$ and 0.8 respectively.

In Fig. 7 shows the dependence of the longitudinal spin asymmetries $A_{p1}^{\pi^+}$ and A_1 on the variable x at $y=1$ and a fixed value $z = 0.2, z = 0.5$ and $z = 0.8$. The asymmetry A_{p1} (A_1) is positive (negative) and with an increase in the variable x it increases (decreases), an increase in the variable z leads to an increase (decrease) in this asymmetry.

Fig. 8 illustrates the dependence of asymmetries $A_{p1}^{\pi^+}$ and A_1 on variable z at $y=1$ and a fixed value $x = 0.2, x = 0.5$ and $x = 0.8$. Asymmetry A_{p1} (A_1) is positive (negative) and with increasing variable x slowly increases (decreases). In Fig. 9 shows the dependence of the P -odd longitudinal spin asymmetry $A_1(e_R^- - e_L^+)$ on the variable x at a fixed value of $z = 0.2, 0.5$ and 0.8 (curves 1, 2, and 3). It is observed here that with an increase in the variable x , the asymmetry $A_1(e_R^- - e_L^+)$ increases and reaches a maximum at $x = 0.6$, and a further increase in the variable leads to a decrease in this asymmetry.

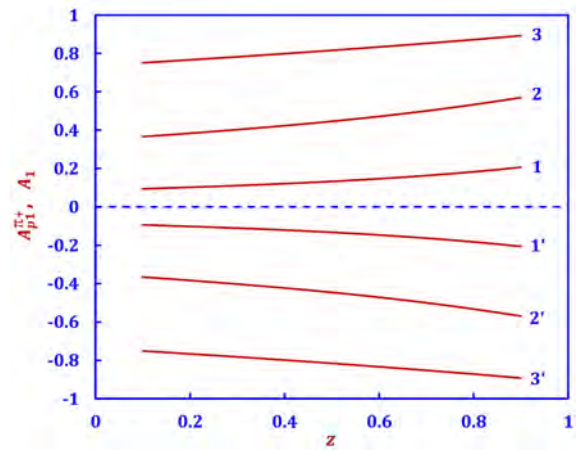


Fig. 8. Dependence of asymmetries $A_{p1}^{\pi^+}$ (curves 1, 2 and 3) and A_1 (curves 1', 2' and 3') on the variable z at $x = 0.2, 0.5$ and 0.8 , respectively.

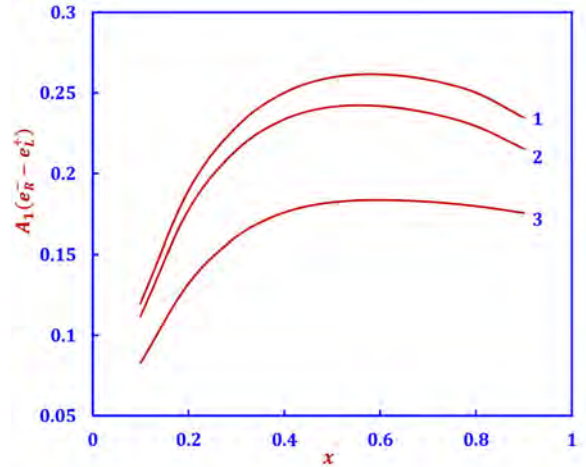


Fig. 9. Dependence of the P -odd longitudinal spin asymmetry $A_1(e_R^- - e_L^+)$ on the variable x at fixed $z = 0.2$ (curve 1), 0.5 (curve 2) and 0.8 (curve 3).

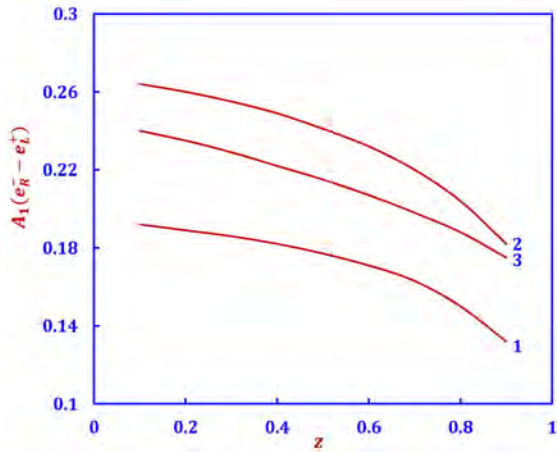


Fig. 10. Dependence of the P -odd longitudinal spin asymmetry $A_1(e_R^- - e_L^+)$ on the variable z at fixed $x = 0.2$ (curve 1), 0.5 (curve 2) and 0.8 (curve 3).

In Fig. 10 illustrates the dependence of the

asymmetry $A_1(e_R^- - e_L^+)$ on the variable z at fixed $x = 0.2, 0.5$ and 0.8 (curves 1, 2 and 3). The asymmetry is positive and decreases with increasing z .

CONCLUSION

Here we discussed the longitudinal spin asymmetries $A_N^{h^+h^-}$, $A_N^{h^+}$, $A_N^{h^-}$, $A_1(e_R^- - e_L^+)$, A_1 in semi-inclusive deep inelastic scattering of polarized leptons (antileptons) by polarized nucleons: $\ell^\pm + N \rightarrow \ell^\pm + h^\pm + X$. By introducing the hadron structure functions, analytical expressions for the differential cross sections of the processes are obtained, the hadron structure functions are calculated in the quark-parton model, the longitudinal spin asymmetries are determined, and the asymmetry behavior depending on the variables x , y and z is studied in detail.

The longitudinal spin asymmetry $A_d^{\pi^+\pi^-}$ is compared with the results of the COMPASS experiments.

- [1] I.A. Savin. COMPASS results on the nucleon spin structure. Nucl. Phys., B (Proceedings Supplements), 2011, V. 219-220, p. 94-101.
- [2] COMPASS Collaboration (Alekseev M., et al.). Flavour Separation of Helicity Distributions from Deep Inelastic Muon-Deuteron Scattering, Phys. Lett., B, 2009, V. 680, p. 217-224.
- [3] COMPASS Collaboration (Alekseev M., et al.). Quark helicity distributions from longitudinal spin asymmetries in muon-proton and muon-deuteron scattering. Phys. Lett., B, 2010, V. 693, p. 227-235.
- [4] HERMES Collaboration. Quark helicity distributions in the nucleon for up, down, and strange quarks from semi-inclusive deep-inelastic scattering. Phys. Rev., D, 2005, V. 71, p. 012003.
- [5] HERMES Collaboration. Precise determination of the spin structure function g_1 of the proton, deuteron and neutron. Phys. Rev., D, 2007, V. 75, p. 012007.
- [6] SMC Collaboration (Adeva B. et al.) Polarization of valence and non-strange sea quarks in the nucleon from semi-inclusive spin asymmetries. Phys. Lett., B, 1996, V. 369, No 1, p. 93-100.
- [7] SMC Collaboration (Adeva B. et al.) Polarized quark distributions in the nucleon from semi-inclusive spin asymmetries. Phys. Lett., B, 1998, V. 369, No 1-2, p. 180-190.
- [8] SMC Collaboration (Adeva B. et al.) Next-to-leading order QCD analysis of the spin structure function g_1 Phys. Lett., D, 1998, V. 58, No 12, p. 112002-1-15.
- [9] S.K. Abdullayev. Azerbaijan Journal of Physics, Fizika, Baku, 2013, V. XIX, №3, p.19-24.
- [10] S.K. Abdullayev, M.Sh. Gojayev Double-spin asymmetries in semi-inclusive processes $\ell^\mp N \rightarrow \ell^\mp h X$ (in Russian) News of Baku University. Series of physico-mathematical sciences, 2007, No 3, p.118-123.
- [11] D. De Florian, Y.R. Habarnau. Polarized semi-inclusive electroweak structure functions at next-to-leading-order. J. European Phys., C, 2013, V. 73, p. 2356(1-11).
- [12] J. Beringer et al. (Particle Data Group Collaboration). Review of Particle Physics. Phys. Rev., D, 2012, V. 86, No 1, 010001.
- [13] M. Glück, E. Reya, A. Vogt. Dynamical Parton Distributions Revisited. J. Eur. Phys., C., 1998, V. 5, No 1, p.461-470. Arxiv: hep-ph/9806404.
- [14] B. Lampe, E. Reya. Spin Physics and Polarized Structure Functions. MPI-Phi / 98-23; DO-TH 98/02, 1998.
- [15] M. Gluck, E. Reya, M. Stratmann, W. Vogelsang. Models for the Polarized Parton Distributions of the Nucleon. Phys. Rev., D, 2005, V. 63, p.094005-1-12.
- [16] D. De Florian, R. Sassot, M. Stratmann, W. Vogelsang. Extraction of spin-dependent parton densities and their uncertainties. Phys. Rev., D, 2009, V. 80, p. 034030-1-26.
- [17] D. De Florian, G.A. Navarro, R. Sassot. Sea quarks and gluon polarization in the nucleon at NLO accuracy. Phys. Rev., D, 2005, V. 71, p.094018-1-12.
- [18] A.D. Martin, W.J. Stirling, R.S. Thorne. MRST partons generated in a fixed-flavour scheme. Phys. Lett., B, 2006, V. 636, p. 259-264.
- [19] H.Y. Cheng, S.N. Lai, C.Y. Wu. Polarized parton distribution functions reexamined. Phys. Rev. D, 1996, V. 53, p. 2380-2389.
- [20] A. Korzenev. Valence Quarks Polarization from COMPASS / 15th International Workshop on Deep-Inelastic Scattering and Related Subjects, Munich, Germany, 16-20 Apr 2007, pp.567-570.

Received:17.11.2020

EVALUATION OF NITRITE-INDUCED OXIDATIVE MODIFICATION OF HEMOGLOBIN AND THE POSSIBILITY OF ITS REGULATION BY SODIUM SELENITE BY RAMAN MICROSCOPY

T.M. HUSEYNOV, M.Z. DADASHOV, S.Y. HUSEYNOVA

Institute of Biophysics of Azerbaijan NAS

117, Zahid Khalilov str., Baku, AZ 1141

tokhus@mail.ru

The method of microscopic recombination scattering was used to assess the conformational changes in hemoglobin under the influence of sodium nitrite (NaNO_2) taken in small (0-0.35 μM) and moderate (0.35-0.70 μM) final concentrations and sodium selenite (Na_2SeO_3 - 5 μM) in incubation medium containing human erythrocytes (incubation time 30 min). Under the influence of NaNO_2 , there is a dose-dependent decrease (up to 60%) in HbO_2 content, an increase ($\approx 25\%$) in the ability of hemoglobin to bind ligands and an increase ($\approx 12\%$) in the ability of hemoglobin to release ligands (O_2), as well as an increase (up to 13%) in the severity of symmetric and asymmetric pyrolic hematoporphyrin rings. Sodium selenite reduces the oxidative effects of sodium nitrite decreasing the increase in MetHb accumulation and a decrease of hemoglobin saturation by oxygen.

Keywords: sodium nitrite, sodium selenite, hemoglobin, erythrocytes, Raman scattering.

PACS:

1. INTRODUCTION

In the last 20-30 years, there has been an increased interest in the participation of nitrogen-containing compounds in human life, in particular nitrites and its main metabolite which is nitrogen oxide. One of the important aspects of this interest is their toxicity due to high emissions of nitrogen oxides into the biosphere by industrial enterprises and transport, nitrites in agricultural production, nitrites in the food and pharmaceutical industry [1-4]. The toxicity of nitrites and its main metabolite, nitric oxide, is due to their ability to influence the oxidative status of hemoglobin (Hb), which transports O_2 , CO_2 , and NO [1,2].

Relatively recently, it was found that NO takes part in allosteric transformations of Hb [5], despite the fact that NO has a significantly higher affinity constant for hemoporphyrin ($\text{Fe} + 2$) than O_2 , and thus competes with oxygen for binding to hemoglobin [3, 6,7], which determines its influence on the hemoglobin conformation and on its affinity for oxygen. Nitric oxide is incorporated into hemoporphyrin, forming nitrosyl hemoglobin (HbNO), and cysteyl residues of the α and β polypeptide chains of hemoglobin (nitrosothiols) [1]. Of particular interest is the incorporation of NO into 93 βcysHb (SNOHb (β 93)) due to the proximity of this fragment to heme, which allows the transition from heme (HbNO position) to this position and vice versa [1,7]. The binding of NO to the SH groups of the α and β chains of Hb increases the affinity of NO for hemoglobin and prevents the transition to the T-conformational state, which has a low affinity of Hb for oxygen. During the transition from the R-state to the T-state, NO is released from the SH-residue 93 β of cysteine into the free state, or passes into hemoporphyrin of hemoglobin (HbNO) [7]. Thus, hemoglobin acts as a utilizer of excess NO; is oxidized to metHb and possibly to deeper forms of oxidation (1-6). In addition, an excess of NO (or

nitrite) coming from outside or as a result of endogenous synthesis can lead to a violation of the prooxidant-oxidative equilibrium (oxidative stress) in erythrocytes with the formation of reactive oxygen and nitrogen species (peroxynitrite) [8]. Erythrocytes have an effective antioxidant (AO) system, which includes superoxide dismutase (SOD), catalase, glutathione peroxidase (GP), peroxiredoxin-2 (Prx-2), glutathione reductase, etc. [9]. One of the important components of the AO system of erythrocytes is selenium, which is included in the active center of GP, as well as nonspecifically included in hemoglobin, replacing sulfur in sulfur-containing amino acid residues [10,11] and affecting the oxidative resistance of hemoglobin [12]. These considerations suggest that the toxic effect of nitrite or NO on hemoglobin and on erythrocytes in general can be limited by the use of selenium in the form of sodium selenite, which has an active metabolism in erythrocytes: it easily penetrates into the cytosol, initially it is almost completely incorporated into hemoglobin by a complex redox mechanism, being reduced to selenide, it leaves through the AE1 anion exchanger, partially remaining in hemoglobin, essentially in certain vacant localization sites, as NO in polypeptide chains ($\text{SNO}\beta\text{cys}$) [13, 14]. It should be noted that if the 93 βcys amino acid residue provides AO protection of hemoglobin [15] protecting hemoporphyrin, then it can be assumed that its selenium analog can do this more efficiently due to its greater reactivity (electronegativity) [16].

It follows that the toxic effect of nitrites or nitric oxide in the form of oxidative effects on hemoglobin and erythrocytes can be weakened by selenium when the erythrocytes (hemoglobin) are enriched with selenite. From the above, it can be seen that both nitrites and selenites, when penetrating into erythrocytes, are actively metabolized and incorporated into hemoglobin, exerting a certain effect on it, which can affect its functional activity and, first

of all, its ability to bind with oxygen. This is closely related to its conformational state.

In this regard, we used the method of microscopic recombination scattering (MCR) to assess possible conformational changes of hemoglobin caused by nitrite and selenite exposure, which allows non-invasively, by the characteristic frequencies of the Raman spectrum, to trace the effects of induced exposure: sodium nitrite and selenite [17,18,19,20].

2. MATERIALS AND METHODS

In the experiments, sodium chloride, sodium nitrite, monosubstituted and disubstituted sodium phosphate monosubstituted and disubstituted were used (CP quality, Russia).

In experiments *in vitro*, donor blood was used, taken from the cubital vein into tubes with heparin (20 units / ml of blood). The main object of the study was human erythrocytes and Hb. Separation of blood plasma from erythrocytes was performed by centrifugation (800 g for 15 min). To obtain a suspension of erythrocytes, the erythrocyte sediment was washed three times in a tenfold volume of sodium phosphate buffer solution (SPB) (10 mM SPB pH 7.4; 0.15 mM NaCl), centrifuged at 800 g for 15 min, followed by removal of the supernatant. Hemolysis of erythrocytes was achieved by diluting the erythrocyte mass with distilled water in a ratio of 1: 9, followed by freezing, thawing and centrifugation at 10000 g. The nitrite effect was carried out with sodium nitrite NaNO₂ in four final concentrations (small - 0.07, 0.15 mM and moderate -0.35, 0.70 mM), exposure time from 0 to 30 minutes, at 37 ° C. These low toxicity doses were taken to track the oxidative process of Hb caused by nitrite. Raman spectra of Hb were recorded using a microscopic system 3D-confocal Raman spectrometer Nanofinder 30 (Japan). To excite the Raman spectra, we used a laser with a wavelength of 532 nm, radiation power 10 mW, objective 50 x. The presence of bands in the Raman spectrum reflects the structural and functional state of the studied material - hemoglobin. In particular, the state of the iron atom (Fe) and its ligands (O₂, NO, CO₂, etc.) that bind to it, affecting the state of the structure of the tetrapyrrole cycle of hemoporphyrin (porphyrin ring) of hemoglobin. To analyze the conformational changes and O₂-binding properties of hemoglobin, we used the characteristic bands of the Raman spectra of erythrocytes 1172, 1355, 1548-1552, 1580-1588, 1618-1668 [17, 18, 19].

Sodium selenite, which has a high permeability through the erythrocyte membrane and an active metabolism in them, was used as a possible antioxidant affecting oxidative processes. The final concentration in the incubation medium was selected based on previous experiments. In particular, before using sodium selenite as an antioxidant, need to take into account that selenite in excess, along with the AO effect, can enhance lipid peroxidation, reduce the content of NADPH, GSH, oxidizing the SH-groups of hemoglobin and other proteins, and ultimately

provoke hemolysis of erythrocytes [11]. In this regard, it was necessary to choose its optimal concentration range of antioxidant effects on erythrocytes. In our early works, it was found that sodium selenite, with a final concentration in the incubation medium of up to 10 μM (incubation period 0-30 min), does not have a prooxidative effect, does not oxidize erythrocyte GSH, and at final concentrations in the range of 1.0-10 μM, it has a certain AO effect: it slows down the accumulation of MetHb, slightly increases the activity of catalase and GP, and has no effect on lipid peroxidation [21]. Based on this, the final concentration of sodium selenite 5 μM was chosen as the optimal one.

To assess the ratios of nitrite-oxidized forms of Hb in erythrocytes, two series of experiments were carried out with the incubation times of the samples (30 min) at 25 ° C. Each series included one control and one prototype. The control sample contained 2.0 ml of erythrocyte suspension and 0.2 ml of buffered saline solution, and the test samples - 2.0 ml of erythrocyte suspension and 0.2 ml of NaNO₂ with different final concentrations.

The accumulation of metHb was assessed using semiempirical formulas [22]. The hemoglobin content was assessed by the standard cyanide method.

Statistical processing of the obtained results was carried out using the t-test at a significance level of p <0.05 [23] using the Microsoftexcel 2010 software package.

3. RESULTS AND THEIR DISCUSSION

Figure 1 shows the Raman spectrum of erythrocytes, which essentially reflect the spectrum of hematoporphyrin (600-1800 cm⁻¹). The family of bands (1375-1355 cm⁻¹) is the frequency region responsible for the vibrations of C-N bonds, the position of which depends on the oxidation state of the iron atom, while the frequency section 1650-1562 cm⁻¹ is responsible for the vibrations of C=C bonds, whose positions depend on the spin of the iron ion. The binding of such ligands as O₂ and NO causes a conformational rearrangement, which is associated with a change in spin. The content (concentration) of HbO₂ (zero spin charge) is estimated from the ratio of the intensity of the bands (I1375 / I1355 + I1375). The formation of a complex of hematoporphyrin with NO is possible in two variants: one is realized without breaking the bond on histidine of the protein part of Hb (ratio I1620 / I1580), in the second variant, this bond is broken (ratio I1658 / I1580), which means the ability of NO to regulate the release of oxygen from hemoglobin, i.e. its transition from a low-spin state to a high-spin state (5/2). In the case of direct oxidation of hemoglobin by sodium nitrite, π-electrons are "pumped" from the iron ions (Fe²⁺ → Fe³⁺) to the orbital of nitrogen oxides, reducing them to nitrates, which is reflected in the vibrational component of the binding energy (shift 1379-1372 cm⁻¹), as well as a decrease in the maximum at 1357 cm⁻¹ (characterizes the growth of MetHb) [17, 18]. The substitution of NO for O₂ in the Hb porphyrin macrocycle ultimately

leads to a change in the position of the iron atom (Fe^{2+}) with respect to the plane of the macrocycle, which is reflected in the spin state, i.e. allows to judge the degree of conformational rearrangement [17, 18, 19].

It is known that nitrites, both in isolated erythrocytes and in vivo, depending on their dose, oxidize hemoglobin to different oxidation states. This process is accompanied by a decrease in the level of oxyhemoglobin (HbO_2) [1,6,7]. In our previous works, it was shown that even low final concentrations of NaNO_2

(0.007–0.070 mM) in the incubation medium already in the first 15–30 min can significantly affect the accumulation of methemoglobin, without accelerating the development of LPO, rather, on the contrary, inhibiting it [24, 25]. In experiments using sodium selenite as an antioxidant, it was also found that it can inhibit the accumulation of MetHb and the development of LPO (moderate doses of NaNO_2) [24,25].

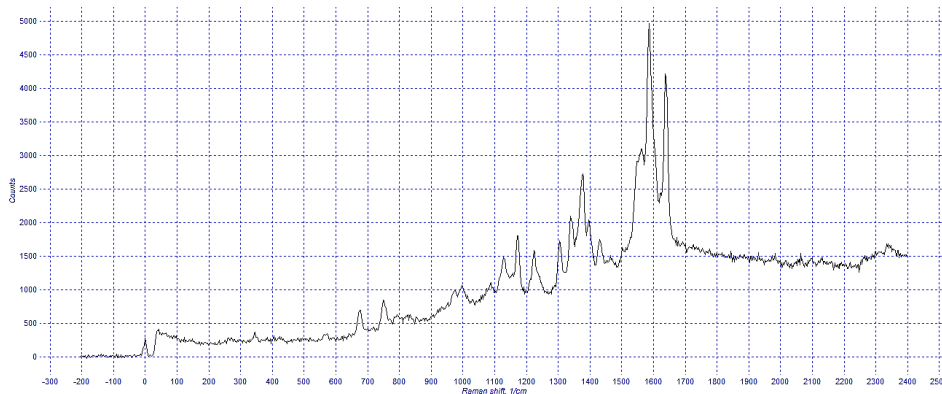


Fig 1. Raman spectra of hemoglobin in human erythrocytes diluted 1/50 in buffered saline (pH 7.4; 25 ° C, laser $\lambda = 532$ nm).

Figure 2 shows the results of experiments on the induced oxidation of hemoglobin with low and moderate doses of sodium nitrite and the inhibitory effect of sodium selenite taken at a dose of 5 μM (30 min incubation). The accumulation of MetHb is due to the decrease in HbO_2 , which can be traced using Raman spectroscopy, which, in

contrast to optical spectroscopy, is distinguished by higher selectivity and sensitivity.

In particular, Fig. 3 shows the estimated relative intensities of the peaks responsible for the state of heme groups at 677 cm^{-1} , 1375 cm^{-1} , 1580 cm^{-1} , 1640 cm^{-1} .

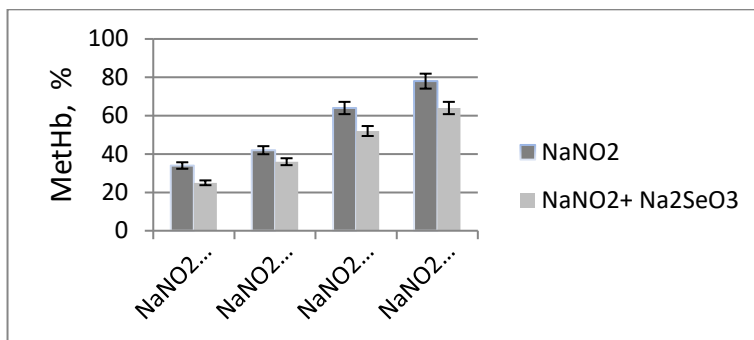


Fig 2. Accumulation of MetHb at various final concentrations of NaNO_2 and participation of Na_2SeO_3 (5 μM) (25 ° C, 10mM SPB, pH 7.4; 30 min)

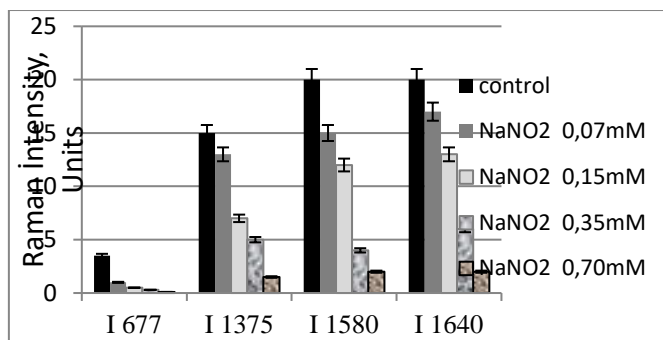


Fig 3. Intensity of Raman spectra of erythrocytes incubated with NaNO_2 (0.07, 0.15, 0.35, 0.70 mM) (25 ° C, 10mM SPB, pH 7.4; 30 min)

Table

Parameters of RAMAN spectroscopy of hemoglobin of erythrocytes treated with sodium nitrite at various concentrations (small 0-0.35 and moderate 0.35-0.70 mM) in the presence of sodium selenite (5 μM). (25 °C, 10mM SPB, pH 7.4; 30 min).

Index	Experimental groups											
	kontrol	NaNO ₂				NaNO ₂ + Na ₂ SeO ₃ (5 μM)						
		0,07 mM	0,15 mM	0,35 mM	0,70 mM	0,00 mM	0,07mM	0,15 mM	0,35 mM	0,70 mM		
The proportion of oxyhemoglobin in erythrocytes (I ₁₃₇₅ /I ₁₃₅₅ +I ₁₃₇₅)	0,73 ± 0,08	0,62 ± 0,04 *	0,55 ± 0,05 *	0,41 ± 0,04 *	0,75±0,05	0,70±0,07	0,67±0,04 *	0,61±0,05 **	0,53±0,06 **			
The ability of hemoglobin to bind ligands (I ₁₃₅₅ /I ₁₅₅₀)	0,68± 0,03	0,77 ± 0,05 *	0,83 ± 0,07 *	0,90 ± 0,08 **	0,66±0,06	0,70 ± 0,05	0,72 ± 0,06	0,77 ± 0,05 *	0,85 ± 0,05 **			
The ability of hemoglobin to separate ligands (I ₁₃₇₅ /I ₁₅₈₀)	0,71 ± 0,06	0,75 ± 0,06	0,78 ± 0,05 *	0,81 ± 0,06 *	0,71 ± 0,08	0,72±0,06	0,73 ± 0,05	0,72±0,04	0,72±0,06			
The affinity of hemoglobin for oxygen (I ₁₃₅₅ /I ₁₅₅₀)/(I ₁₃₇₅ /I ₁₅₈₀)	1,04 ± 0,05	0,93 ± 0,07 *	0,88 ± 0,12 *	0,81 ± 0,15 *	1,05 ± 0,07	1,02±0,12	0,97 ± 0,11 *	0,90±0,10	0,85±0,15			
The severity of symmetric and asymmetric vibrations of pyrrole rings (I ₁₃₇₅ /I ₁₁₇₂)	1,20 ± 0,04	1,29± 0,09 *	1,35 ± 0,10 *	1,41 ± 0,11 **	1,21 ± 0,17	1,22 ± 0,06	1,24 ± 0,08	1,30 ± 0,10 *	1,33±0,11 **			
Fraction of complexes of hemoglobin with NO in the presence of a bond between the Fe ²⁺ atom and globin (I ₁₆₁₈ /I ₁₅₈₀)	0,22±0,02	0,16 ± 0,03 **	0,12 ± 0,04 **	0,08 ± 0,02 **	0,22±0,02	0,20 ± 0,02	0,18 ± 0,03 *	0,15±0,05 *	0,21±0,04			
Fraction of complexes of hemoglobin with NO in the absence of a bond between the Fe ²⁺ atom and globin (I ₁₆₆₉ /I ₁₅₈₀)	0,41 ± 0,02	0,45 ± 0,03	0,47 ± 0,03 *	0,55 ± 0,05 **	0,40±0,05	0,41±0,03	0,42±0,04	0,45±0,05 *	0,43±0,06 *			

Note * $p < 0.05$, ** $p < 0.01$

Fig. 3 shows that as the final concentrations NaNO_2 increase, the peaks at 677 cm^{-1} , 1375 cm^{-1} , 1580 cm^{-1} , 1640 cm^{-1} decrease or even disappear (a band characterizing the bond with hemoglobin). The most sensitive to the spin state is the 1375 band, which characterizes the degree of decrease in the HbO_2 saturation.

Table shows the main parameters of Raman scattering spectroscopy of human erythrocytes incubated in a medium containing sodium nitrite in various final concentrations from 0 to 0.70 mM and sodium selenite with a final concentration of $5\text{ }\mu\text{M}$ for 30 min ($25\text{ }^\circ\text{C}$, 10 mM sodium phosphate buffer, 0.15 M NaCl). It can be seen from it that the treatment with NaNO_2 leads to:

1. A dose-dependent decrease (to 60%) of the HbO_2 content, which is estimated from the ratio of the intensity of the peaks $I_{1375} / I_{1355} + I_{1375}$.
2. A noticeable increase ($\approx 25\%$) in the ability of hemoglobin to bind ligands, including O_2 (I_{1355} / I_{1580}).
3. Some increase ($\approx 12\%$) in the ability of hemoglobin to give ligands, including oxygen (I_{1375} / I_{1580}).
4. Certain multidirectional change in the affinity of hemoglobin for oxygen, estimated by the ratio $(I_{1355} / I_{1550}) / (I_{1350} / I_{1580})$.
5. A noticeable increase in the severity of symmetry and asymmetry of vibrations of the pyrrole rings of hemoglobin in isolated erythrocytes (I_{1375} / I_{1172}).
6. A significant decrease in the proportion of hemoglobin complexes with NO (up to 50%, depending on the final concentration of NaNO_2) in the presence of a bond between the Fe^{2+} atom and globin (I_{1618} / I_{1580}).
7. Some increase in the proportion of complexes of hemoglobin with NO, with the separation of the bond of the Fe^{2+} atom and globulin, which changes little depending on the concentration of NaNO_2 (I_{1618} / I_{1580}).
8. Sodium selenite ($5\text{ }\mu\text{M}$) introduced into the incubation medium has a clear AO effect, reducing the effects of the oxidative effect of NaNO_2 , i.e. reduces the effects of conformational rearrangements. This is especially noticeable in the effect of inhibition of reducing the saturation of hemoglobin with oxygen (HbO_2). This AO effect is hardly noticeable in the range of low concentrations (0.07 - 0.35 mM), but above 0.35 mM, i.e. at moderate final concentrations of NaNO_2 , it is noticeably pronounced.

It is also important to note here that sodium selenite smoothes not only a decrease in the HbO_2 level and, accordingly, an increase in MetHb, but also changes in other parameters of conformational rearrangements caused by nitrites. One of the possible mechanisms of this effect is the very fact of the inclusion of selenium in the globular part of hemoglobin at position 93 β cys, replacing sulfur, thereby affecting the affinity of hemoglobin for

oxygen under conditions of nitrite exposure, changes, in general, the electron density around heme [26].

Table 1 shows that sodium nitrite affects the conformation of hemoglobin and this rearrangement is the deeper, the greater the dose of NaNO_2 (final concentration). However, on the affinity of hemoglobin for oxygen, in the indicated final concentrations, NaNO_2 has a somewhat multidirectional effect: small doses (0.07-0.15 mM) can increase the affinity, and moderate doses (0.35-0.70 mM) can reduce. This seems to be due to the fact that the affinity of hemoglobin for oxygen is influenced by two opposite processes. Formed during nitrite exposure, NO is incorporated into heme with the formation of nitrosyl hemoglobin, contributing to the formation of five-coordinate nitrosyl iron (HbNO) by separation of the proximal ligation. This leads to the stabilization of the T-state, which provides an easier release of oxygen, i.e. a decrease in affinity [27], which takes place for moderate doses of NaNO_2 . On the other hand, by nitrosylation (inclusion of NO at the 93 β cysHb position), the formation of SNO-Hb increases the affinity of Hb for oxygen due to a change in the electron density [7].

It also follows from the ratio of the intensities of the peaks I 1375: I 1172 that sodium nitrite has a dose-dependent effect of increasing (up to 13%) the severity of symmetric and asymmetric vibrations of the pyrrole rings of hematoporphyrin. This effect can be associated with an increase in the proportion of membrane-bound hemoglobin in isolated erythrocytes [28]. Our earlier results also indicate this [25,29,30], i.e. an increase in the accumulation of membrane-bound hemoglobin, which penetrating through the AE1 anion exchanger into the erythrocyte membrane can stimulate the LPO process [28].

The totality of the results obtained allows us to draw certain conclusions: Raman microscopy makes it possible to determine with high sensitivity the onset of conformational rearrangements in hemoglobin caused by the action of sodium nitrite. This can be seen: 1) by the example of fixing multidirectional changes in the affinity of Hb for oxygen, depending on the "dose" of the effect of sodium nitrite on erythrocytes (hemoglobin); 2) depending on the final concentrations of sodium nitrite, a rupture of the bond between hemoglobin and an iron atom and a change in the valence of an iron atom ($\text{Fe}^{2+} \rightarrow \text{Fe}^{3+}$) may occur; 3) by the effect on the oscillatory processes in the pyrrole rings of hematoporphyrin, which can give information about the accumulation of membrane-bound hemoglobin, which stimulates the development of oxidative processes in erythrocytes; 4) Included selenium from sodium selenite smoothes out the conformational effects induced by sodium nitrite, while weakening oxidative processes on Hb, reducing the accumulation of MetHb and reducing the proportion of membrane-bound hemoglobin.

[1] A.W. DeMartino, D.B Kim-Shapiro, R.P. Patel, M.T. Gladwin. Nitrite and Nitrate Chemical

Biology and Signalling. Br J Pharmacol. 2019;176(2):228-245. doi: 10.1111/bph.14484.

- [2] E.I. Nasybullina, O.V. Kosmachevskaya, A.F. Topunov. Influence of nitric oxide metabolites on the formation of membrane-bound hemoglobin under carbonyl stress. "Fundamentals of Biotechnology" RAS, Moscow, Russia. 2018; 4: 93–104. doi: 10.17076 / them814.
- [3] A.F. Vanin. Dinitrosyl iron complexes with thiol-containing ligands as a «working form» of endogenous nitric oxide, nitric Oxide Biol. Chem. 2016; 54: 15-29.
- [4] A.K. Martusevich, A.G. Solovieva, S.P. Peretyagin, A.F. Vanin. Comparative analysis of the effect of free and deposited NO on the state of pro- and antioxidant systems in the blood. "Biophysics" ". 2015; 60 (2): 348-354.
- [5] Duke researchers discover central role of Nitric Oxide in hemoglobin action. Duke Medicine News and Communication. 3 Nov. 2004. dukehealth.org
- [6] M.K. Ruban, G.A. Vashanov, I.A. Lavrinenko. Oxygenation-induced structural and functional modifications of nitrosylated hemoglobin. VSU Bulletin, series: chemistry. biology. pharmacy, 2010;1:56-61.
- [7] A.I. Hobbs, M.T. Gladwin, R.P. Patel, D.L.H. Williams, A.R. Butler. Haemoglobin: NO transporter, NO inactivator or none of the above. TRENDS in Pharmacological Science. 2002; 23: 406–411.
- [8] P.K. Maurya, P. Kumar, P. Chandra. Biomarkers of oxidative stress in erythrocytes as a function of human age. World J Methodol. 2015; 5(4): 216–222. doi: 10.5662/wjm.v5.i4.216.
- [9] S. Rocha, D. Gomes, M. Lima, E. Bronze-da-Rocha, Santos-Silva A. Peroxiredoxin 2, glutathione peroxidase, and catalase in the cytosol and membrane of erythrocytes under H₂O₂-induced oxidative stress. Free Radic Res. 2015;49(8):990-1003. doi: 10.3109/10715762.2015.1028402.
- [10] M.A. Beilstein, P.D. Whanger. Distribution of selenium and glutathione peroxidase in blood fraction from humans, rhesus and a quere monkey, rats and sheep. J. Nutr; 1983; 113(11):2138-2146. doi:10.1093/jn/113.11.2138.
- [11] R.F. Burk, K.E. Hill. Regulation of Selenium Metabolism and Transport. Annu Rev Nutr 2015;35:109-34. doi: 10.1146/annurev-nutr-071714-034250.
- [12] T.M. Huseynov, F.R. Yakhyeva, R.T. Gulieva. Effect of selenium on the resistance of hemoglobin to photooxidative processes. Ukrainian Biochemical Journal. 2012; 84(2): 53-60.
- [13] K.T. Suzuki, Y. Shiobara, M. Itoh, M. Ohmichi. Selective uptake of selenite by red blood cells. Analyst. 1998;123(1):63-67. doi: 10.1039/a706230c.
- [14] M. Haratake, K. Fujimoto, M. Ono, M. Nakayama. Selenium binding to human hemoglobin via selenotrisulfide. Biochim Biophys Acta. 2005; 25;1723(1-3):215-220. doi:10.1016/j.bbagen.2005.02.002.
- [15] D.A. Vitturi, C.W. Sun, V.M. Harper. Antioxidant Functions for the Hemoglobin β93 Cysteine Residue in Erythrocytes and in the Vascular Compartment in Vivo. Free Radic Biol Med. 2013; 55:119-29. doi: 10.1016/j.freeradbiomed.2012.11.003.
- [16] U.M. Viswanathan, T. Burkholz and C. Jacob. Electrochemistry at the edge of reason: Chalcogen-based redox systems in biochemistry and drug design, Zeitschrift für Physikalische Chemie, 227(5): 691-706 (2013). doi.org/10.1524/zpch.2013.0321
- [17] G.V. Maksimov, N.A. Brazhe, A.I. Yusipovich, E.Yu. Parshina, O.V. Rodnenkov, A.B. Rubin, G.G. Levin, V.A. Bykov. The use of nanoparticles to study the conformations of the approximate hemoglobin. Biophysics, 2011; 56(6):1099-1104
- [18] P. Ivo, J. Terner, R.N. Pittman, E. Proffitt and K.R. Ward. Measurement of hemoglobin oxygen saturation using Raman microspectroscopy and 532-nm excitation. J Appl Physiol. 2008; 104: 1809–1817. doi:10.1152/japplphysiol.00025.2008.
- [19] M.F. Zhu, Y.Y. Huang, Z.Y. Guo, Z.F. Zhuang, S.H. Liu. Detection of methemoglobin in whole blood based on confocal micro-Raman spectroscopy and multivariate statistical techniques. Scanning 2014; 36: 471–478. doi: 10.1002/sca.21143
- [20] S.Y. Huseynova, T.M. Huseynov, M.Z. Dadashov. Oxidative modification of hemoglobin by nitrites and the protective role of selenium. Possibilities of Raman spectroscopy. Azerbaijan journal of physics. Baku, 2015; 21(03): 16-20.
- [21] S.Y. Huseynova. Oxidative metabolism of sodium selenite in isolated human erythrocytes in vitro. Biomedicine (Baku).2019;17(3):18-23. doi: 10.24411/1815-3917-2019-10018
- [22] J. Szebeni, C.C. Winterbourn, R.W. Carrell. Oxidative interactions between haemoglobin and membrane lipid. A liposome model. Biochem. J. 1984. V. 220. No 3. P. 685–692
- [23] G.F. Lakin. Biometriya. Moscow, 1990; 352 p.
- [24] S.Y. Huseynova, R.T. Gulieva, M.Z. Dadashov, A.I. Jafarov, F.R. Yakhyeva, T.M. Guseinov. Oxidative modification of hemoglobin of isolated erythrocytes in an incubation medium containing donors of nitric oxide and sodium selenite. Bulletin of the Novosibirsk State Pedagogical University. 2016; 6(5):207-215.
- [25] S.Y. Huseynova, T.M. Huseynov, M.Z. Dadashov. Oxidative modification of erythrocytes with moderate doses of sodium nitrite in in vitro experiments, Medical biophysics and biochemical chemistry. 2018;(3)1:189-195.
- [26] H. Kosaka. Nitric oxide and hemoglobin interactions in the vasculature. Biochim. Biophys. Acta . 1999; 1411: 370–377.
- [27] M.C. Garel, C. Domenget, J. Caburi-Martin, C. Prehu, F. Galacteros, Y. Beuzard. Covalent binding of glutathione to hemoglobin. I. Inhibition of hemoglobin S polymerization. J. Biol. Chem. 1986; 261:14704–14709.

- [28] *N.A. Brazhe, S. Abdali, R.A. Brazhe, O.G. Luneva et. al* New insight into erythrocyte through in vivo surface-enhanced raman spectroscopy *Biophys J.* 2009; 97(12): 3206–3214. doi: 10.1016/j.bpj.2009.09.029
- [29] *S.Y. Huseynova, T.M. Huseynov, M.Z. Dadashov.* Evaluation of nitrite-induced oxidative modification of hemoglobin by Raman spectroscopy. Abstracts of the International Scientific Conference dedicated to the 90th anniversary of the National Academy of Sciences of Belarus and the 45th anniversary of the Institute of Biophysics and Cell Engineering, Belarus, Minsk, June 27-29, 2018 g, page 149.
- [30] *S.Y. Huseynova.* Membrane-bound hemoglobin as an indicator of nitric toxicity of erythrocytes. *Azerbaijan chemical journal* 2019, 2020 (2) : 67-73. doi.org/10.32737/0005-2531-2020-2-67-73.

Received:17.11.2020

CONTENTS

1.	On biological activity of selenium compounds T.M. Guseynov, T.R. Mehdiyev, R.T. Guliyeva, B.Sh. Barkhalov	3
2.	Ab initio calculation Al, Co, Sr doped graphene S.S. Huseynova, S.O. Mammadova, A.A. Sadigova	11
3.	The thermal power and conductivity of superconducting $\text{Bi}_2\text{Sr}_2\text{Ca}_{0.4}\text{Zn}_{0.6}\text{Cu}_2\text{O}_y$ G.I. Agayeva	15
4.	The production of a chargino pair in polarized lepton-antilepton collisions (II) S.K. Abdullayev, M.Sh. Gojayev, A.K. Gulayeva	19
5.	Phase transition at thermal treatment of $\text{TlIn}_{1-x}\text{Sn}_x\text{Se}_2$ amorphous films M.M. Panakhov, E.Sh. Alekperov, E.S. Garayev, S.A. Sadraddinov¹, A.M. Nazarov, S.S. Farzaliyev	28
6.	Longitudinal spin asymmetries in semi-inclusive deep-inelastic scattering of polarized leptons by polarized nucleons S.K. Abdullayev, M.Sh. Gojayev, A.K. Gulayeva	32
7.	Evaluation of nitrite-induced oxidative modification of hemoglobin and the possibility of its regulation by sodium selenite by Raman microscopy T.M. Huseynov, M.Z. Dadashov, S.Y. Huseynova	44



www.physics.gov.az